Developing Highly Multiplexed Technology for High-throughput Super-resolution Fluorescence Microscopy

Pedro Manuel Bento Carvalho Almada

A dissertation submitted in partial fulfillment

of the requirements for the degree of

Doctor of Philosophy

of

University College London.

Laboratory for Molecular Cell Biology

University College London

Supervisors

Ricardo Henriques

Guillaume Charras

18th December 2017

I, Pedro Manuel Bento Carvalho Almada, confirm that the work presented in this thesis is my own. Where information has been derived from other sources, I confirm that this has been indicated in the work.

Abstract

High-Throughput imaging can reconstruct complex signalling networks, reveal unknown interactions and capture rare cellular events. Simultaneously, the development of Single Molecule Localization Super Resolution Microscopy has enabled molecular-level structural information to be obtained in a single cell. But the increase in resolution comes at a trade-off for the amount of molecular species that can be imaged and the time it takes to acquire data, all of which limit the applicability of super-resolution to high-throughput work-flows. The present work details a framework to address this. It combines three independent approaches: a microscope hardware design approach to increase the amount of data that can be obtained in a Super-Resolution experiment; an optofluidics platform that can be wholly synchronized with most microscopes; and a sequential labelling framework to increase the number of species that can be imaged in Super-Resolution in a single cell. The hardware design is validated by performing Single Molecule Localization of cytoskeleton components and its throughput is shown to be up to an order of magnitude larger than a corresponding commercial system. We demonstrate a complete optofluidics platform to integrate microfluidics with a microscope, enabling live imaging, drug application, fixation, and staining in single cells synchronized with imaging protocols. Finally, we show an efficient sequential labelling protocol that is compatible with the optofluidics platform, enabling several molecular species to be imaged in the same cells. Overall, our approach increases the speed and amount of data that can be acquired in a single of Super-Resolution experiment, as well as, by performing on-line fixation, considerably improves our capacity for High-Throughput experiments in Super-Resolution imaging.

Impact Statement

By combining super-resolution, sequential labelling and microfluidics, live imaging of single cells can be directly linked to highly multiplexed, high resolution fixed imaging of cellular components, enabling more data to be extracted from a single cell than has been otherwise possible. With this method, potentially, the state of entire signalling pathways can be reconstructed in single cells in a high-throughput manner. For Systems Biology, this means biological networks can be identified and parameterized with unprecedented precision and accuracy. The use of online fixation has the potential of solving a long-standing issue in Systems Biology which is the lack of temporal information on predicted biological networks. Such information can also be used to probe the impact of drugs on whole signalling pathways with much greater detail than before. Pharmaceutical drug screening would benefit from this as the predictive power of early validation screens would increase. This could reduce the number false positives and increase the number of valid candidate drugs, thereby accelerating the drug discovery process. By reducing the number of false positives, less funding would be wasted and it would also reduce the number of animals used on non-beneficial drug trials. Given the current lack of new antibiotics being developed, the increase of valid candidate drugs could be an invaluable boost to world health. In support of this, microscopy and microfluidics companies would stand to gain from integrating microscope and pump software packages. This sort of technology would then open up for researchers from basic science across to large pharmaceutical companies. From better products in the microscopy and microfluidics industries, to new ways to do Systems Biology, to sorely needed new drugs, this framework presents many new possibilities.

Acknowledgements

I would like to acknowledge my supervisors, Ricardo Henriques and Guillaume Charras, without whom none of this would have been possible. Working with Pedro Matos Pereira has been a genuine pleasure and I am indebted to him for his advice and tremendous help. Caron Jacobs was of great assistance in all cell culture related matters and her continouous upkeep of the lab has been the plank that keeps everyone else afloat. Anna Bove and Jessica Davies have guided me through the dark arts of microfluidics and I am very grateful for their assistance. Siân Culley has provided valuable input in all my outptus, and I thank her for that. David Albrecht's generosity can not be overstated and his help and presence in the lab is only marred by the fact he had not joined sooner. It has been, in equal parts, difficult and gratifying to discuss with Nils Gustafsson all maner of things and I will surely miss those chats. Jason Mercer has been highly supportive and collaborating with him has been a highlight for these four years. The LMCB smoking crew of Pedro, Gautam Dey and Agathe Chaigne were the calms in the storm that made it possible to go back to it and keep on with the science. There are more names than I can mention here so I will thank all of the LMCB for its incredible environment and great people. Collaborating with Buzz Baum, Cristina Dix, Dylan Owen and Michael Shannon and generating science was a truly motivating experience and I hope they took as much from it as I did from them. I would be remiss not to thank Alan Lowe and Kwasi Kwakwa for invaluable input and discussions on all things relating to microscopes and single molecule imaging. Ralf Jungmann, Florian Schüder and Thomas Schlichthärle were very generous to have hosted me in Munich and continously helpful in teaching me all things relating to DNA-PAINT.

And finally, I want to acknowledge Ekaterina Kapitonova for her patience and calming presence in the face of my crumbling mental stability. Without her support, this thesis would never have materialized.

Contents

1 Introduction **14**

1.1 Resolution in Light Microscopy 14

1.2 Super-Resolution Fluorescence Microscopy 18

1.3 High-Throughput Single Molecule Localisation Microscopy 23

1.4 Sequential Labelling 28

1.5 Fluidics for High-throughput Microscopy 31

1.6 Thesis Scope 34

1.7 Bibliography 35

2 High-Throughput Single Molecule Super-Resolution Microscope **36**

2.1 Introduction 36

2.1.1 Illumination Intensity 36

2.1.2 Large FOV Homogeneity 37

2.1.3 Total Internal Reflection Fluorescence Microscopy 38

2.1.4 Dual Camera Imaging 40

2.1.5 Drift Correction 41

2.1.6 Chapter Scope 44

2.2 Results 45

2.2.1 Microscope Design 45

2.2.1.1 Microscope Parts and Assembly 45

2.2.1.2 High-density TIRF Illuminator 47

2.2.1.3 Large FOV Illumination 49

2.2.1.4 Dual-Camera sCMOS Imaging 55

2.2.2 Drift Correction in Super-Resolution Microscopy 56
2.2.2.1 ASI CRISP 56
2.2.2.2 3D Cross-Correlation by Static Reference 58
2.2.3 Super-Resolution Cellular Imaging at High-throughput . . . 67
2.3 Discussion 71
2.3.1 Throughput of the Alpha 71
2.3.2 Illumination Intensity and Throughput in SMLM 71
2.3.3 Vibration dampening 73
2.3.4 Drift Correction in High-throughput 74
2.4 Methods 75
2.4.1 Cell Culture 75
2.4.2 Immuno-Staining 75
2.4.3 dSTORM Imaging 76
2.4.4 Software Development and Image Analysis 76
2.4.5 Bead preparations 77
2.4.6 Laser Intensity Measurements 77
2.5 Bibliography 78

3 Open-Source fluidics for *In-situ* Liquid Exchange 79
3.1 Introduction 79
3.1.1 Microfluidics for Microscopy 79
3.1.2 Microfluidic Flow-Cells 80
3.1.3 Plumbing for Fluidics 81
3.1.4 Pump Types for Fluidics 81
3.1.5 Open-Source Fluidics for *In-situ* Liquid Exchange 83
3.2 Results 86
3.2.1 A Fluidic Platform for Liquid Exchange *In-situ* 86
3.2.1.1 LEGO-based Syringe Pumps 86
3.2.1.2 3D Printed Syringe Pump 89
3.2.1.3 Control Systems for Integrated Microscope and Fluidic Applications 90

3.2.2 Fluidic Device Design for Bulk Liquid Exchange *In-situ* . . 96
3.2.2.1 Channel-type Microfluidic Devices 96
3.2.2.2 Dish-based Microfluidic Device Design 100
3.3 Discussion 106
3.3.1 Dish-based Devices 106
3.3.2 NanoJ Pumps 106
3.3.3 Software 108
3.3.4 Conclusions 109
3.4 Attribution 111
3.5 Methods 112
3.5.1 Fluidic Device Fabrication and Intubation 112
3.5.2 Cell Culture and Immuno-staining 113
3.5.3 Software Development 113
3.6 Bibliography 114

4 Online Fixation and Sequential Labelling for High-Throughput Super-Resolution 115

4.1 Introduction 115
4.1.1 Sequential Labelling *In-situ* 115
4.1.2 Adhesion of Migratory Animal Cells During Cell Division . 119
4.1.3 Dynamics of Adhesion Nano-clustering During T-cell Motility 120
4.1.4 Chapter Scope 122
4.2 Results 123
4.2.1 Methods for High-Throughput Sequential Labelling *In-situ* . 123
4.2.2 Multi-modal, Sequential Labelling Super-Resolution Imaging Enabled by Automated Microfluidics 127
4.2.3 Online Fixation Reveals Origin and Adhesion Mechanism of Retraction Fibres 129
4.2.4 Online Fixation and Super-Resolution Sequential Labelling Reveals Link Between T-cell Speed and LFA Cluster Size . 132

4.3 Discussion . . . 135
4.3.1 Antibody Elution Methods for Microscopy . . . 135
4.3.2 Multiplexing Methods for High-Throughput Super-Resolution Microscopy . . . 137
4.3.3 Integrin from Focal Adhesions Determines Retraction Fibre Adhesion Sites . . . 139
4.3.4 T-cell LFA-1 Nano-Cluster Size is Related to Cell Speed . . 140
4.3.5 NanoJ-Optofluidics Enables Dynamic and Multiplexed Super-Resolution Imaging . . . 141
4.4 Attributions . . . 143
4.5 Methods . . . 144
4.5.1 Cell Culture and Plasmid Transfection . . . 144
4.5.2 Microscopy . . . 145
4.5.3 Immuno-staining . . . 146
4.5.4 Sequential Labelling . . . 147
4.5.5 Data Processing and Analysis . . . 147
4.6 Bibliography . . . 149

5 Concluding remarks **150**
5.1 Bibliography . . . 153

Appendices **154**

A Acronyms **154**

List of Figures

1.1 Demonstration of resolution by the Rayleigh criterion 15
1.2 Schematic illustration of a SML microscopy acquisition. 20
1.3 Making PDMS devices 33

2.1 Dependence of the angle of incidence on the BFP 39
2.2 Cross-Correlation drift correction by Static Reference 44
2.3 Illustrative diagram of the MIM microscope 46
2.4 Photograph of the microscope stand 47
2.5 Laser Combiner 50
2.6 TIRF illuminator 51
2.7 Demonstration of TIRF 51
2.8 Vibration pattern of the multi-mode fibre 53
2.9 Vibration motor sequence 53
2.10 Field of view uniformity 54
2.11 Emission splitter path 57
2.12 Dual camera imaging 58
2.13 Axial drift in the Alpha 59
2.14 ASI CRISP 60
2.15 Diagram of the optical path for the drift correction hardware. 61
2.16 Image Processing for Cross Correlation 63
2.17 Measurement of drift with CCSR 64
2.18 Sensitivity of the Cross Correlation by Static Reference algorithm . 65
2.19 Vibrations in the Alpha 66
2.20 Drift Correction Plugin for Micro-Manager 67

2.21 dSTORM with drift correction 69
2.22 High-Speed dSTORM imaging 70

3.1 Peristaltic and syringe pump diagrams 82
3.2 NanoJ-Optofluidics pump device diagrams 87
3.3 Liquid exchange with NanoJ-Optofluidics 88
3.4 3D printed prototype 90
3.5 Exponential growth of Arduino in science 91
3.6 NanoJ-Optofluidics control systems 92
3.7 NanoJ-Optofluidics hardware on commercial systems 93
3.8 Fluidics connectors use with silica capillaries 98
3.9 Staining using NanoJ-Optofluidics and a PDMS device 98
3.10 No-Flow PDMS device designs 99
3.11 Dish-based fluidics device 101
3.12 Staining using NanoJ-Optofluidics and dish-based design 105

4.1 Acidic buffer elution 124
4.2 Acid treated cells being washed away in a PDMS device 124
4.3 madSTORM buffer elution 125
4.4 Exchange-PAINT proof of principle 127
4.5 NanoJ-Optofluidics enable multi-modal super-resolution imaging . . 128
4.6 Online fixation reveals mechanism for mitotic adhesion 131
4.7 Interphase integrin signal corresponds to focal adhesion sites 132
4.8 T-Cell speed correlates with number of LFA clusters 133

List of Tables

2.1 Laser lines on the Alpha 48

2.2 Laser combiner illumination intensity loss 52

2.3 FOV versus illumination intensity 55

2.4 Throughput comparison between the Alpha and commercial systems 72

3.1 Flow-rates obtained with BD Plastipak syringes 89

4.1 Correlations between number of clusters and cell speed 134

Chapter 1

Introduction

1.1 Resolution in Light Microscopy

Since the advent of the microscope's invention, the minimum resolvable detail that could be discerned has been truncated to around 200 nanometres (Rino et al., 2009). Light, as it passes through the optical elements of a microscope, gets diffracted. As a consequence, even if light is generated from an infinitesimally small point in space, an image will be blurred into a spot of limited diameter, with a pattern of concentric rings surrounding it (figure 1.1 A, B). This pattern was first observed in telescope images and the central spot is named the Airy disk, after George Biddell Airy who made the first theoretical description of it. (Cox, 2010).

After Airy, Lord Rayleigh (John William Strutt), formulated an estimate of the minimum detail that could be observed with a telescope, or in other words, its resolution. The resolution of a system is defined as the minimum distance at which two spots or objects can be resolved from each other. Therefore, the larger the diameter of the image of a spot (the airy disk), the larger the distance, and the worse the resolution of a system. To calculate the resolution of a microscope, Rayleigh empirically formulated equation (1.1) which estimates the radius of an airy disk.

$$d = \frac{0.61\lambda}{NA} \tag{1.1}$$

Where λ is wavelength and NA the numerical aperture of the lens. He posited that when the centre of one airy disk lies between the centre and the first minimum

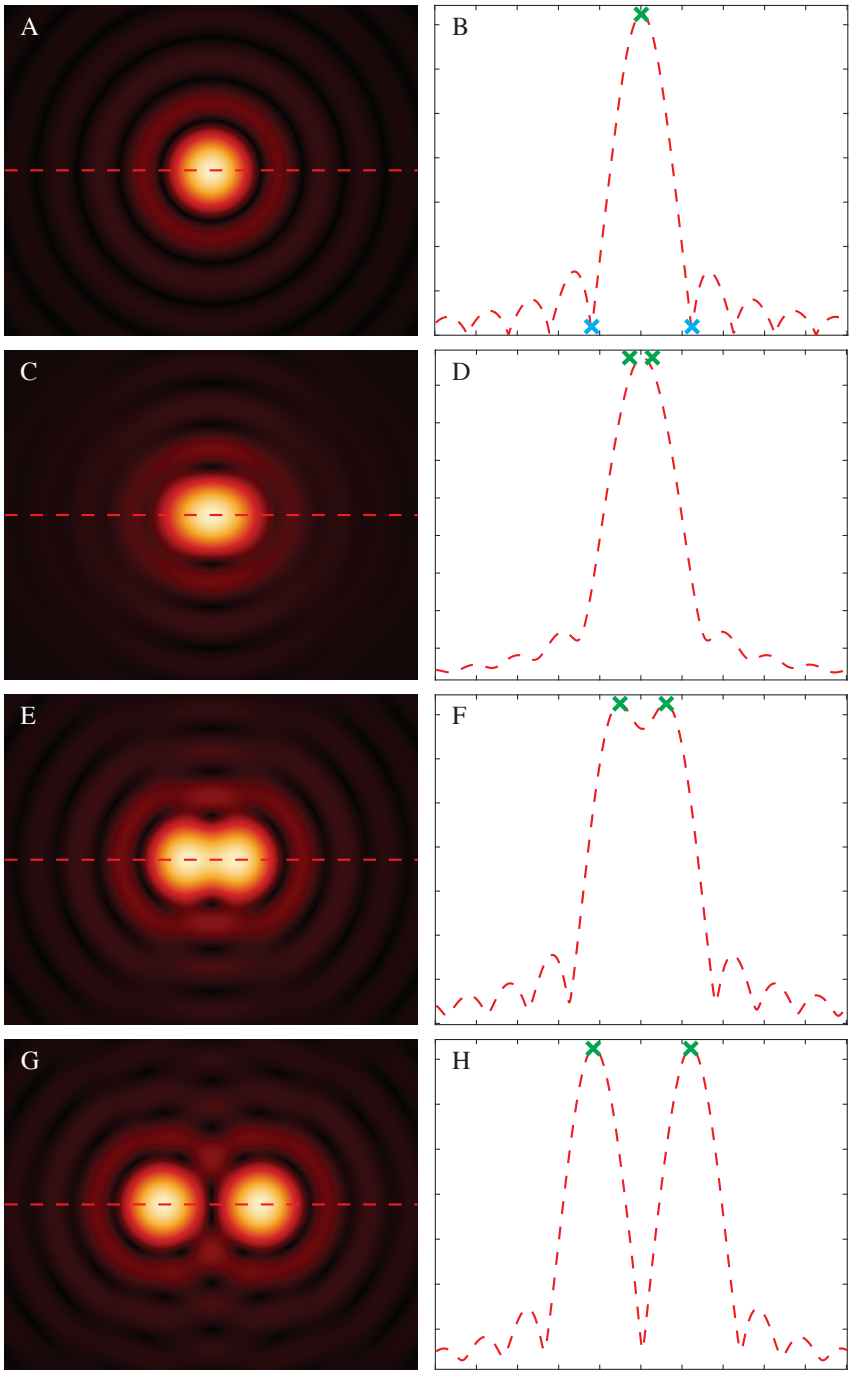

Figure 1.1: Demonstration of resolution by the Rayleigh criterion. Green crosses - spot locations; Blue crosses - first minimums; Dotted lines in A,C,E and G are plotted in B,D,F and H, respectively. The distance between the centre and the first minimum of an Airy disk is the Rayleigh resolution (B). The airy disk of a single infinitesimal spot (A, B) is indistinct from that of two spots lying at half the Rayleigh distance (C, D). But they can be distinguished at the Rayleigh distance (E, F) or any value above it (G, H).

of another airy disk (figure 1.1), that is when either could no longer be distinguished from each other. The distance between the first minimum and the centre of the disk would be the minimum distance where two spots could still be distinguished. This is called the Rayleigh resolution criterion (Cox, 2010). This meant that the radius of a spot could be used as an estimate of the maximum resolution obtainable when looking at bright spots in dark backgrounds, which is the case in astronomy but also in fluorescence microscopy. There are other analytical definitions of resolution such as the Abbe or sparrow criterion (Cox, 2010). However, since Rayleigh was looking at bright spots in a dark background, his criterion has become the standard estimator of the resolution of a fluorescence imaging microscope. By applying the Rayleigh criterion to visible light wavelengths and common objective NA, the value of 200nm has become the standard estimate of the maximum resolution a visible light microscope can achieve (Pawley, 2006).

The diffraction limit of light has meant light microscopes are inherently incapable of imaging details and interactions at the level of single molecules as these are often an order of magnitude, or more, smaller. For example, the diameter of a microtubule is 25nm (Wade, 2009), chromatin fibres have a width of 30nm (Robinson et al., 2006), and the prokaryotic ribosome has a diameter of circa 20nm (Alberts et al., 2002).

Diffraction occurs when an aperture lies on the path of any particles with wave properties. Photons fall under this category, but so do electrons. From equation (1.1) one can surmise that by using particles with smaller wavelengths than photons, like electrons, one can image with better resolution. Indeed, that is the motivation behind the development of Electron Microscopy (EM). EM microscopes can reach practical atomic resolutions as low as 0.1nm, but in practice electron microscopes routinely achieve resolutions of around 2nm in cellular samples (Alberts et al., 2002). This is 2 orders of magnitude better than even the best light microscope. However, the sample preparation methods for EM imaging of cells are lengthy, difficult, artefact prone, limited to thin cross-sections and strictly limited to fixed samples (Herbert et al., 2012; Alberts et al., 2002). Moreover, while EM samples

can be labelled specifically using immuno-gold techniques, the antigens available for labelling are much reduced when in comparison to fluorescence microscopy, reducing sensitivity, and the ability to reconstruct protein distribution (Alberts et al., 2002). Given the trade-off's inherent to EM imaging, there has been considerable interest in enhancing the resolution achievable with a light microscope in order to approach the resolution of EM while retaining good labelling characteristics.

1.2 Super-Resolution Fluorescence Microscopy

This interest has led to the development of a set of techniques collectively known as Super-Resolution (SR) microscopy (Schermelleh et al., 2010). There have been many methods developed that claim to achieve SR imaging (i.e. <200nm), but three have achieved widespread adoption: Stimulated Emission Depletion (STED) microscopy; Structured Illumination Microscopy (SIM); and Single Molecule Localization Microscopy (SMLM).

STED microscopy uses the principle of stimulated emission depletion (Hell et al., 1994). When a fluorophore is in the excited state (i.e., it has been excited by a photon), it can be stimulated to drop its energy to a ground state by an incoming photon of an appropriate wavelength. The resulting stimulated emission will have the same wavelength and direction as the stimulating photon (Pawley, 2006). A STED microscope is based on the confocal microscope, where the excitation laser is focused to a diffraction-limited spot, which is scanned through the sample in a raster pattern (Cox, 2010). The resulting emitted fluorescence is captured by a detector, and the image is constructed point-by-point. In STED microscopy, two lasers are used: one to excite fluorophores and another to deplete their emission (Hell et al., 1994). While the excitation laser will focus to a normal, diffraction-limited spot, the depletion laser is shaped into a doughnut pattern that is superimposed to the excitation spot. The result is that all the fluorophores under the doughnut pattern will be forced to emit in a specific wavelength, which is filtered out. The fluorophores in the centre of the doughnut will be allowed to emit in their normal emission spectrum. Since the emitting area corresponding to the centre of the doughnut will be significantly smaller than the diffraction limit of light, SR imaging is achieved in this way (Hell et al., 1994). The resolution achievable with STED is theoretically unlimited. Under ideal conditions, STED has been shown to achieve resolutions as low as 6nm (Rittweger et al., 2009), but in biological samples it is limited by a few factors: First, there is a limit to how many photons can emit in a quantity that is sufficient to detect in such a small focal volume (Pawley, 2006); Second, it is hampered by the imperfections in the optics that distort the doughnut-pattern as well

as the super-position of both lasers (Gould et al., 2012); Third, the photochemistry of many fluorophores and their local micro-environment does not allow efficient depletion, restricting STED to a specific selection of fluorophores and mounting media (Bouzin et al., 2013); Finally, because of the two laser wavelengths and the possibility of cross-talk, multi-colour STED is severely limited. Despite this, STED can routinely achieve resolutions of around 60 to 70nm (Almada et al., 2015).

Like STED, SIM is based on structuring the illumination of a microscope to achieve SR. Its principle is based on the concept of Moiré patterns (M. Gustafsson, 2000). These mathematically predictable patterns emerge whenever two patterns or structures super-impose on each other. In a fluorescence microscope, if its illumination is patterned with a known structure, Moiré patterns will emerge on the fluorescence image. The sample contains structural detail that is smaller than the diffraction limit of light, which means it can't be captured by the microscope. However, the Moiré patterns that result from the interaction of the structured illumination with the sample will have sizes that allow them to be captured in the fluorescence image. Since the pattern that is imposed on the sample is known, the underlying structural detail can then be mathematically reconstructed from these patterns (M. Gustafsson, 2000). The Moiré pattern will depend on both the phase and orientation of the illuminating pattern so each Moiré will only provide information for that particular phase and orientation. To fully reconstruct the SR image, a series of translations and rotations of the pattern need to be performed. At a minimum, three translations and three rotations are required. Combined, this means at least 9 raw images are necessary for a meaningful reconstruction. Despite this, SIM is the fastest technique of three mentioned technologies (Almada et al., 2015). It also makes no constraint on the sample or fluorophore choice, making it widely applicable. However, because the structuring that can be applied to the illumination pattern is itself limited by diffraction, SIM can only achieve a doubling of resolution (i.e., from 200 to 100nm). The fact that it depends on a mathematical reconstruction process also makes it artefact prone (Ball et al., 2015; Schaefer et al., 2004).

While SIM and STED structure the microscope illumination spatially, SML

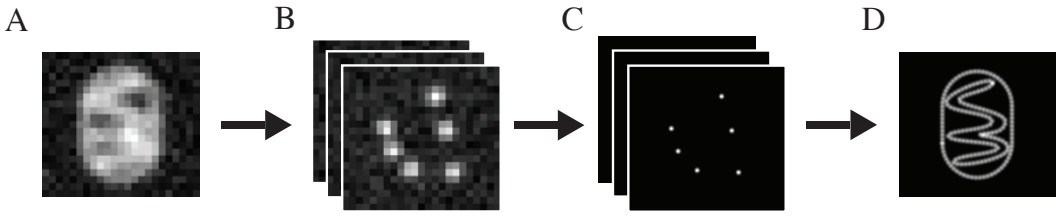

Figure 1.2: Schematic illustration of a SML microscopy acquisition. Adapted from Herbert et al. (2012). A - Simulation of a widefield diffraction limited image of a fluorescent sample; All fluorophores are emitting simultaneously, which doesn't allow them to be individually discriminated; B - SML microscopy techniques separate the emission in time so that tens of thousands of frames of different subsets of single molecules can be acquired; C - Each single molecule is identified and localised with high-precision from each of the raw frames; D - By plotting the locations of all the localisations, a SR reconstruction of the sample can be achieved.

microscopy structures the fluorescence emission temporally. The concept underlying SML is that two or more molecules that are spaced at a distance shorter than the resolution of the microscope cannot be resolved if they emit light simultaneously. However, if only one of the molecules is emitting light, the Airy disk can be clearly resolved. This allows the position of the single molecule to be estimated accurately. There have been several SML techniques developed, but almost all rely on trying to separate the emission of fluorophores over a period of time, in order to image non-overlapping single molecules. This usually requires acquiring several tens of thousands of images of single molecules. Each molecule is later fitted to a function approximating the Airy disk shape, such as a Gaussian function. From this fit, the estimated position of the molecule can be recovered with a precision that is greater than the resolution of the microscope (Thompson et al., 2002). From these recovered positions, a SR reconstruction can be made (figure 1.2). There are two main techniques to separate the fluorophore's emission in time: Photoactivated Localization Microscopy (PALM)(Betzig et al., 2006), and direct Stochastic Optical Reconstruction Microscopy (dSTORM) (Heilemann, Sebastian Linde et al., 2008).

PALM is based on the use of photo-activatable or photo-convertible fluorescent proteins. These proteins can change emission state when exposed to an Ultra-Violet (UV) light pulse; photo-activatable proteins change from a dark to a bright-state and photo-convertible proteins change from one colour to another. By exposing the

sample to a low intensity UV pulse, in the range of milliseconds, only a small and random subset of the fluorescent proteins will change state (Betzig et al., 2006). These altered proteins can be imaged specifically as single molecules, and their signal can subsequently be bleached. This process of UV pulsing, imaging and bleaching can be repeated several thousands of times until most of the fluorescent proteins have been imaged. While PALM uses fluorescent proteins, dSTORM uses organic fluorophores, such as Alexa Fluor and Cyanine (Cy) dyes, whose emission can be turned on and off stochastically. Bates, Blosser et al. (2005) first observed that, by pairing two dyes with distinct, but close, emission spectra the fluorescence emission could be selectively activated by excitation with one wavelength, and inactivated with another. These optical switches became the base for the first STORM modality (Rust et al., 2006; Bates, B. Huang et al., 2007). By using these dye-pairs, super-resolution can be achieved by alternating pulses of activating and inactivating laser-light to generate a blinking sequence. Heilemann, Margeat et al. (2005) then observed that, by using an oxygen-scavenging buffer in conjunction with a thiol, such as β-mercaptoethylamine, organic fluorophores can blink naturally when illuminated with intense laser light (i.e., $> 1\,\mathrm{kW\,cm^{-2}}$ to $2\,\mathrm{kW\,cm^{-2}}$; Sebastian Linde, Löschberger et al., 2011). By exploiting this property, dSTORM simplified the STORM procedure by requiring only one dye, a specific buffer and a strong illumination laser (Linde et al., 2008; Sebastian Linde, Löschberger et al., 2011). The inherent photochemistry of most fluorescent molecules commonly used in dSTORM allows them to easily enter long-lived dark states when in such conditions, and these states are reversible as opposed to bleaching. Dyes can also be induced to re-enter an activated state through excitation with UV or near UV light. This enables most dSTORM systems to modulate the switching behaviour of fluorophores by adjusting both the excitation laser and UV laser intensity. In both PALM and dSTORM, the resulting image stack consist largely of single molecules appearing in one frame and disappearing in the next. Most of these molecules will be separated from each other by a distance greater than the resolution of the microscope, even though some will inevitably lie at a smaller distance. The apparent turning on and off of the

molecules is generally referred to as blinking. A localisation algorithm will then attempt to identify and discard any overlapping molecules and precisely locate all the single molecules present in the image stack. The result of an SML experiment is not an image in the traditional sense, but a table of localisations from which a SR reconstruction can be made. The resolution of a SMLM dataset will depend on both the labelling density and on the localisation precision that can be achieved for each molecule (Sebastian van de Linde, Wolter et al., 2010). This precision is proportional to the Signal-to-Noise Ratio (SNR) (Thompson et al., 2002). Therefore, the number of photons (the signal) that can be captured from a single molecule will determine the final resolution of a SML experiment. For this reason, PALM cannot achieve the same resolution as dSTORM since fluorescent proteins are generally less brighter than organic fluorophores by almost an order of magnitude (Henriques et al., 2009). dSTORM experiments can routinely achieve resolutions of around 20 to 30nm (Almada et al., 2015) which surpasses either STED or SIM. Because the main requirements for dSTORM are only a powerful illumination system, a sensitive camera and a tailored buffer, it is also the simplest method to implement in almost any microscope. However, SMLM in general requires tens of thousands of frames to be acquired therefore it is also traditionally the slowest of the three techniques (Almada et al., 2015).

1.3 High-Throughput Single Molecule Localisation Microscopy

The resolution afforded by SMLM has enabled researchers to make biological discoveries previously obscured by the diffraction limit of fluorescence microscopy. For example, some signalling receptors have been found to group into nano-scale clusters (Lillemeier et al., 2010). SMLM imaging of cellular adhesions has shown their components are organized in discrete layers at different distances from the membrane (Kanchanawong et al., 2010; Case et al., 2015; Bertocchi et al., 2017). The bacterial Ftsz protein was thought to organise as a ring structure, until PALM data revealed it actually organises as discontinuous filaments (Buss et al., 2013; Holden, Pengo et al., 2014). High-throughput SMLM imaging can also overcome some of the limitations from SMLM, namely that structures can be discontinuous due to the imaging process' nature. In this work, throughput is defined as the rate at which a system can acquire data and a high-throughput work-flow as an automated and significantly fast acquisition of a large number of datasets. For example, using such a system, Szymborska et al. (2013) averaged many dSTORM data-sets, enabling them to establish a model of the organization of the nuclear pore complex. High-throughput SMLM imaging can also enable experiments which are otherwise too onerous to perform manually. Soares et al. (2013), by using an automated system, were able to observe nano-scale reorganisation of cellular receptors due to vesicle trafficking. However, the slow speed of SMLM acquisitions severely limits its applicability for high-throughput experiments. To overcome this, the overall throughput of SMLM can be increased in two ways. First, one can decrease the time required for a single SMLM acquisition. Secondly, one can increase the amount of data that can be acquired in parallel in a SMLM experiment.

To reduce the total acquisition time, one can decrease the overall number of frames needed for an SMLM reconstruction. The simplest way to achieve this is to use analysis algorithms that are capable of localising overlapping molecules with SR precision. This means highly dense datasets can be acquired, where a single

frame can have orders of magnitude more single molecules emitting in it. There have been several new SR algorithms designed to achieve this goal (Dertinger et al., 2010; Holden, Uphoff et al., 2011; Munck et al., 2012; N. Gustafsson et al., 2016); However, even if an algorithm can distinguish between two molecules that overlap, when one molecule overlaps with another, it will increase the background for its neighbour and vice-versa. This reduces the overall SNR, which explains why most of these algorithms achieve faster acquisition times but at a trade-off to resolution.

Instead of reducing the number of frames, one can also increase the camera's frame-rate and decrease the overall acquisition time proportionally. But different camera technologies are limited in what frame-rates they can achieve. To acquire signals from single molecules efficiently, a SMLM microscope needs to have a camera that is sensitive enough to detect low light levels. This is usually achieved by the use of cameras with Electron-Multiplying Charge-Coupled Device (EM-CCD) sensors. Charge-Coupled Device sensors consist of an array of pixels that convert photons to an electric charge through the photo-electric effect (Moomaw, 2013). These are then converted to a digital signal, one by one, through the read-out stage of the camera. There is some noise associated with this stage of the process, meaning it adds a small random number of electrons to the output signal. If the light on the sensor produces less charge than the read-out noise of the camera, then it can't be detected (Pawley, 2006). EM-CCD's can solve this issue by having an electron multiplication stage added before the read-out stage. The amplification stage consists of a series of steps that amplify the electrons coming from the sensor to levels that are orders of magnitude larger than the read-out noise, essentially obviating it (Robbins et al., 2003). As a result, EM-CCD cameras can have single-photon sensitivity. The measure of the percentage of light that is captured by the sensor and converted to electronic charge is called the Quantum Efficiency (QE), and the QE of common EM-CCD cameras is 90% (Andor Technology Ltd, 2016b; Hamamatsu Photonics K.K., 2017; Photometrics, 2017), making them one of the most sensitive detectors available. This is what makes EM-CCD the most common sensor technology traditionally used in SMLM experiments (Chen et al., 2016). Because the

electron-multiplying process of an EM-CCD has a fixed uncertainty associated with it, it reduces the overall SNR of the camera by $\sqrt{2}$. Additionally, because each pixel has to be read one by one, the larger the number of pixels, the slower the acquisition speed. Therefore, a camera model with a Field-Of-View (FOV) of 512x512 pixels can acquire at a maximum of 56 Frames Per Second (FPS) (i.e. 12 min. to collect a typical sized dataset with 40.000 frames), but a different model with a FOV of 1024x1024 pixels can acquire only at 26 FPS (Andor Technology Ltd, 2016b).

Recently, advances in sensor and manufacturing processes has led to the development of a new type of scientific imaging sensors called scientific Complementary Metal Oxide Semiconductor (sCMOS). These are designed to have a QE of over 82% and very small ($\sim 1e^{-}$) read-noise (Andor Technology Ltd, 2016a; Hamamatsu Photonics K.K., 2016), almost matching the specifications of an EM-CCD. Because they do not have an electron-multiplying stage that can reduce the overall SNR, sCMOS cameras perform either comparably or better than EM-CCD's in the moderate light intensities typical of SMLM experiments (Beier et al., 2014; Fullerton et al., 2012; F. Huang et al., 2013; Z.-L. Huang et al., 2011; Long et al., 2012; Saurabh et al., 2012). sCMOS sensors also differ from EM-CCD's in that instead of all the pixels in the array being read one by one in a single read-stage, each line of the pixel array is read in parallel instead. This results in higher frame-rates for much larger acquisitions areas. A typical sCMOS sensor used in SMLM with a QE of 82% has a FOV of 2048x2048 pixels and a top acquisition speed of 100 FPS (Andor Technology Ltd, 2016a; Hamamatsu Photonics K.K., 2016). For high-throughput microscopy, if our sample of interest is fairly evenly spread in the coverslip and it is significantly smaller than our FOV, then increasing the FOV can increase the overall throughput. The FOV of an sCMOS can cover up to 16x the FOV that an EM-CCD can cover. Combined with the fact it is twice as fast as an EM-CCD, this means the sCMOS sensor can potentially have a throughput increase of 32x, a large boost for high-throughput microscopy. The one caveat for using sCMOS sensors in SMLM is that, due to the different read-out stages for each column and due to unevenness in the manufacturing process, they have a non-uniform noise distribution that needs to

be accounted for in SR algorithms before performing a localisation analysis. However, the analytic methods needed to account for this patterning have been solved for SMLM imaging (F. Huang et al., 2013; Liu et al., 2017).

For dSTORM imaging specifically, a high laser illumination intensity is required to induce efficient blinking. This is because the rate at which fluorophores enter the long-lived dark (OFF) states is proportional to the exciting photon density. Simultaneously, the average time that a fluorophore spends on an emitting (ON) state is also reduced in high photon density conditions (Sebastian Linde, Löschberger et al., 2011). This is important for high-throughput dSTORM imaging since, as the camera frame-rate is increased, the average lifetime of the ON state should reduce accordingly to match the exposure time of a single frame. Otherwise the probability of imaging overlapping molecules increases. To design a dSTORM imaging system that fully benefits from sCMOS sensor technology, the illumination intensity needs to be sufficient to induce blinking across the entire FOV. Since this means the illumination needs to be spread across a larger FOV than a normal camera, the intensity rating of the lasers needs to be proportionally higher. Additionally, the non-uniformity of the illumination needs to be addressed. Most laser illumination systems for SMLM have a Gaussian illumination profile as they use critical illumination to maximise laser illumination intensity (Coumans et al., 2012; Almada et al., 2015). This means the centre of the FOV has a significant larger illumination intensity when compared to the edges of the FOV. In order to ensure that illumination intensity is sufficient to induce blinking throughout a large FOV, the laser illumination can be homogenised and to that end there exist many methods to homogenise a FOV, each with different advantages and disadvantages (Almada et al., 2015). Aside from decreasing the acquisition time, one can increase the throughput by acquiring more data in parallel, as was mentioned for the case of large FOV's. When studying a cellular process, several cellular components may play a role and a different fluorophore species is needed to tag each component of interest. Typically, SMLM imaging is performed by imaging one colour at a time. But one may parallelise a high-throughput system by simultaneously imaging more

than one fluorescent species at a time. This can be achieved by splitting the emission light between two cameras or to two halves of the same camera sensor. For two fluorophores that are spectrally distinct, such as Alexa Fluor 488 and Alexa Fluor 647, this means they can be successfully imaged in parallel, reducing the imaging time in half. While there are methods available to try and distinguish fluorophores whose spectra overlap (Testa et al., 2010; Winterflood et al., 2015), this is beyond the scope of this thesis.

1.4 Sequential Labelling

The above methods focus on how to accelerate a SMLM work-flow to enable high-throughput SR imaging. One may also consider, however, how to reduce the need to acquire large amounts of data in the first place. A major limitation of fluorescence microscopy is its spectral bandwidth limit. For one species of fluorophore to be discriminated from another both need to have their emission spectra sufficiently separated, enough to not have the spectra of one fluorophore cross-over into the range of another fluorophore. Most fluorophores emit light in a broad range of wavelengths and most microscope objectives only capture a finite range of visible light wavelengths, referred to as its spectral bandwidth. Taking both of these facts into account it becomes apparent that, at most, a fluorescence microscope can only image up to 4 fluorophores (Cox, 2010).

Because of the spectral bandwidth limit, a complex process with many interacting elements needs to be decomposed into smaller pairs of interactions in a fluorescence microscopy experiment. This means that in order to investigate a complex process requires many disconnected data-points that need to be correlated together with carefully planned controls. Relying on correlations introduces a degree of uncertainty to the analysis. However, this could be greatly minimised if the spectral bandwidth limit was overcome and all known relevant partners could be imaged simultaneously in a single cell.

In order to overcome the spectral bandwidth limit, several researchers have developed sequential labelling methods. These consist of a work-flow where a sample is labelled, imaged and then has its labelling removed to allow the process to be repeated. This can be done by either bleaching the fluorophore and leaving the labelling antibody in place (Gerdes et al., 2013; Lin et al., 2015; Schubert et al., 2006), by eluting the antibody away (Micheva et al., 2007; Murray et al., 2015; Wählby et al., 2002) or by denaturing the antibodies, allowing them to be washed away (Lin et al., 2015; Pirici et al., 2009; Wählby et al., 2002). Bleaching, elution and denaturing have all been demonstrated with SMLM techniques (Ku et al., 2016; Tam et al., 2014; Valley et al., 2015; Yi et al., 2016). With adequately fixed samples, the

sample can be relabelled for new targets and the process can be repeated a number of times (each step being generally referred to as a round). The process is primarily limited by the steric hindrance generated by accumulated labels (except when eluting), the stability of the sample throughout the process and the efficiency of the removal/bleaching of previously visualised labels. In this context, steric hindrance is the hindering of antibodies binding to antigens due to the proximity of other antibodies. Despite the possibility of steric hindrance and to disturb the sample, it has been shown that both cells and tissue slices can be sequentially labelled by chemical bleaching and maintain structural integrity over several rounds. Gerdes et al. (2013) studied up to 61 proteins in human colorectal cancer samples using this method. This allowed them to measure the degree of tumour heterogeneity, as well as reveal potential action mechanisms for the immuno-suppressant rapamycin. Schubert et al. (2006) labelled up to 90 proteins in human biopsies from patients and discovered putative rules for how protein networks organise as hierarchies. Furthermore, they identify there are disease specific network patterns for psoriasis, demonstrating the power of this approach to study human disease mechanisms.

Since the early days of immuno-staining, there are have been many published attempts at establishing sequential labelling protocols even before the use of fluorescent dyes became widespread. This was due to a lack of diversity of animal species from which antibodies could be reared (limiting multiplexing) and a lack of easily distinguishable fluorescent or coloured dyes (dyes which cause a specific colour to appear under transmitted light). Chromogenic dyes are, usually, enzymes which deposit coloured products in specific locations. Since these products are separate from the antibody used to label a sample, Nakane (1968) used a sequence of buffer solutions with high and low pH levels (ph 9 and 2) to elute antibodies from a chromogenically labelled sample while leaving the chromogenic dyes intact for a sequential triple labelling (Nakane, 1968). In 1975, Vandesande and Dierickx used a combination of a glycine buffer and dimethylformamide for a sequential double labelling (Vandesande et al., 1975) and in 1976 they added an electrophoresis step in the same buffer to achieve a more complete elution of high affinity antibodies

(Vandesande et al., 1976). Also in 1976, Erlandsen et al. used only a low pH solution to elute antibodies (Erlandsen et al., 1976) and in 1978, Tramu et al. used a high pH solution instead (Tramu et al., 1978). In 1986 Kolodziejczyk and Baertschi prove antibodies can be denatured using only heat (Kolodziejczyk et al., 1986), enabling triple labelling using antibodies raised only in rats. In 1993 Lewis Carl et al. demonstrate that by using antibody fragments to block sites where secondary antibodies might bind to, they can achieve dual labelling using only mouse monoclonal primary antibodies (Lewis Carl et al., 1993). More recently, Micheva et al. (2007) used the same method Tramu et al. established in 1978 to label up to 60 proteins in brain slices. These elution methods were established at a time when chromogenic dyes were favoured for immuno-histochemistry, but the use of fluorescent antibodies has opened the possibility to simply bleach a fluorophore away to perform sequential labelling. By using a microscope's illumination, Schubert et. al use a high-throughput system to image and bleach fluorophores between rounds, enabling up to 90 different proteins to be imaged (Schubert et al., 2006).

After SMLM was developed, dSTORM imaging is usually performed using only a single fluorophore, Alexa Fluor 647, because of it's brightness and amenable blinking characteristics (Dempsey et al., 2011). Other fluorophores have been tested for Super-Resolution SMLM imaging (Dempsey et al., 2011) but fail to achieve the same resolution that can be obtained with Alexa Fluor 647. This makes multi-colour SMLM difficult as one of the colours will be inherently lower resolution. To be able to use only Alexa Fluor 647 for imaging different targets, bleaching-based sequential labelling has been demonstrated for dSTORM imaging. Tam et al. (2014) imaged up to 4 proteins using when performing secondary labelling and Valley et al. (2015) was able to image 5 proteins using primarily labelled antibodies.

1.5 Fluidics for High-throughput Microscopy

Sequential labelling, then, is an attractive technique for high-throughput Super-Resolution Single Molecule imaging. But it is not without its drawbacks. If one were to perform a sequential labelling protocol manually, it would involve the following steps in between imaging sessions:

1. Remove the sample from the stage
2. Remove the prior label from the sample
3. Stain the sample for a new target
4. Replace the sample on the microscope
5. Find the previous regions of interest
6. Image the sample

If one were to simply perform the label removal and staining steps while the sample is still on the microscope, steps 1, 4 and 5 could be bypassed. These are manual steps which would otherwise prevent one from fully automating the protocol. For a high-throughput application of sequential-labelling, where the goal is to achieve the labelling of a large number of epitopes (ex. 25 to 100), it becomes ideal to perform the protocol automatically and *in-situ*. In general, immuno-labelling protocols can be summarised as a series of liquid exchange steps. Therefore, one must find a way to both remove and deliver liquids to a sample while it is on the microscope stage and one way to achieve this is through the use of fluidic technology (El-Ali et al., 2006; Sackmann et al., 2014; Duncombe et al., 2015).

Microfluidics are a large and varied set of technologies designed for fluid manipulation at the micro- and nano-litre scale (Duncombe et al., 2015; Sackmann et al., 2014). Fluid flow can be described using the Reynols number (equation (1.2)):

$$Re = \frac{\rho v D_h}{\mu} \tag{1.2}$$

Where ρ is the fluid density, v is the characteristic velocity of the fluid, D_h is the hydraulic diameter and μ is the fluid viscosity. When the Reynolds number is low (i.e. < 2300), the fluid flow is considered to be laminar, meaning there is essentially no turbidity. At the small scales of microfluidics devices, the fluid flow is largely laminar, making it highly predictable. Among other things, this enables laminar flows to be created (Beebe et al., 2002) which allow the manipulation of single cells (Reece et al., 2016), to control environmental properties such as shear flow stress (Polacheck et al., 2013) or create controlled concentration gradients (Duncombe et al., 2015). These techniques require closed systems where liquids can be exchanged and pressure can be applied in a controlled manner. The most common method to achieve this is through the use of Polydimethylsiloxane (PDMS) devices (Bhatia et al., 2014; Sackmann et al., 2014; Duncombe et al., 2015). PDMS is an elastomer that, using a chemical cross-linker, can be polymerised into an optically clear polymer. It has many attractive advantages:

- Gas- and vapour-permeable
- Same refractive index as glass
- Bio-compatible
- Tuneable elastic properties
- Can be covalently bonded to glass

For these reasons, it is the most popular material to build microfluidic devices with (Beebe et al., 2002; Sackmann et al., 2014; Duncombe et al., 2015; Reece et al., 2016).

Devices can be made with features as small as a couple of micrometres by pouring PDMS on a mould and allowing it to polymerise (figure 1.3 A,B). The mould's features are first designed on a computer and it is then fabricated using photo lithography techniques which were first developed for computer chip design (Bhatia et al., 2014; Sackmann et al., 2014). These features can, for example, be channels where cells are cultured and manipulated. For microscopy applications,

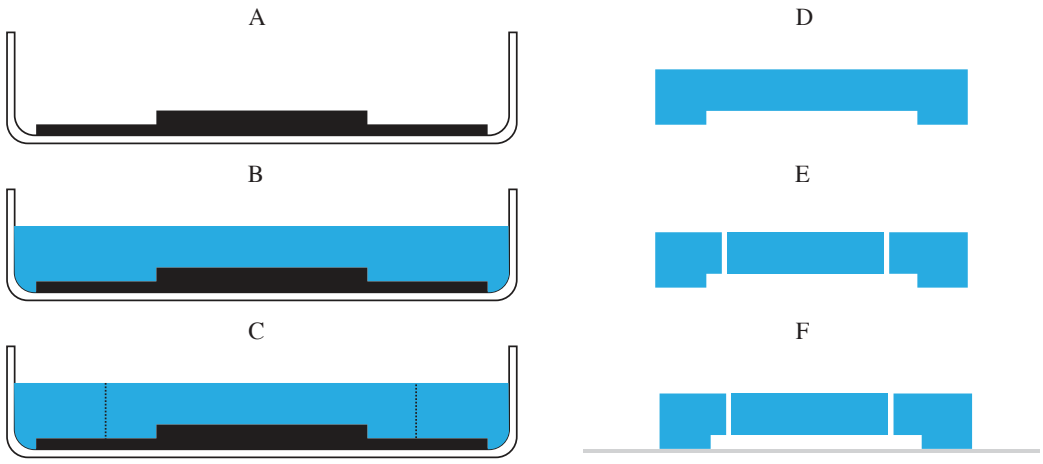

Figure 1.3: Steps required to make a PDMS microfluidic device. A - A mould (in blackk) is first placed in a container such as a 90mm diameter petri dish (in white); B - The PDMS is mixed with the curing agent and poured on the mould; C - After allowing the PDMS to cure, it can be cut (as shown by the dotted lines) and D - removed from the mould; E - Once removed, a few holes can be bored through the device to create inlets and outlets; F - Finally, the device can be plasma treated so it is covalently bonded to glass.

the device is removed from the mould (figure 1.3 C,D) and a few inlets are bored through the device (figure 1.3 E). The PDMS can then be activated through plasma treatment, allowing it to covalently bind to a coverslip surface (figure 1.3 F). Thus a self-contained device is made, with inlets and outlets for fluid exchange and a glass-bottom coverslip for microscopy imaging. Once the device has been made, the inlets and outlets can be fitted with adapters to accept tubing. Using syringes, liquid can then be removed or added to the microfluidic chamber, enabling us to perform complex staining and sequential labelling protocols *in-situ*.

1.6 Thesis Scope

The object of this thesis is to tie all three proposed methodologies (high-throughput super-resolution microscope design, sequential labelling and fluidics) into a single, unified framework for high-throughput super-resolution microscopy.

Chapter 2 will show the design and implementation steps for a custom large field-of-view super-resolution microscope, encompassing both the illumination and detection stages of the microscope. A large FOV illumination scheme is implemented to leverage the large FOV of an sCMOS camera. We also implement a custom drift-correction procedure to both reduce the amount of steps required in analysis as well as to enable consistent positioning through different rounds of sequential labelling.

Chapter 3 describes a fluidics framework (NanoJ-Optofluidics) for microscope *in-situ* fluidic manipulation of cells. A simple but highly multiplexed computer controlled pump array for liquid handling is demonstrated. To fully automate the hardware array, a complete software framework is shown that can be synchronised with the microscope acquisition software, enabling complete automation of the sequential labelling and acquisition process.

Chapter 4 will present a comparison of different sequential labelling techniques as applied to super-resolution microscopy. It will also demonstrate the application of the NanoJ-Optofluidics framework described in Chapter 3 for online fixation, sequential labelling and super-resolution imaging. Using NanoJ-Optofluidics for *in-situ* fixation and labelling, the system was able to show a link between mitotic adhesion of migratory cells and interphase focal adhesions. The combination of fixation, super-resolution imaging and sequential labelling is also used to investigate immune cell migration.

1.7 Bibliography

Alberts, Bruce et al. *Molecular Biology of the Cell*. 4th editio. New York: Garland Science, 2002, p. 1463. ISBN: 0815332181.

El-Ali, Jamil, Peter K Sorger and Klavs F Jensen. 'Cells on chips.' In: *Nature* 442.7101 (2006), pp. 403–411. ISSN: 0028-0836. DOI: 10.1038/nature05063.

Almada, Pedro, Siân Culley and Ricardo Henriques. 'PALM and STORM: Into large fields and high-throughput microscopy with sCMOS detectors.' In: *Methods (San Diego, Calif.)* 88 (Oct. 2015), pp. 109–21. ISSN: 1095-9130. DOI: 10.1016/j.ymeth.2015.06.004.

Andor Technology Ltd. *Andor Zyla 4.2 PLUS | sCMOS Camera for Light Sheet Microscopy | Andor*. 2016. URL: http://www.andor.com/scientific-cameras/neo-and-zyla-scmos-cameras/zyla-42-plus-scmos (visited on 06/02/2017).

— *iXon EMCCD Cameras | Andor*. 2016. URL: http://www.andor.com/cameras/ixon-emccd-camera-series (visited on 10/02/2017).

Ball, Graeme et al. 'SIMcheck: a Toolbox for Successful Super-resolution Structured Illumination Microscopy.' In: *Scientific reports* 5 (2015), p. 15915. ISSN: 2045-2322. DOI: 10.1038/srep15915. arXiv: arXiv:1011.1669v3.

Bates, Mark, Timothy R Blosser and Xiaowei Zhuang. 'Short-range spectroscopic ruler based on a single-molecule optical switch.' In: *Physical review letters* 94.10 (Mar. 2005), p. 108101. ISSN: 0031-9007. DOI: 10.1103/PhysRevLett.94.108101.

Bates, Mark, Bo Huang et al. 'Multicolor super-resolution imaging with photo-switchable fluorescent probes.' In: *Science (New York, N.Y.)* 317.5845 (Sept. 2007), pp. 1749–53. ISSN: 1095-9203. DOI: 10.1126/science.1146598.

Beebe, David J., Glennys A. Mensing and Glenn M. Walker. 'Physics and Applications of Microfluidics in Biology'. In: *Annual Review of Biomedical Engin-*

eering 4.1 (Aug. 2002), pp. 261–286. ISSN: 1523-9829. DOI: 10.1146/annurev.bioeng.4.112601.125916.

Beier, Hope T and Bennett L Ibey. 'Experimental comparison of the high-speed imaging performance of an EM-CCD and sCMOS camera in a dynamic live-cell imaging test case.' In: *PloS one* 9.1 (Jan. 2014), e84614. ISSN: 1932-6203. DOI: 10.1371/journal.pone.0084614.

Bertocchi, Cristina et al. 'Nanoscale architecture of cadherin-based cell adhesions.' In: *Nature cell biology* 19.1 (Jan. 2017), pp. 28–37. ISSN: 1476-4679. DOI: 10.1038/ncb3456.

Betzig, Eric et al. 'Imaging intracellular fluorescent proteins at nanometer resolution.' In: *Science (New York, N.Y.)* 313.5793 (Sept. 2006), pp. 1642–5. ISSN: 1095-9203. DOI: 10.1126/science.1127344.

Bhatia, Sangeeta N and Donald E Ingber. 'Microfluidic organs-on-chips'. In: *Nat Biotech* 32.8 (2014), pp. 760–772. ISSN: 1087-0156. DOI: 10.1038/nbt.2989[doi]. arXiv: 1408.1149.

Bouzin, M et al. 'Stimulated emission properties of fluorophores by CW-STED single molecule spectroscopy.' In: *The journal of physical chemistry. B* 117.51 (2013), pp. 16405–15. ISSN: 1520-5207. DOI: 10.1021/jp409330t.

Buss, Jackson et al. 'In vivo organization of the FtsZ-ring by ZapA and ZapB revealed by quantitative super-resolution microscopy.' In: *Molecular microbiology* 89.6 (Sept. 2013), pp. 1099–120. ISSN: 1365-2958. DOI: 10.1111/mmi.12331.

Case, Lindsay B et al. 'Molecular mechanism of vinculin activation and nano-scale spatial organization in focal adhesions.' In: *Nature cell biology* 17.7 (July 2015), pp. 880–92. ISSN: 1476-4679. DOI: 10.1038/ncb3180.

Chen, Xuanze et al. 'Superior performance with sCMOS over EMCCD in super-resolution optical fluctuation imaging'. In: *Journal of Biomedical Optics* 21.6 (2016), p. 066007. ISSN: 1083-3668. DOI: 10.1117/1.JBO.21.6.066007.

Coumans, Frank a W, Edwin van der Pol and Leon W M M Terstappen. 'Flat-top illumination profile in an epifluorescence microscope by dual microlens arrays.' In: *Cytometry. Part A : the journal of the International Society for Analytical Cytology* 81.4 (Apr. 2012), pp. 324–31. ISSN: 1552-4930. DOI: 10.1002/cyto.a.22029.

Cox, Guy. *Optical Imaging Techniques in Cell Biology, Second Edition*. CRC Press, 2010, p. 316. ISBN: 1439848254.

Dempsey, Graham T et al. 'Evaluation of fluorophores for optimal performance in localization-based super-resolution imaging.' In: *Nature methods* 8.12 (Dec. 2011), pp. 1027–36. ISSN: 1548-7105. DOI: 10.1038/nmeth.1768.

Dertinger, Thomas et al. 'Achieving increased resolution and more pixels with Superresolution Optical Fluctuation Imaging (SOFI).' In: *Optics express* 18.18 (Aug. 2010), pp. 18875–18885. ISSN: 1094-4087.

Duncombe, Todd A., Augusto M. Tentori and Amy E. Herr. 'Microfluidics: reframing biological enquiry.' In: *Nature reviews. Molecular cell biology* 16.9 (Sept. 2015), pp. 554–67. ISSN: 1471-0080. DOI: 10.1038/nrm4041.

Erlandsen, S L et al. 'Pancreatic islet cell hormones distribution of cell types in the islet and evidence for the presence of somatostatin and gastrin within the D cell.' In: *The journal of histochemistry and cytochemistry : official journal of the Histochemistry Society* 24.7 (1976), pp. 883–897. ISSN: 00221554.

Fullerton, Stephanie et al. 'Optimization of Precision Localization Microscopy using CMOS Camera Technology'. In: ed. by Jörg Enderlein et al. Feb. 2012, 82280T–82280T–10. DOI: 10.1117/12.906336.

Gerdes, Michael J. et al. 'Highly multiplexed single-cell analysis of formalin-fixed, paraffin-embedded cancer tissue.' In: *Proceedings of the National Academy of Sciences of the United States of America* 110.29 (July 2013), pp. 11982–7. ISSN: 1091-6490. DOI: 10.1073/pnas.1300136110.

Gould, Travis J et al. 'Adaptive optics enables 3D STED microscopy in aberrating specimens.' In: *Optics express* 20.19 (Sept. 2012), pp. 20998–1009. ISSN: 1094-4087.

Gustafsson, Mats. 'Surpassing the lateral resolution limit by a factor of two using structured illumination microscopy.' In: *Journal of microscopy* 198.Pt 2 (May 2000), pp. 82–7. ISSN: 0022-2720. DOI: 10.1046/j.1365-2818.2000.00710.x.

Gustafsson, Nils et al. 'Fast live-cell conventional fluorophore nanoscopy with ImageJ through super-resolution radial fluctuations'. In: *Nature Communications* 7 (Aug. 2016), p. 12471. ISSN: 2041-1723. DOI: 10.1038/ncomms12471.

Hamamatsu Photonics K.K. *ImagEM X2 EM-CCD camera C9100-23B | Hamamatsu Photonics*. URL: https://www.hamamatsu.com/jp/en/community/life_science_camera/product/search/C9100-23B/index.html (visited on 12/06/2017).

— *ORCA-Flash4.0 V2 Digital CMOS camera C11440-22CU | Hamamatsu Photonics*. 2016. URL: https://www.hamamatsu.com/us/en/product/category/5000/5005/C13440-20CU/index.html (visited on 10/02/2017).

Heilemann, Mike, Sebastian Linde et al. 'Subdiffraction-resolution fluorescence imaging with conventional fluorescent probes.' In: *Angewandte Chemie (International ed. in English)* 47.33 (Jan. 2008), pp. 6172–6. ISSN: 1521-3773. DOI: 10.1002/anie.200802376.

Heilemann, Mike, Emmanuel Margeat et al. 'Carbocyanine Dyes as Efficient Reversible Single-Molecule Optical Switch'. In: *Journal of the American Chemical Society* 127.11 (Mar. 2005), pp. 3801–3806. ISSN: 0002-7863. DOI: 10.1021/ja044686x.

Hell, S W and J Wichmann. 'Breaking the diffraction resolution limit by stimulated emission: stimulated-emission-depletion fluorescence microscopy.' In: *Optics letters* 19.11 (June 1994), pp. 780–782. ISSN: 0146-9592. DOI: 10.1364/OL.19.000780.

Henriques, Ricardo and Musa M Mhlanga. 'PALM and STORM: what hides beyond the Rayleigh limit?' In: *Biotechnology journal* 4.6 (June 2009), pp. 846–57. ISSN: 1860-7314. DOI: 10.1002/biot.200900024.

Herbert, Sébastien et al. 'Single-molecule localization super-resolution microscopy: deeper and faster.' In: *Microscopy and microanalysis : the official journal of Microscopy Society of America, Microbeam Analysis Society, Microscopical Society of Canada* 18.6 (Dec. 2012), pp. 1419–29. ISSN: 1435-8115. DOI: 10.1017/S1431927612013347.

Holden, Seamus J, Thomas Pengo et al. 'High throughput 3D super-resolution microscopy reveals Caulobacter crescentus in vivo Z-ring organization.' In: *Proceedings of the National Academy of Sciences of the United States of America* 111.12 (2014), pp. 4566–71. ISSN: 1091-6490. DOI: 10.1073/pnas.1313368111.

Holden, Seamus J, Stephan Uphoff and Achillefs N Kapanidis. 'DAOSTORM: an algorithm for high- density super-resolution microscopy.' In: *Nature methods* 8.4 (Apr. 2011), pp. 279–80. ISSN: 1548-7105.

Huang, Fang et al. 'Video-rate nanoscopy using sCMOS camera-specific single-molecule localization algorithms.' In: *Nature methods* 10.7 (July 2013), pp. 653–8. ISSN: 1548-7105. DOI: 10.1038/nmeth.2488.

Huang, Zhen-Li et al. 'Localization-based super-resolution microscopy with an sCMOS camera'. In: *Optics Express* 19.20 (2011), p. 19156. ISSN: 1094-4087. DOI: 10.1364/OE.19.019156.

Kanchanawong, Pakorn et al. 'Nanoscale architecture of integrin-based cell adhesions.' In: *Nature* 468.7323 (2010), pp. 580–584. ISSN: 1476-4687. DOI: 10.1038/nature09621.

Kolodziejczyk, E. and a. J. Baertschi. 'Multiple immunolabeling in histology: a new method using thermo-inactivation of immunoglobulins.' In: *The journal of histochemistry and cytochemistry : official journal of the Histochemistry Society* 34.12 (Dec. 1986), pp. 1725–9. ISSN: 0022-1554. DOI: 10.1177/34.12.3023476.

Ku, Taeyun et al. 'Multiplexed and scalable super-resolution imaging of three-dimensional protein localization in size-adjustable tissues'. In: *Nature Biotech-*

nology In press.November 2015 (2016), doi:10.1038/nbt.3641. ISSN: 1087-0156. DOI: 10.1038/nbt.3641.

Lewis Carl, S. a., I. Gillete-Ferguson and D. G. Ferguson. 'An indirect immunofluorescence procedure for staining the same cryosection with two mouse monoclonal primary antibodies.' In: *Journal of Histochemistry & Cytochemistry* 41.8 (Aug. 1993), pp. 1273–1278. ISSN: 0022-1554. DOI: 10.1177/41.8.7687266.

Lillemeier, Björn F et al. 'TCR and Lat are expressed on separate protein islands on T cell membranes and concatenate during activation.' In: *Nature immunology* 11.1 (Jan. 2010), pp. 90–6. ISSN: 1529-2916. DOI: 10.1038/ni.1832.

Lin, Jia Ren, Mohammad Fallahi Sichani and Peter K Sorger. 'Highly multiplexed imaging of single cells using a high-throughput cyclic immunofluorescence method.' In: *Nature communications* 6 (Sept. 2015), p. 8390. ISSN: 2041-1723. DOI: 10.1038/ncomms9390.

Linde, Sebastian van de, Steve Wolter et al. 'The effect of photoswitching kinetics and labeling densities on super-resolution fluorescence imaging.' In: *Journal of biotechnology* 149.4 (Sept. 2010), pp. 260–6. ISSN: 1873-4863. DOI: 10.1016/j.jbiotec.2010.02.010.

Linde, Sebastian, Anna Löschberger et al. 'Direct stochastic optical reconstruction microscopy with standard fluorescent probes.' In: *Nature protocols* 6.7 (July 2011), pp. 991–1009. ISSN: 1750-2799. DOI: 10.1038/nprot.2011.336.

Linde, S et al. 'Photoswitching microscopy with standard fluorophores'. In: *Applied Physics B: Lasers and Optics* 93.4 (Oct. 2008), pp. 725–731. ISSN: 0946-2171. DOI: 10.1007/s00340-008-3250-9.

Liu, Sheng et al. 'sCMOS noise-correction algorithm for microscopy images'. In: *Nature Methods* 14.8 (2017), pp. 760–761. ISSN: 1548-7091. DOI: 10.1038/nmeth.4379.

Long, Fan, Shaoqun Zeng and Zhen-Li Huang. 'Localization-based super-resolution microscopy with an sCMOS camera Part II: Experimental methodo-

logy for comparing sCMOS with EMCCD cameras'. In: *Optics Express* 20.16 (July 2012), p. 17741. ISSN: 1094-4087. DOI: 10.1364/OE.20.017741.

Micheva, Kristina D and Stephen J Smith. 'Array tomography: a new tool for imaging the molecular architecture and ultrastructure of neural circuits.' In: *Neuron* 55.1 (July 2007), pp. 25–36. ISSN: 0896-6273. DOI: 10.1016/j.neuron.2007.06.014.

Moomaw, Butch. 'Camera technologies for low light imaging: overview and relative advantages.' In: *Methods in cell biology* 114.06 (Jan. 2013), pp. 243–83. ISSN: 0091-679X. DOI: 10.1016/B978-0-12-407761-4.00011-7.

Munck, Sebastian et al. 'Sub-diffraction imaging on standard microscopes through photobleaching microscopy with non-linear processing.' In: *Journal of cell science* 125.Pt 9 (May 2012), pp. 2257–66. ISSN: 1477-9137. DOI: 10.1242/jcs.098939.

Murray, Evan et al. 'Simple, Scalable Proteomic Imaging for High-Dimensional Profiling of Intact Systems'. In: *Cell* 163.6 (2015), pp. 1500–1514. ISSN: 10974172. DOI: 10.1016/j.cell.2015.11.025.

Nakane, P K. 'Simultaneous localization of multiple tissue antigens using the peroxidase-labeled antibody method: a study on pituitary glands of the rat.' In: *The journal of histochemistry and cytochemistry : official journal of the Histochemistry Society* 16.9 (1968), pp. 557–560. ISSN: 0022-1554. DOI: 10.1177/16.9.557.

Pawley, James B., ed. *Handbook Of Biological Confocal Microscopy*. 3rd. Boston, MA: Springer US, 2006, p. 988. ISBN: 978-0-387-25921-5. DOI: 10.1007/978-0-387-45524-2.

Photometrics. *Photometrics Evolve 512 Delta EMCCD Camera for Super-Resolution Research*. 2017. URL: https://www.photometrics.com/products/emccdcams/evolvedelta.php (visited on 12/06/2017).

Pirici, Daniel et al. 'Antibody elution method for multiple immunohistochemistry on primary antibodies raised in the same species and of the same subtype.' In: *The journal of histochemistry and cytochemistry : official journal of the*

Histochemistry Society 57.6 (2009), pp. 567–575. ISSN: 0022-1554. DOI: 10.1369/jhc.2009.953240.

Polacheck, William J et al. 'Microfluidic platforms for mechanobiology.' In: *Lab on a chip* 13.12 (2013), pp. 2252–67. ISSN: 1473-0189. DOI: 10.1039/c3lc41393d. arXiv: NIHMS150003.

Reece, Amy et al. 'Microfluidic techniques for high throughput single cell analysis.' In: *Current opinion in biotechnology* 40 (2016), pp. 90–96. ISSN: 1879-0429. DOI: 10.1016/j.copbio.2016.02.015.

Rino, José et al. 'Frontiers in fluorescence microscopy.' In: *The International journal of developmental biology* 53.8-10 (Jan. 2009), pp. 1569–79. ISSN: 1696-3547. DOI: 10.1387/ijdb.072351jr.

Rittweger, Eva et al. 'STED microscopy reveals crystal colour centres with nanometric resolution'. In: *Nature Photonics* 3.3 (Feb. 2009), pp. 144–147. ISSN: 1749-4885. DOI: 10.1038/nphoton.2009.2.

Robbins, Mark Stanford and Benjamin James Hadwen. 'The noise performance of electron multiplying charge-coupled devices'. In: *IEEE Transactions on Electron Devices* 50.5 (2003), pp. 1227–1232. ISSN: 00189383. DOI: 10.1109/TED.2003.813462.

Robinson, Philip J J et al. 'EM measurements define the dimensions of the "30-nm" chromatin fiber: evidence for a compact, interdigitated structure.' In: *Proceedings of the National Academy of Sciences of the United States of America* 103.17 (Apr. 2006), pp. 6506–11. ISSN: 0027-8424. DOI: 10.1073/pnas.0601212103.

Rust, Michael J, Mark Bates and Xiaowei Zhuang. 'Sub-diffraction-limit imaging by stochastic optical reconstruction microscopy (STORM).' In: *Nature methods* 3.10 (Oct. 2006), pp. 793–5. ISSN: 1548-7091. DOI: 10.1038/nmeth929.

Sackmann, Eric K, Anna L Fulton and David J Beebe. 'The present and future role of microfluidics in biomedical research.' In: *Nature* 507.7491 (2014), pp. 181–9. ISSN: 1476-4687. DOI: 10.1038/nature13118.

Saurabh, Saumya, Suvrajit Maji and Marcel P Bruchez. 'Evaluation of sCMOS cameras for detection and localization of single Cy5 molecules.' In: *Optics express* 20.7 (Mar. 2012), pp. 7338–49. ISSN: 1094-4087.

Schaefer, L H et al. 'Structured illumination microscopy: artefact analysis and reduction utilizing a parameter optimization approach.' In: *Journal of microscopy* 216.Pt 2 (2004), pp. 165–74. DOI: 10.1111/j.0022-2720.2004.01411.x.

Schermelleh, Lothar, Rainer Heintzmann and Heinrich Leonhardt. 'A guide to super-resolution fluorescence microscopy.' In: *The Journal of cell biology* 190.2 (July 2010), pp. 165–75. ISSN: 1540-8140. DOI: 10.1083/jcb.201002018.

Schubert, Walter et al. 'Analyzing proteome topology and function by automated multidimensional fluorescence microscopy.' In: *Nature biotechnology* 24.10 (Oct. 2006), pp. 1270–8. ISSN: 1087-0156. DOI: 10.1038/nbt1250.

Soares, Helena et al. 'Regulated vesicle fusion generates signaling nanoterritories that control T cell activation at the immunological synapse.' In: *The Journal of experimental medicine* 210.11 (Oct. 2013), pp. 2415–33. ISSN: 1540-9538. DOI: 10.1084/jem.20130150.

Szymborska, Anna et al. 'Nuclear pore scaffold structure analyzed by super-resolution microscopy and particle averaging.' In: *Science (New York, N.Y.)* 341.6146 (Aug. 2013), pp. 655–8. ISSN: 1095-9203. DOI: 10.1126/science.1240672.

Tam, Johnny et al. 'Cross-Talk-Free Multi-Color STORM Imaging Using a Single Fluorophore.' In: *PloS one* 9.7 (Jan. 2014), e101772. ISSN: 1932-6203. DOI: 10.1371/journal.pone.0101772.

Testa, Ilaria et al. 'Multicolor Fluorescence Nanoscopy in Fixed and Living Cells by Exciting Conventional Fluorophores with a Single Wavelength'. In: *Biophysical Journal* 99.8 (Oct. 2010), pp. 2686–2694. ISSN: 00063495. DOI: 10.1016/j.bpj.2010.08.012.

Thompson, Russell E, Daniel R Larson and Watt W Webb. 'Precise nanometer localization analysis for individual fluorescent probes.' In: *Biophysical journal* 82.5 (May 2002), pp. 2775–83. ISSN: 0006-3495. DOI: 10.1016/S0006-3495(02)75618-X.

Tramu, G., a. Pillez and J. Leonardelli. 'An efficient method of antibody elution for the successive or simultaneous localization of two antigens by immunocytochemistry.' In: *Journal of Histochemistry & Cytochemistry* 26.4 (Apr. 1978), pp. 322–324. ISSN: 0022-1554. DOI: 10.1177/26.4.207771.

Valley, Christopher C. et al. 'Sequential superresolution imaging of multiple targets using a single fluorophore.' In: *PloS one* 10.4 (2015), e0123941. ISSN: 1932-6203. DOI: 10.1371/journal.pone.0123941.

Vandesande, F and K Dierickx. 'Identification of the vasopressin producing and of the oxytocin producing neurons in the hypothalamic magnocellular neurosecretroy system of the rat.' In: *Cell and tissue research* 164.2 (1975), pp. 153–162. ISSN: 0302-766X. DOI: 10.1007/BF00218970.

— 'Immunocytochemical demonstration of separate vasotocinergic and mesotocinergic neurons in the amphibian hypothalamic magnocellular neurosecretory system.' In: *Cell and tissue research* 175.3 (1976), pp. 289–296. ISSN: 0302-766X. DOI: 10.1007/BF00218707.

Wade, Richard H. 'On and around microtubules: an overview.' In: *Molecular biotechnology* 43.2 (Aug. 2009), pp. 177–91. ISSN: 1073-6085. DOI: 10.1007/s12033-009-9193-5.

Wählby, Carolina et al. 'Sequential immunofluorescence staining and image analysis for detection of large numbers of antigens in individual cell nuclei.' In: *Cytometry* 47.1 (Jan. 2002), pp. 32–41. ISSN: 0196-4763. DOI: 10.1002/cyto.10026.

Winterflood, Christian M. et al. 'Dual-Color 3D Superresolution Microscopy by Combined Spectral-Demixing and Biplane Imaging'. In: *Biophysical Journal* 109.1 (2015), pp. 3–6. ISSN: 00063495. DOI: 10.1016/j.bpj.2015.05.026.

Yi, Jason et al. ‘madSTORM: a Super-Resolution Technique for Large-Scale Multiplexing at Single Molecule Accuracy.’ In: *Molecular biology of the cell* 27 (2016). ISSN: 1939-4586. DOI: 10.1091/mbc.E16-05-0330.

Chapter 2

High-Throughput Single Molecule Super-Resolution Microscope

2.1 Introduction

System development was focused towards dSTORM imaging for two reasons: First, the only two requirements for dSTORM imaging are sufficient illumination intensity (the optical power per unit area) and sufficiently sensitive sensors; and secondly, dSTORM has the potential to achieve the highest resolution possible. However, large FOV dSTORM imaging becomes complicated by the need to ensure sufficient illumination intensity throughout the FOV to induce blinking.

2.1.1 Illumination Intensity

A fluorophore's ON time will decrease proportionally with the laser illumination intensity (Linde et al., 2011). For fast frame-rate cameras, the ON time should match the camera exposure time. Given that there are large variations on the formulation of dSTORM buffers, many prior studies on the impact of blinking characteristics of fluorophores in dSTORM imaging have largely been qualitative. Linde et al. (2011) made a comprehensive list of references comparing dyes, buffers and imaging conditions and the majority of cited studies have imaged dyes at a illumination intensity of $\approx 1\,\mathrm{kW\,cm^{-2}}$ to $2\,\mathrm{kW\,cm^{-2}}$. One of the first published fast EM-CCD dSTORM imaging results with Alexa Fluor 647, Wolter et al. (2010) used from $\approx 35\,\mathrm{kW\,cm^{-2}}$ to $50\,\mathrm{kW\,cm^{-2}}$ to image at 1000 FPS. It should be noted

that this is 10-50 fold greater than the intensities generally used for dSTORM and 10^6 to 10^9 fold greater than conventional imaging (Gustafsson et al., 2016). In another dSTORM experiment imaging Alexa Fluor 647, this time with a fast sCMOS camera rather than an EMCCD, F. Huang et al. (2013) used $\approx$18 kW cm^{-2} to image at 1600 FPS. More recently, Lin et al. (2015) have undertaken a methodical comparison of the impact of different camera speeds and illumination densities on the resolution of dSTORM imaging of Alexa Fluor 647. They compared camera speeds ranging from 50 to 1600 FPS and illumination densities ranging from $\approx$1 kW cm^{-2} to 97 kW cm^{-2} on a FOV of $6.4x6.4\mu m^2$. They observed that increasing the imaging speed had only a negligible impact on the resolution obtained as long as it was accompanied by a proportional increase in illumination density. This demonstrates that there is an ideal illumination density for each camera speed. However, when imaging at 1600 FPS, there was no illumination intensity high enough to replicate the resolutions achievable at slower imaging rates, indicating there is an upper limit to how fast imaging can be performed (Lin et al., 2015). This limit is most likely the life-time of the excited state of a fluorescent molecule, given that this will reduce the number of photons that can be emitted in a given period of time.

While imaging at such high speeds will reduce the overall acquisition time, for high-throughput imaging with sCMOS cameras, there is another factor to consider: the large FOV can also increase the overall throughput. As has been argued (Almada et al., 2015), if a coverslip is uniformly covered with cells, the parallel acquisition of different cells offsets any benefit from acquiring a single FOV very fast. For a high-throughput SMLM system with an sCMOS camera it becomes apparent that the laser illumination intensity should ideally match the full FOV acquisition rate.

2.1.2 Large FOV Homogeneity

Aside from illumination density, the homogeneity of the FOV also needs to be considered. As mentioned in section 1.3, traditional laser illumination schemes have a non-uniform illumination pattern that results in the centre of the FOV being brighter than its edges. This is because the intensity distribution profile of a laser beam and the single-mode optical fibres typically used in laser illumination sys-

tems approximates a Gaussian distribution (Pawley, 2006). To correct for this, there are several options to achieve a uniform illumination throughout the FOV (Almada et al., 2015). For fast (>50 FPS) dSTORM imaging, optical efficiency needs to be maximised to achieve the highest possible resolution (F. Huang et al., 2013; Linde et al., 2011). One cost effective option for delivery of homogeneous illumination with minimal power loss is a vibrated multi-mode fibre system. The homogenisation results from the fact that the output of a multi-mode fibre is a semi-random pattern that is mechanically sensitive and if the fibre is agitated in any way, the output pattern is altered. By vibrating the fibre at a frequency that is significantly higher than the acquisition exposure time, all of the different resulting patterns blur together into a homogenous pattern (Inoué et al., 1997; Fujimaki et al., 2014; Zhao et al., 2017). Multi-mode fibres have large illumination transmission efficiency (~90%) and are significantly easier to align when compared to single-mode fibres. Fibre based illumination systems also have the potential to be more stable as any alignment drift of parts of the laser launch should result in a reduction of illumination intensity and not misalignment of the illumination itself. For the above reasons, the illumination system was designed around a vibrated multi-mode fibre.

2.1.3 Total Internal Reflection Fluorescence Microscopy

One important consideration for dSTORM imaging is the choice of whether or not to implement Total Internal Reflection Fluorescence (TIRF) illumination. TIRF illumination allows for high SNR imaging of structures near the coverslip. As the resolution achievable in SMLM is dependent upon the SNR, using TIRF is highly beneficial for SMLM systems (Thompson et al., 2002). Most modern TIRF microscopes are based on focusing laser light on the microscope objective's Back Focal Plane (BFP) (Mattheyses et al., 2010). Any translation of the focal spot on the BFP will result in a change of the angle of the beam exiting through the front of the objective (figure 2.1). When focusing a beam on the centre of the BFP, the beam will be going straight through the sample, at 90°to the coverslip surface (figure 2.1 A,B). As the beam is translated towards the edge of the BFP, the angle at which the beam exits from the objective will change (figure 2.1C and D). If the beam reaches an

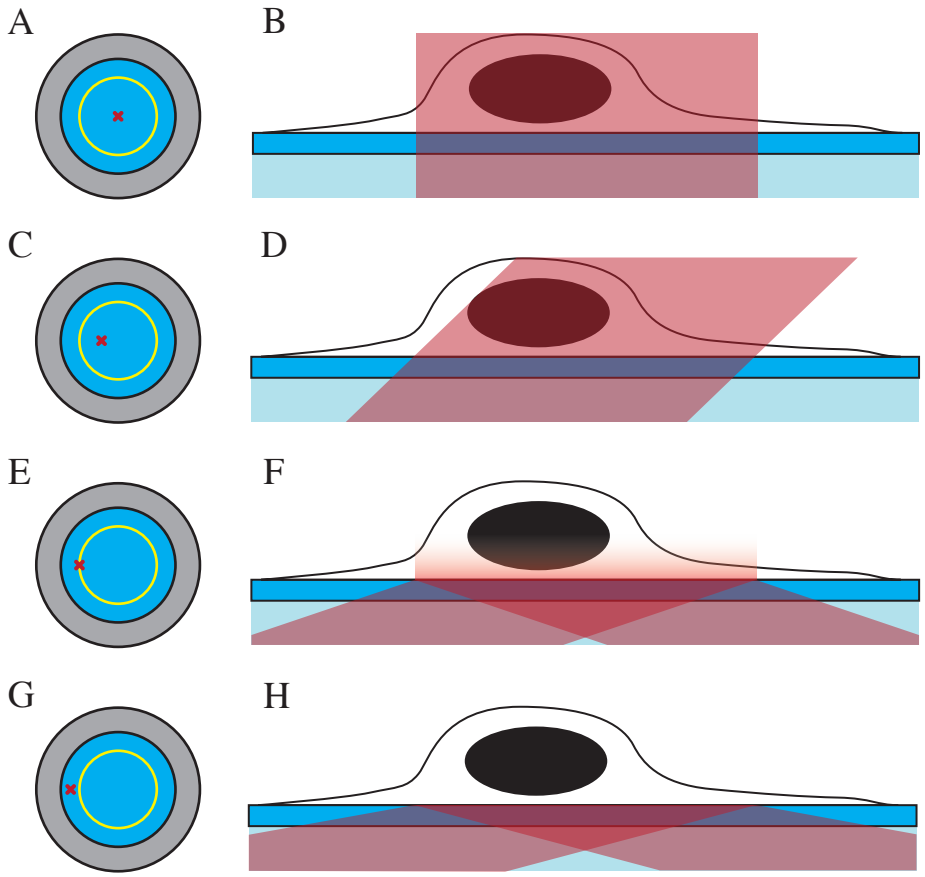

Figure 2.1: Focusing a laser spot in different regions of the BFP results in different angles of incidence of the laser beam out of the objective. A, C, E and G show illustrations of the BFP and the critical region is denoted by a yellow ring. The red cross shows where the laser is focused and the resulting illumination is shown in B, D, F and H respectively. Light blue elements correspond to the immersion oil, dark blue corresponds to any glass element and the laser beam is shown in red.

interface between two media of different refractive index (i.e. the interface between the coverslip glass and the water of the cell media) at a critical angle or lower, it will get reflected (figure 2.1 G,H). However, when light hits the interface at precisely the critical angle, an evanescent field is generated that illuminates only a small depth of the sample ($< 100nm$; figure 2.1 E,F). Thus, to achieve TIRF one needs to be able to translate a laser beam along the BFP of the objective. The size of the region on the BFP where critical angle illumination is achieved will be a function of the Numerical Aperture (NA), the Refractive Index (RI) of the objective immersion and the RI of the sample's media. For these reasons, TIRF is generally achieved with very high NA (>1.4) oil objectives imaging samples immersed in water. Since most

dSTORM buffers are water based, TIRF is compatible with SMLM. A vibrated multi-mode fibre system is also compatible with TIRF depending on the size of the focused spot on the BFP (Pawley, 2006).

2.1.4 Dual Camera Imaging

If an underlying principle of accelerating SMLM is to parallelise acquisition, then doubling the number of cameras used for imaging is inherently beneficial. Dual-camera imaging can enhance an SMLM experiment in two ways. First, the light can be split to each camera according to wavelength by using a dichroic mirror. This would enable simultaneous dual-colour imaging which would double the throughput for a two-colour experiment. Secondly, Juette et al. (2008) demonstrate the biplane method, where two cameras can be used to determine the axial position of the fluorophore with super-resolution accuracy. In the biplane method, light is split 50/50 between each camera, but each is slightly defocused on opposite directions. The Point Spread Function (PSF) (the description of how light from a single point is captured by an optical system) will change shape as it is slightly defocused, and by fitting the shape observed in both cameras to the PSF, the axial position of the fluorophore can be determined precisely. More recently, Winterflood et al. (2015) combined dual-colour imaging with biplane imaging by both using a dichroic mirror to split the light by emission wavelength while simultaneously defocusing each camera. In this way, dual camera imaging can simultaneously provide 3D super-resolution information while still doubling the throughput.

There are two main methods to split the light between two cameras without affecting image quality. The simplest method is to split the light in the so-called infinity path. Most modern objectives for fluorescence microscopy use infinity optics (Cox, 2010). The light rays coming from the back of the objective are in fact parallel to each other as if they were focused to infinity. These objectives need a paired tube lens that will focus this light into a magnified image. The distance between the BFP and the tube lens is called the infinity space, or infinity path. The primary advantage of using infinity-corrected optics is that placing dichroic mirrors, either to inject illumination light or to split the emission light will not introduce any chro-

matic aberrations resulting from having a tilted piece of glass on the light path. The length of the infinity space, L_∞, should be kept less than the length obtained from equation (2.1) or the FOV will be reduced (Applied Scientific Instrumentation, n.d.).

$$L_\infty \leq (D_t - D_o) * \frac{F_t}{D_s} \tag{2.1}$$

Where, D_t is the diameter of the tube lens, D_o is the diameter of the objective pupil, F_t is the focal length of the tube lens and D_s the diagonal length of the sensor. Depending on the choice of objective, tube lens and camera sensor, L_∞ may not be sufficiently large to place many optical elements such as dichroic mirrors. If more optical elements are required than L_∞ allows, an optical relay can be used. An optical relay uses two lenses to relay the image plane that is made after the tube lens to another location. In between these two lenses a second L_∞ is created which allows for more optical elements to be placed in the emission path (figure 2.11). Optical relays are also called 4F systems given that it will have a path length of 4 focal lengths, 2 for each lens. This method has been used in the original biplane imaging paper (Juette et al., 2008), as well as in Winterflood et al. (2015) to assemble a SMLM microscope that splits the emission light for both multicolour and biplane imaging.

2.1.5 Drift Correction

A SMLM acquisition requires tens of thousands of frames to be acquired for a satisfactory reconstruction. It is paramount that the sample remains static for the duration of the acquisition. However, most samples will drift in some form during acquisition and this drift can occur in both the axial and lateral dimensions. Axial drift is the most destructive since, if the sample goes out of focus, it will simply no longer be imaged. However, lateral drift can be corrected for *a posteriori* if the sample remains in focus, meaning it will not prevent image acquisition like axial drift. Given this, most SMLM experiments rely on some method to correct for axial drift, but not lateral drift, during acquisition. Hardware based axial drift correction has largely been accomplished by an active feedback loop created by shinning an

Infra-Red (IR) laser on the sample, measuring any shifts in the reflected signal and adjusting the stage position (Winterflood et al., 2015; Linde et al., 2011; B. Huang et al., 2008). All major microscope manufacturers sell these systems as microscope additions (Applied Scientific Instrumentation, 2017a; Nikon, 2017b; Leica, 2015; Zeiss, 2017; Olympus, 2017).

To correct for lateral drift, either fiducial markers (such as fluorescent beads) (Rust et al., 2006) or cross-correlation can be used to correct for drift *a posteriori* (Wang et al., 2014; Mlodzianoski et al., 2011; Bates et al., 2007).

Fiducial markers for SMLM are non-blinking reference markers whose position can be tracked through the acquired image stack, providing a direct measurement of lateral drift. This measured drift can then be subtracted from the localisations table, thereby correcting for lateral drift. Fiducial marker correction provides the most direct measurement of drift but requires at least one fiducial to be present in the FOV through the entire acquisition which is not always guaranteed. Increasing the number of fiducial markers can ensure sufficient markers are present but their brightness can also obscure the object of interest.

Cross-correlation, or the dot-product function, does not require any markers to be present however. It is a function used to measure similarity between two signals. For two dimensional signals, or images, the normalised cross-correlation is defined as (Lewis, 1995)

$$\mathrm{CCM}(\Delta x, \Delta y) = \frac{\sum_{x,y}(f(x,y) - \overline{f}_{x,y})(g(x-\Delta x, y-\Delta y) - \overline{g}_{x,y})}{\sqrt{\sum_{x,y}(f(x,y) - \overline{f}_{x,y})^2 \sum_{x,y}(g(x-\Delta x, y-\Delta y) - \overline{g}_{x,y})^2}} \tag{2.2}$$

Where $f(x,y)$ and $g(x,y)$ are the two images being correlated, $\overline{f}_{x,y}$ and $\overline{g}_{x,y}$ are their respective mean values and Δx and Δy correspond to a pixel-wise translation of the image. The final result is a 2D map, the Cross Correlation Map (CCM), that corresponds to the cross-correlation signal (see figure 2.16 for examples). The value of the normalised cross correlation reflects the degree of similarity between the two images, where a value of 1 indicates that the images are perfectly identical. The position of the highest value in the cross correlation map can as such be used to infer

which shift of Δx and Δy (i.e which drift compensation shift) resulted in maximal similarity between the two images. If one image is shifted laterally in relation to the other, the peak will be shifted laterally in the map by the same amount. So, if the sample has drifted by one pixel in either direction, the peak will shift by one pixel in that direction. Lateral drift correction in SMLM is achieved by cross-correlating each frame to the next to estimate the overall lateral drift (Wang et al., 2014). By tracking the lateral displacement of the peak in the resulting CCM stack, the total lateral drift can be estimated and the localisations corrected. The sparse nature of these images can make it hard to correlate one frame to the next, so the stack can be binned into chunks (i.e. projections of 1000 frames) to improve the correlation (Mlodzianoski et al., 2011). However, when comparing with tracking fiducial markers, precision can still suffer when there is dissimilarity between chunks.

The cross-correlation map can also give an estimate of the axial drift. The lower the intensity of the peak, the lower the similarity between two images. If a sample is going out of focus, this will result in lower cross correlation. This has been exploited by McGorty et al. (2013) to perform drift correction during acquisition of all three dimensions (3D). They use a separate IR illumination and camera path to measure the cross-correlation of the sample over time versus a static reference (figure 2.2). The static reference is an image stack acquired by taking an image of the sample when it is in focus and when it is moved by 750 nm above and below the focus. During the SMLM acquisition, new IR images are acquired simultaneously and compared with the three reference images. Cross-correlation with the in focus image will yield the lateral drift. If the sample has moved up, the above focus reference will generate a higher cross-correlation signal than the bottom reference and vice-versa. By calibrating with the known axial displacement of the reference images, the axial drift can be determined accurately. This algorithm, here termed as Cross Correlation by Static Reference (CCSR) drift correction, is particularly useful for high-throughput SMLM as it removes the need to add fiducial markers during sample preparation as well as the need to correct for lateral drift *a posteriori*.

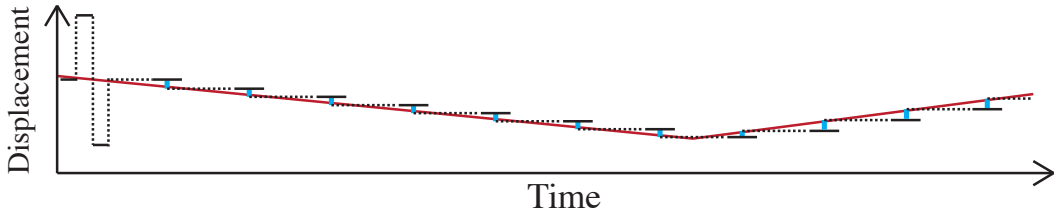

Figure 2.2: Diagram of the Cross-Correlation Drift correction by Static Reference algorithm. A stack of 3 images is acquired at the beginning of the procedure to be used as a reference. At regular time intervals a frame is acquired and the drift is estimated by cross-correlating the new frame with the three images on the reference stack. The stage is then offset by the amount of estimated drift. Solid lines - frame acquired; Dashed lines - stage position; Blue lines - measured drift; Red line - actual drift present in the microscope.

2.1.6 Chapter Scope

The above mentioned features correspond to the major desirable characteristics of a high-throughput SMLM system: large-FOV imaging with homogeneous illumination; high illumination intensity for high-speed imaging; dual camera acquisition; TIRF illumination; and 3D real time drift-stabilisation. The remainder of this chapter will describe the design and implementation of a system implementing all of the above features along with early imaging results. The microscope system will be referred to here as the Alpha.

2.2 Results

2.2.1 Microscope Design

2.2.1.1 Microscope Parts and Assembly

The microscope stand of the Alpha needs to be able to accommodate a high-intensity TIRF illuminator and a dual camera emission path. Applied Scientific Instrumentation (ASI) manufacture a highly modular system geared towards custom solutions. This frame was chosen since the modularity imposed less restrictions on the optical path when compared to other commercial microscope frames. The modularity also allows for more cameras to be added in the future. This microscope system is based on the Modular Infinity Microscope (MIM) (Applied Scientific Instrumentation, 2017b). It consists of a bare-bone set of parts that include objective threads, objective translator for focusing, cube-mounts for dichroic mirrors and tube lenses. MIM microscopes can be assembled in ASI Rapid Automated Modular Microscope (RAMM) (Applied Scientific Instrumentation, 2017c) stands. These consist of a simple microscope frame where automated or manual stages can be mounted as well as a MIM create a fully functioning microscope system. ASI also provide a hardware axial drift correction option (Applied Scientific Instrumentation, 2017a) that is easily adapted to MIM systems.

The MIM system was configured and assembled as shown in figure 2.3. The objective is mounted on a motorised linear stage (ASI, LS-150) which allows the objective's focus to be adjusted in relation to the sample mount on the RAMM (not shown in figure 2.3). Fixed to the stage (not translated with the objective) are two dichroic cube holders: immediately below the objective is an 800nm long pass dichroic for the drift correction system and below it is a quad dichroic to allow the TIRF illuminator to focus on the BFP of the objective. The fluorescence emission passes through both dichroics and will exit through the bottom of the TIRF illumination dichroic cube. A thread was machined on the bottom of this cube to allow an achromatic Nikon 200mm tube lens (Thorlabs, ITL200) to be threaded in. A 2 inch elliptical mirror, mounted at 45° on the optical table, takes the fluorescence

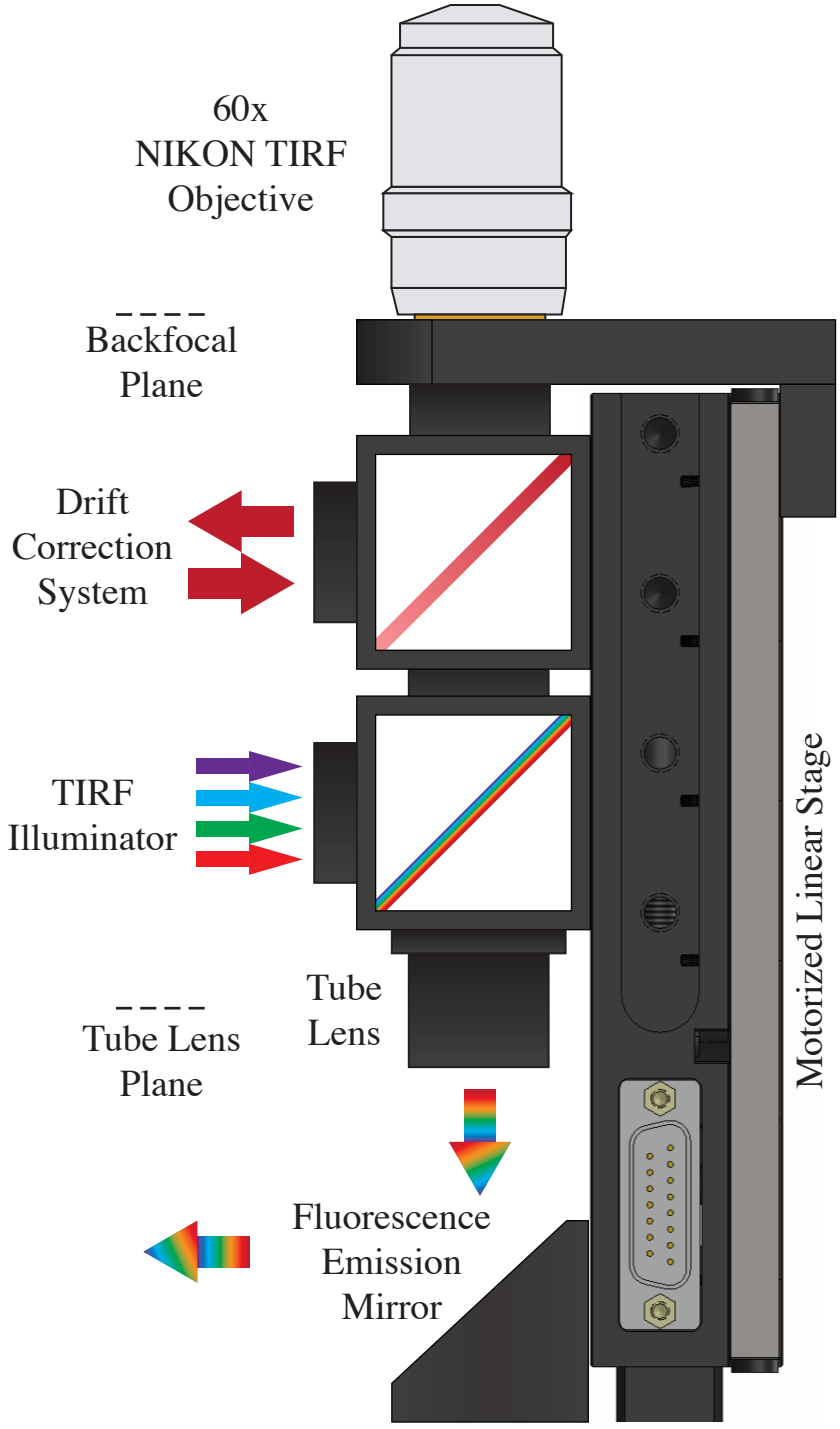

Figure 2.3: Illustrative diagram of the Modular Infinity Microscope. Shown are the motorised stage on the right-hand side which translates the objective for focusing. The two cubes correspond to the dichroic for the drift correction system (above) and for TIRF illumination (below). The infinity space corresponds to the length between the lens's back focal plane and the plane of the tube lens. The microscope is positioned vertically and the emission light is reflected at 45°to make it parallel to the table plane by a 2" elliptical mirror (below).

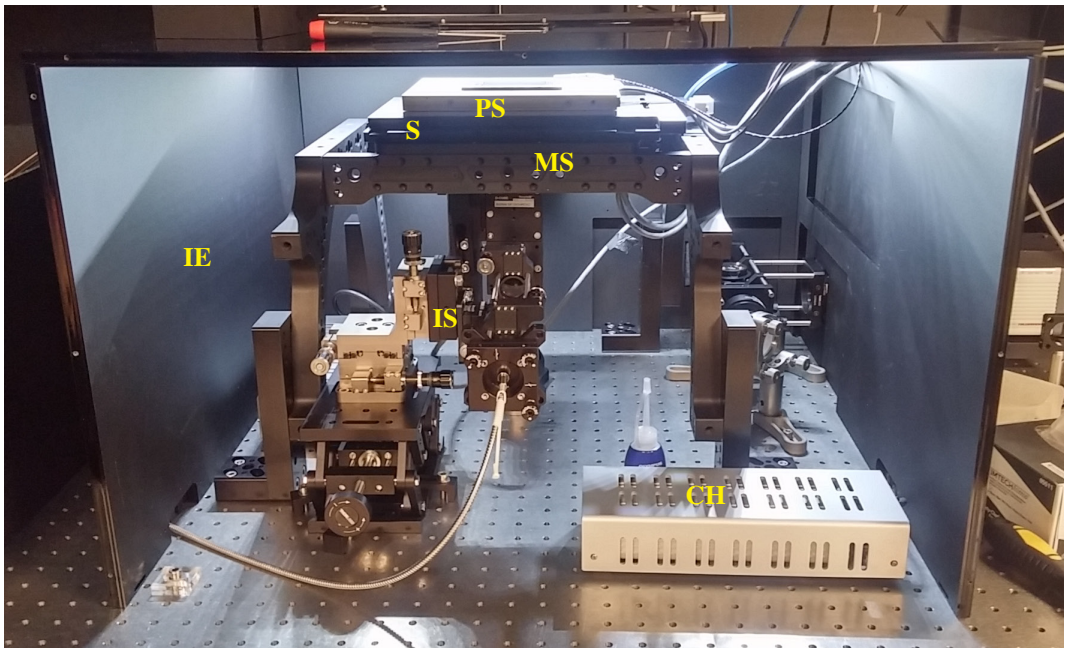

Figure 2.4: Photograph of the microscope stand, TIRF illuminator and incubator. The MIM microscope is mounted behind the TIRF illuminator. MS - microscope stand; IE - incubator enclosure; S - XY motorised stage; PS - 3D piezo stage; IS - illumination system described in figure 2.6; CH - ceramic heater.

emission and makes it parallel to the optical table. In this way, the fluorescence emission is steered towards the emission path (see section 2.2.1.4). The entire MIM assembly is mounted in an ASI RAMM stage (figure 2.4). The sample holder is mounted on an automated XY stage (ASI, MS2000) with a secondary small travel range ($300\mu m$) piezo 3D stage (PiezoConcept, BIO-3). The entire microscope is enclosed by an incubation enclosure and ceramic heaters (enclosure and heaters provided by Digital Pixel) which allow for vibration free temperature control for live imaging experiments.

2.2.1.2 High-density TIRF Illuminator

In order to benefit from TIRF imaging, the microscope was designed around a single Nikon Apo TIRF 1.49 60x objective and system illumination was designed with the ability to perform TIRF in mind. Given the dependence of high-speed dSTORM imaging on illumination intensity, the illumination system was designed to maximise this. Four lasers (table 2.1) were installed on an optical table separate from the table where the RAMM and the emission path are mounted. This is to

prevent any vibrations from the lasers cooling fans to be transmitted to the Alpha.

Manufacturer	Model	Wavelength (nm)	Power (mW)
Coherent	OBIS	405	50
Coherent	GENESIS	488	1000
Coherent	GENESIS	561	500
Toptica	iBeam	640	150

Table 2.1: Laser lines presently installed on the microscope.

This optical table contains all the optical elements required to combine the 4 laser lines into one beam, modulate it with an AOTF and couple the beam to an optical fibre (figure 2.5). Each laser was installed on a custom machined aluminium mount which allowed all four laser units to emit light at the same height, facilitating alignment. In front of each laser is a lens system designed to adjust the laser divergence. These consist of a pair of two 30*mm* lenses (Thorlabs, LA1805-A) assembled on a cage system, one of which is mounted on a translating mount. Both lenses are two focal lengths away from each other, which should result in no change to laser beams divergence. But by moving one of the lenses backward or forward, the laser beam can be made to diverge or converge slightly. This allows to adjust for any chromatic aberrations on the lens focusing on the optical fibre, thereby maximising transmission for each laser line. Preceding this lens system there are two mirrors to make the laser beam coaxial with the centre of both lenses. After the collimation adjusters, the lasers are combined by a sequence of dichroic mirrors (Chroma, ZT568rdc, ZT491rdc, ZT442rdc) which are then guided through an AOTF (AA Optoelectronics, AOTFnC-400.650). The AOTF performs intensity modulation and shuttering of all 4 lasers by acoustically modulating a birefringent crystal (Pawley, 2006). Light is normally refracted when going through the AOTF crystal but its direction can be changed by a fixed amount when specific acoustic frequencies are applied to it. When light is meant to illuminate the sample, the lasers are steered into a fibre coupler (Thorlabs, KT110/M). Light that is not being steered into the fibre coupler is directed to a beam dump instead (Thorlabs, LB1/M). Before both the AOTF and the fibre coupler there is a set of two mirrors assembled in adjustable tip/tilt mounts (Thorlabs, POLARIS-K1). This allows the alignment

to be corrected for each element.

The output end of the optical fibre is installed on a TIRF illumination system (figure 2.6A). This consists of a cage system which collimates the beam and then focuses it on the BFP. In order to retain achromatic illumination and thereby preventing different TIRF profiles for each laser line, the TIRF illuminator was designed to be achromatic. The output of the fibre is collimated by a 30*mm* achromatic lens (Thorlabs, ACA254-030-A). The collimated beam is slightly eccentric with regards to the central axis of the cage system. Laser light that is focused by a lens will have less chromatic aberrations when the beams hits the lens on its centre and perpendicularly to the lens's plane (Cox, 2010). Two corner mirrors (figure 2.6 A) are used to adjust and make the beam axially aligned with the cage system. The beam is then focused by a 200*mm* lens (Thorlabs, LA1708-A) onto the BFP. Because the beam is made to enter the 200*mm* lens straight through its centre, the focused spot will have ideal achromaticity for that lens. Additionally, the whole illuminator is mounted on a 3D translation and 2 axis rotation stage (figure 2.6 B). This stage allows the beam's angle and position on the BFP to be adjusted for alignment. It is by moving this stage that TIRF can be achieved, as the focal spot needs only to be translated laterally on the BFP. The stage itself is mounted on a lab-jack to enable fast switching between widefield and TIRF modes. To demonstrate the ability to perform TIRF, HeLa cells were immuno-labelled for Vimentin with Alexa Fluor 647 and imaged in both widefield and TIRF modes (figure 2.7). The TIRF effect can be observed by the significant reduction in background signal in the TIRF image.

2.2.1.3 Large FOV Illumination

There is, however, a loss of laser illumination intensity associated with each optical element. Table 2.2 shows measured illumination intensity losses for some of the major components. As can be observed, the multi mode fibre results in lower laser illumination intensity loss than other components of the illumination system. For comparison, a single mode fibre was also installed and yielded losses ranging from 40% to 80%, depending on the laser line, as is consistent with the literature (Pawley, 2006). The disadvantage of using a multimode fibre as a microscope il-

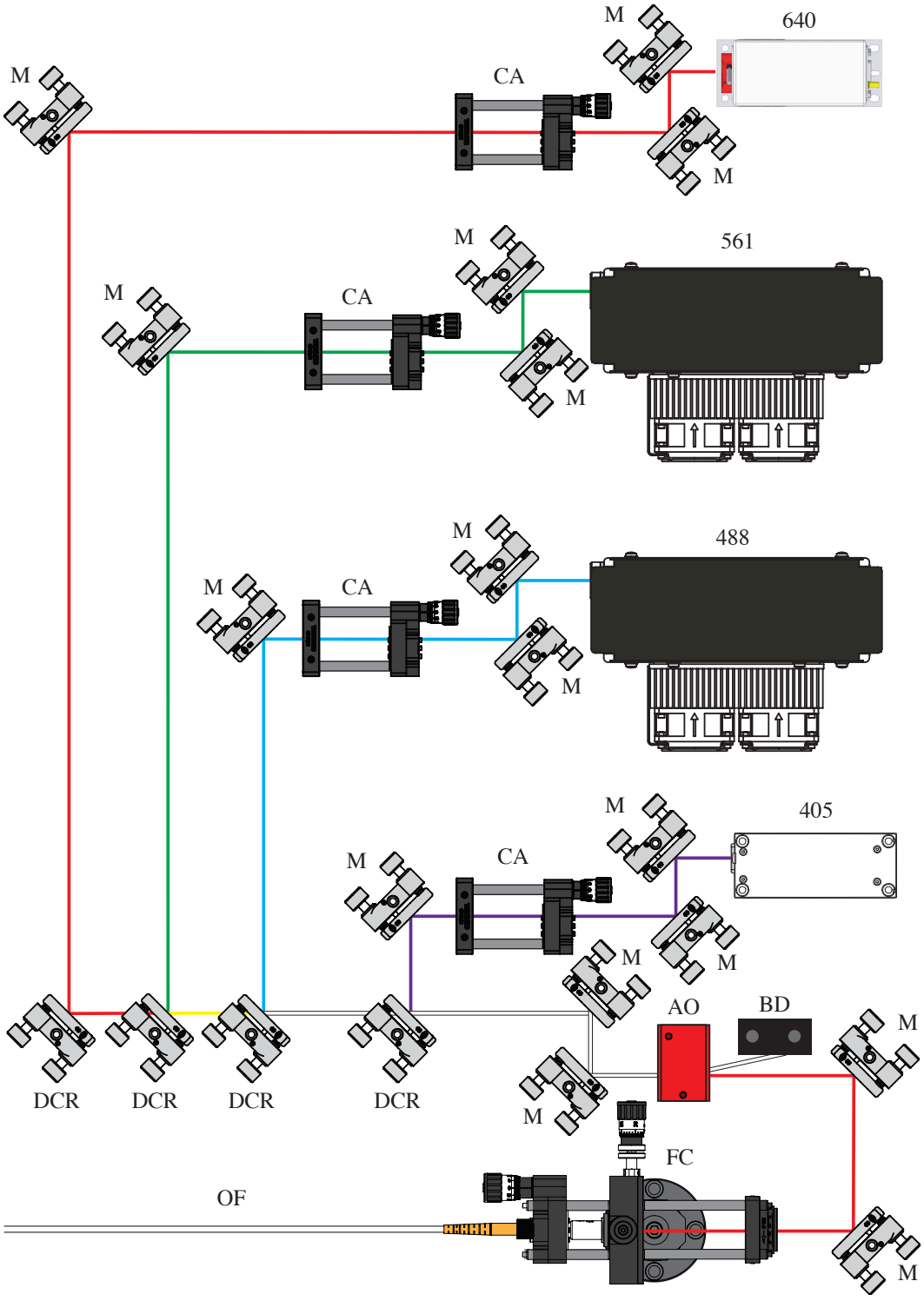

Figure 2.5: Illustrative diagram of the Laser combiner. 405, 488, 561, 640 - lasers identified by their respective emission wavelengths; M - mirror; CA - collimation adjuster; DCR - dichroic mirror; AO - AOTF; BD - beam dump; FC - fibre coupler; OF - optical fibre.

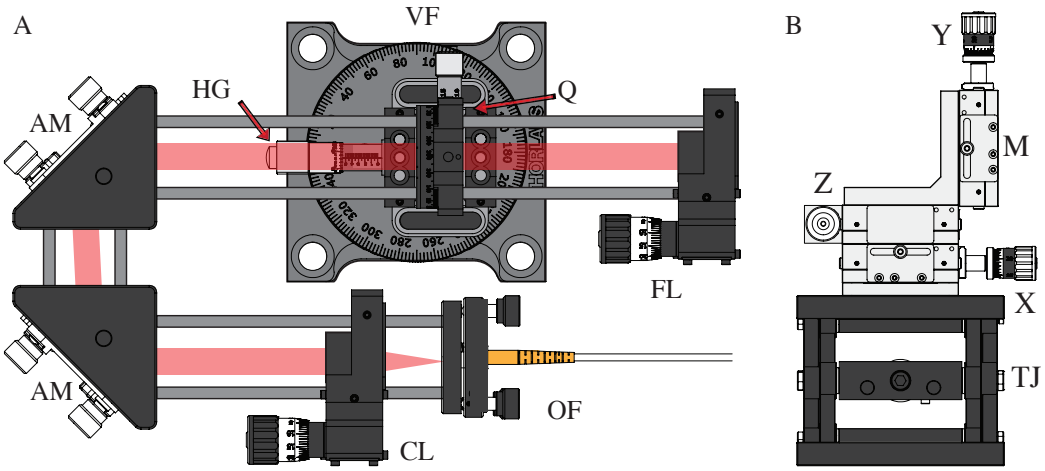

Figure 2.6: Illustrative diagram of the TIRF illuminator. A - TIRF illuminator. The illuminator is designed to focus laser light achromatically at the back focal plane of the TIRF objective (figure 2.3). It consists of a cage system that contains the optics necessary to collimate the laser coming from an optical fibre and adjust so it is centred on the focusing lens. It is mounted on a 3D translator and vertical and horizontal rotation stages. OF - optical fibre; CL - collimating lens; AM - adjustment mirror; Q - quarter wave plate; FL - focusing lens; VR - vertical rotation stage; HG - horizontal goniometer/rotation stage. B - Illustrative diagram of the translation stage for position adjustment of the TIRF illuminator. The stage itself is mounted on a lab jack (TJ) which allows for fast adjustment of the TIRF angle. M - mounting point where VR is mounted; X - X axis adjustment stage; Y - Y axis adjustment stage; Z - Z axis adjustment stage; TJ - TIRF adjustment jack.

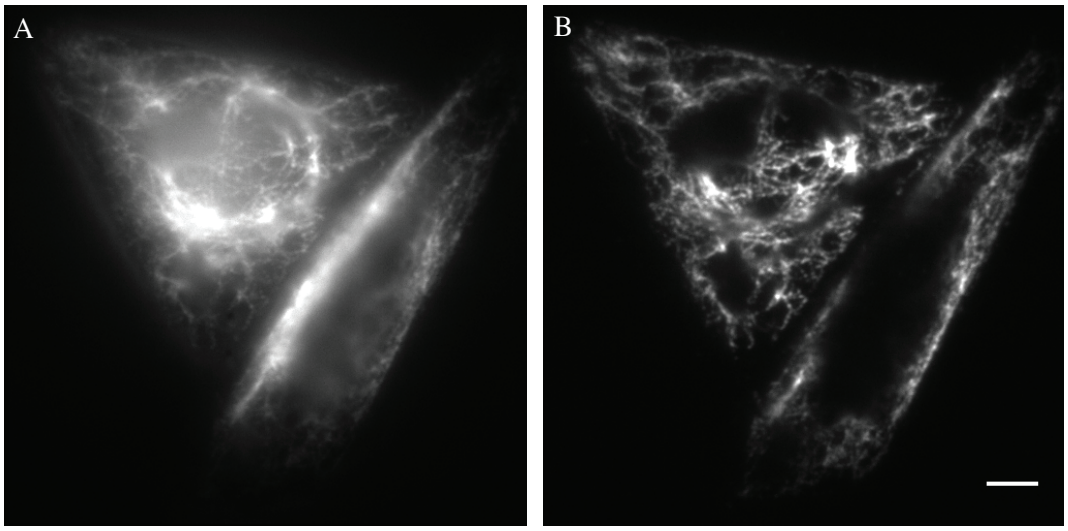

Figure 2.7: Demonstration of TIRF imaging on the Alpha. HeLa cells immuno-labelled for vimentin with Alexa Fluor 647 being imaged in widefield mode (A) and TIRF mode (B). Scale bar - 5μm.

Laser line	Rated power	Dichroic loss	AOTF loss	MM loss	Recovered
640	150	14.57%	16.28%	7.5%	99
561	1000	22.49%	3.28%	4.5%	716
488	500	17.50%	7.58%	5.1%	362
405	50	18.87%	23.26%	18.3%	24.4

Table 2.2: Measurements of laser illumination intensity loss and total recovered illumination intensity for each laser line. Laser light was measured before and after each element to estimate individual illumination intensity loss. Recovered laser illumination intensity was measured at the objective focal plane. Rated and recovered laser illumination intensity given in mW. MM - Multi Mode fibre;

lumination source is that it creates a non-homogenous pattern on the FOV. This pattern is highly sensitive to any mechanical perturbation of the optical fibre. To demonstrate this, HeLa cells were methanol fixed, immuno-labelled for microtubules using Alexa Fluor 647 and imaged. In order to qualitatively demonstrate the mechanical sensitivity of the pattern, a sequence of 500 frames was acquired while agitating the fibre manually. The pattern is largely too subtle to identify on a static frame, even when compared with a maximum projection of all 500 frames (figure 2.8A and B). However, by dividing the pixel values of different frames with the values in the average projection, the underlying difference in the patterning for each frame can be observed (figure 2.8C).

While the patterning may seem negligible on static frames, it becomes immediately apparent in any time-lapse or z-stack acquisitions. It could also be problematic for single-molecule super-resolution imaging as the resolution is dependent in illumination intensity and this pattern could result in images with different resolutions in different parts of the image. The fibre can be vibrated at high frequencies in order to blur the patterns into an homogenous field of view (Inoué et al., 1997; Fujimaki et al., 2014). To achieve this, two sets of four $\approx 283Hz$ vibration motors (Precision MicroDrives, 312-401) were attached to loops of the multi-mode fibre. An Arduino open-source electronic controller (Arduino, 2017) was configured to control the motors. The motors are activated in a staggered sequence (figure 2.9). The Arduino was also configured to act as a micro-manager shutter, making sure the motors are only turned on when an acquisition is ongoing. Both of these features (staggered ac-

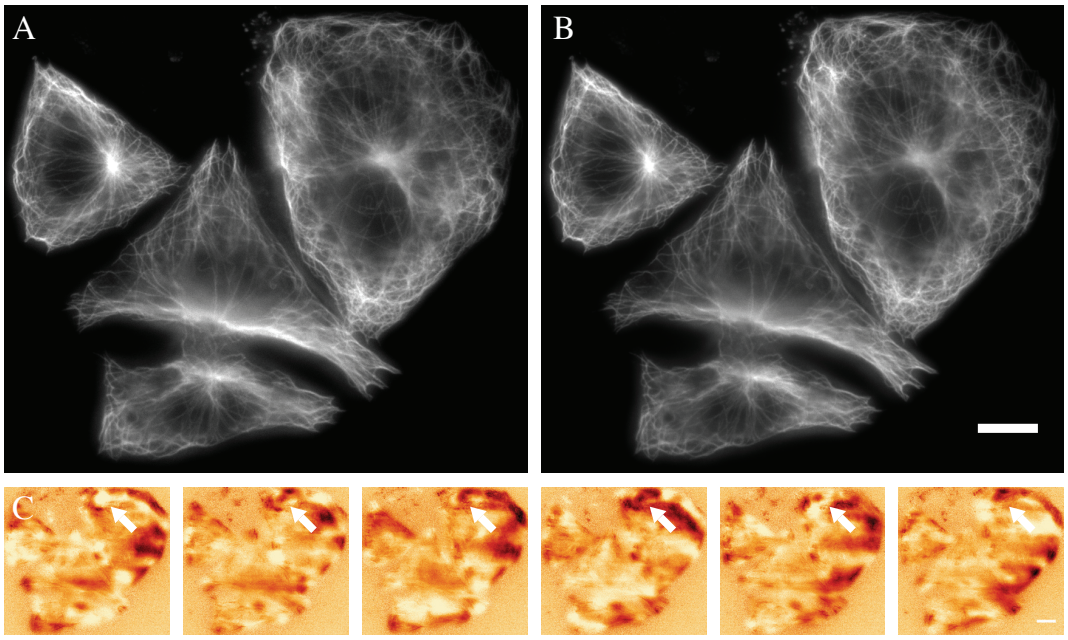

Figure 2.8: Demonstration of the effect of the multi-mode fibre patterning on the illumination. A - single frame; B - average projection of the 500 different frames when agitating the fibre manually; C - sequence of 6 frames whose values were divided against the average projection in B. White arrows show areas where intensity is changing over time. Scale bars - 10μm.

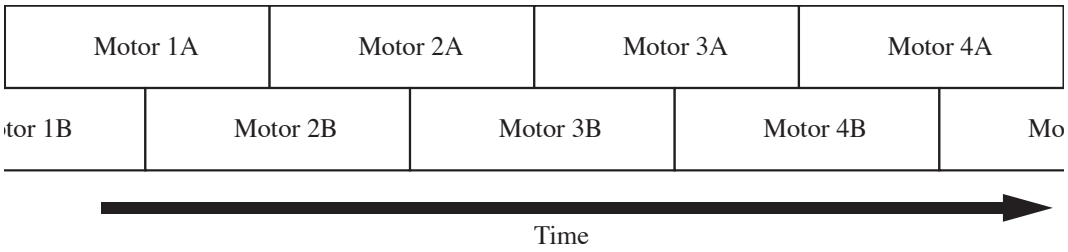

Figure 2.9: Time sequence for the two sets (A and B) of vibration motors. Two motors are turned on at any given time. Halfway through the vibration cycle of one motor set, the other motor set will progress in its sequence.

tivation and Arduino shuttering) ensure that the motors are not turned on for longer than their rated capabilities, thereby preventing damage.

The homogeneity that is achieved is demonstrated in figure 2.10. An homogenous plastic slide (Chroma) was imaged with 10 ms exposure time using either a single mode or a vibrated multi-mode fibre. Figure 2.10A demonstrates the non-homogeneity associated with the single mode fibre when illuminating a 512x512 ($55x55\mu m^2$) FOV. There is an almost 50% drop in illumination intensity from centre to edge, whereas the multi-mode fibre (figure 2.10B) results in a maximum of a 18%

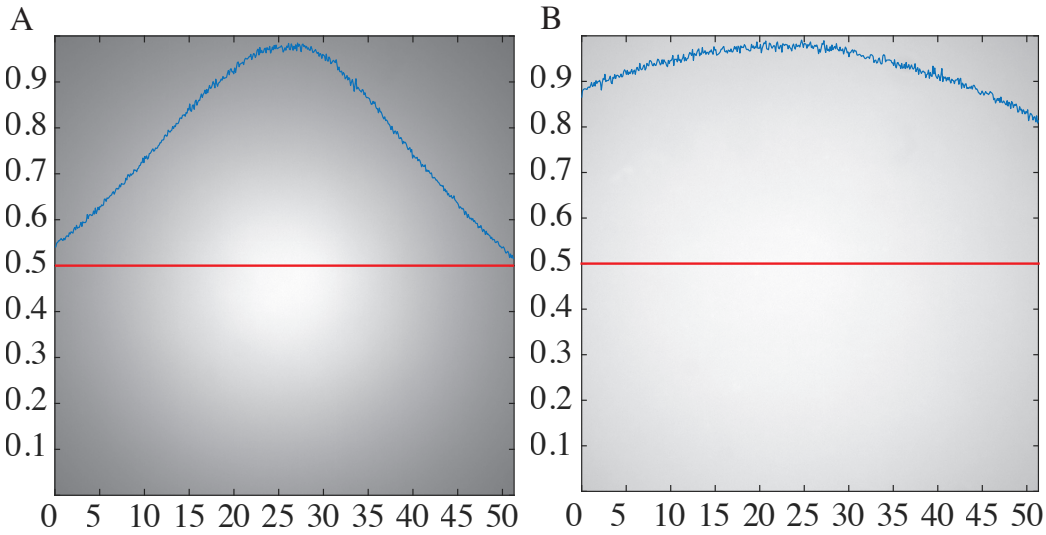

Figure 2.10: Normalised intensity plots for a 512x512 pixel FOV ($55x55\mu m^2$) using a single mode (A) or a vibrated multi-mode (B) fibre. Plots are overlaid over a representative image of the FOV. Red lines - Line along which the intensity values were measured; Y axis corresponds to the normalised intensity values; X axis corresponds to the pixel position in microns.

drop in illumination intensity for the same covered area. Additionally, the patterning is no longer visible.

Having established the homogeneity of the FOV, the question becomes: what is the achievable illumination intensity for high speed SMLM imaging? The cameras used with the Alpha (see next section) have a 2048x2048 pixel sensor which can be cropped to cover smaller areas and the laser illumination can be made to cover circular areas of different size (depending on the focal length of the collimating lens in figure 2.6A). Table 2.3 estimates the 640nm illumination intensity that would be achieved by matching the diameter of the illuminating spot to different square cropped regions of the sensor. It also assumes that only up to 99mW of laser light are available. The 30*mmlens* in use in the TIRF illuminator achieves homogenous illumination at 512x512. According to table 2.3 this is the largest FOV with a illumination intensity sufficient for dSTORM imaging (Lin et al., 2015; Linde et al., 2011). Given this, the FOV illumination for further acquisitions was set at 512x512 with the 30*mmlens*, corresponding to a FOV of $55x55\mu m^2$.

Pixels	2048	1024	512	256	128	64
Illumination Intensity	0.13	0.51	2.05	8.19	32.78	131.11

Table 2.3: Calculation of expected illumination intensity of 640nm laser illumination for different FOV crop factors. Illumination intensity given in $\mathrm{kW\,cm^{-2}}$ and corresponds to 99mW projected into a circle with a diameter which matches the diagonal of the cropped area.

2.2.1.4 Dual-Camera sCMOS Imaging

Because the Hamamatsu Flash4.0 cameras provides the combination of QE, fast frame-rate and large FOV that a high-throughput SMLM system requires, these were chosen for the Alpha. A 4F system was required to allow dual camera imaging since the infinity path was not long enough to accommodate both the ASI CRISP dichroic and the laser illumination dichroic. Figure 2.11 shows the design of the emission path, placed shortly after the laser dichroic (figure 2.3). Before the emission splitting system, there are two 2" dichroic mirrors mounted in tip/tilt mounts, allowing the emission path to be aligned with regards to the 4f system. The lenses for the 4f system as well as the dichroic mirror holder are mounted in a cage system to simplify alignment of the optical path. The light coming from the microscope is then relayed by a tube lens (Thorlabs, ITL200), recreating the infinity path. At a distance of one focal length from this tube lens, a dichroic mirror is held in a tip/tilt platform mount (Thorlabs, B4C/M). The mirror is exchangeable and either a 50/50 beam-splitter (i.e., it transmits and reflects half of the light; Chroma, 21000), a 565nm dichroic mirror (Chroma, T565lpxr) or a 647nm dichroic mirror (Chroma, T647lpxr) can be installed. The 50/50 mirror allows biplane imaging to be achieved; the 565nm and 647nm dichroics reflect shorter wavelengths and transmit longer wavelengths, enabling dual-colour imaging. The mirrors have a thickness of $3mm$ to minimize any distortions introduced in the reflected image resulting from the mirror being gripped in the mount. The tip/tilt also mount allows for any misalignment between the two cameras to be corrected. At two focal lengths from the first tube lens, a second tube lens takes the emission light and focuses it into an image on one of the two cameras. Prior to each of the cameras there is also an 8-position high-speed filter wheel (ASI, FW-1000) which helps to block laser reflections, pre-

vent bleed-through from different channels and blocks autofluorescence from being captured.

For alignment of the two cameras, 100nm Tetraspeck beads were imaged while adjusting the tip/tilt mount. Some instability of the mount means regular alignment is required but the system achieved good registration between both channels. Figure 2.12A shows Tetraspeck beads being imaged with the 647nm dichroic, demonstrating dual-colour imaging and good registration between channels. Figure 2.12B demonstrates widefield multi-colour cellular imaging achieved with the 647nm dichroic. The registration between both channels was quantified by using the ThunderSTORM packages (Ovesný et al., 2014) maximum likelihood estimator function to calculate the position of all the beads in both channels offigure 2.12A. Calculating for every bead the difference in position between channels gives a mean lateral displacement of 57nm. While significant for SMLM imaging, this error can be corrected for *a posteriori* in SMLM datasets. It is, however, small enough that both channels essentially cover the same FOV.

2.2.2 Drift Correction in Super-Resolution Microscopy

Any drift should be the result of the thermal response of different materials in a system as well as the mechanical stability of any elements present. However, axial drift could be observed when imaging beads on the Alpha (figure 2.13). Refocusing the beads restored the signal, demonstrating that the fading signal was because of axial drift and not bleaching. It is therefore imperative to correct for axial drift during acquisitions on the Alpha.

2.2.2.1 ASI CRISP

ASI provide an axial drift correction device termed the Continuous Reflective Interface Sample Placement (CRISP) system. It works by measuring the reflection of an Light Emitting Diode (LED) on the coverslip surface (figure 2.14A). The Alphas CRISP is mounted on a 100*mm* tube lens (ASI) to relay the signal from the LED to the BFP and this tube lens is attached to the drift correction dichroic shown in figure 2.3. For the CRISP to be functional, the LED needs to be focused on

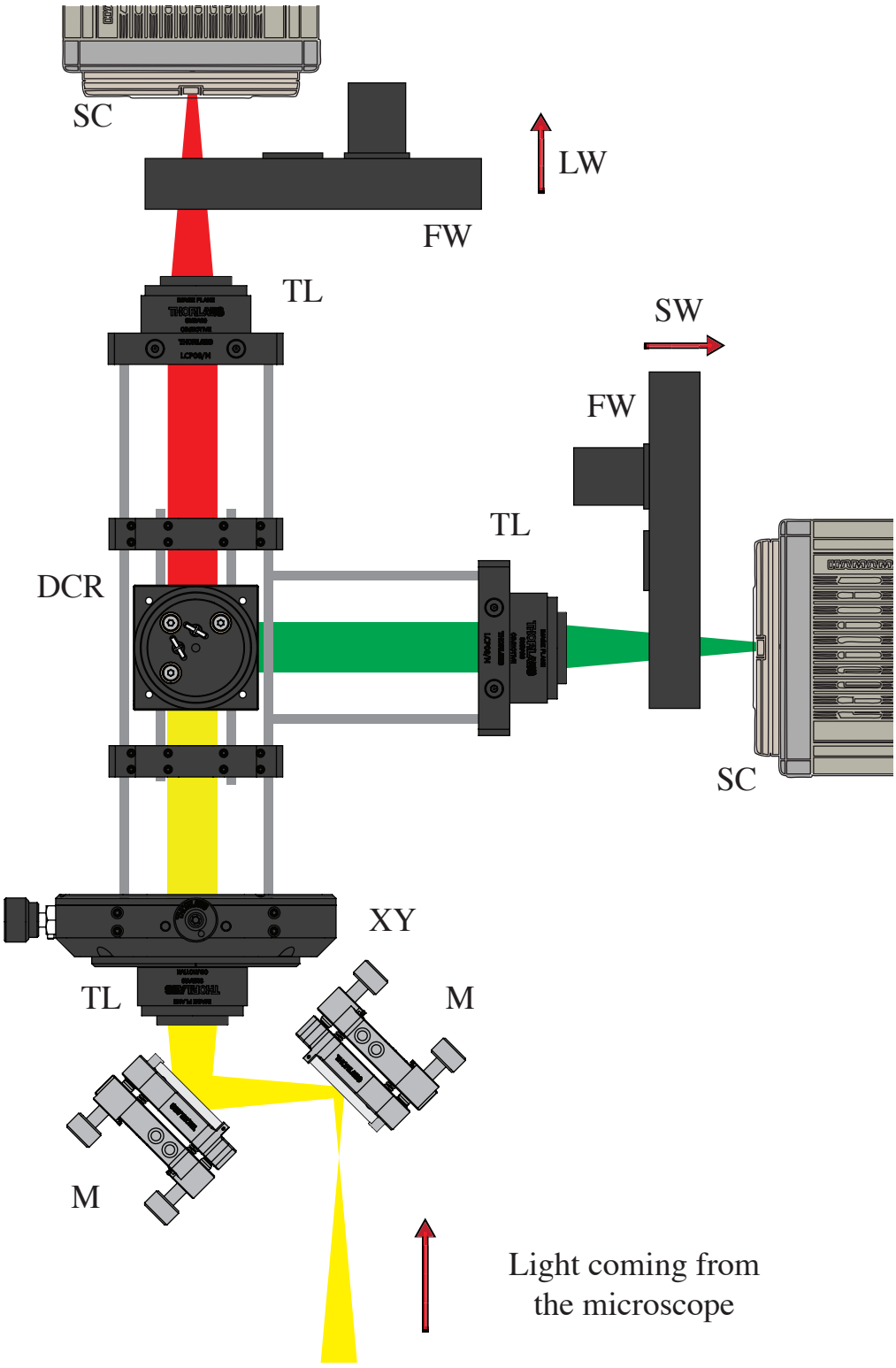

Figure 2.11: Illustrative diagram of the fluorescence emission splitting path. M - mirror; TL - tube lens; XY - XY lens adjustment mount; DCR - dichroic mirror; FW - filter wheels; LW - longer wavelength fluorescence emission; SW - shorter wavelength fluorescence emission; SC - sCMOS camera.

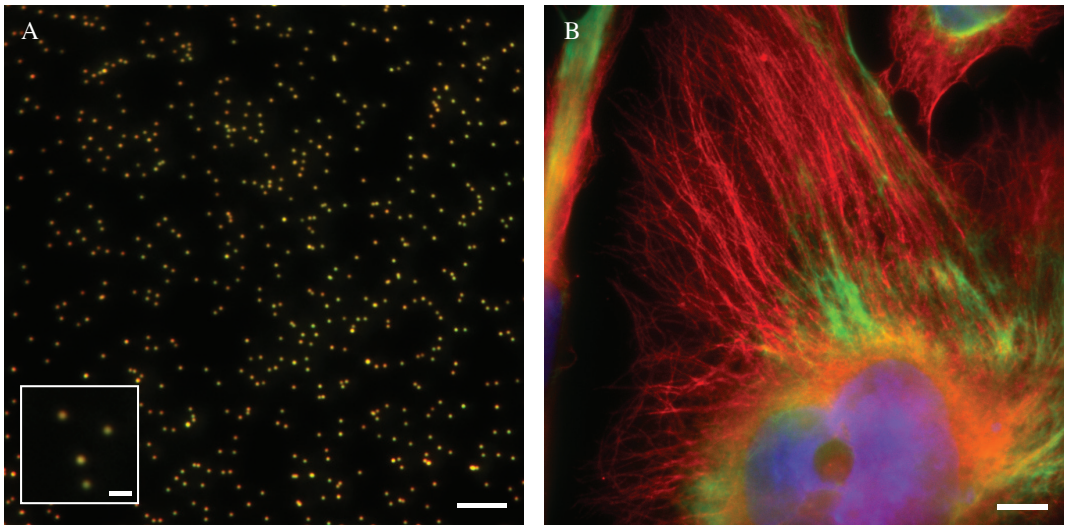

Figure 2.12: Demonstration of dual colour imaging with two cameras. A - Tetraspeck beads illuminated with 561 and 640 nm lasers to demonstrate dual colour imaging with two cameras; Scale bar - $5\mu m$; Inset - zoom of beads from the center of the field of view; Inset Scale bar - $2\mu m$; B - CHO cells immuno-labelled for microtubules, vimentin and nucleotides, imaged with the two cameras and the 657nm dichroic; Red channel - microtubules secondarily labelled with Alexa Fluor 647; Green channel - vimentin secondarily labelled with Alexa Fluor 488; Blue channel - DAPI staining; Scale bar - $5\mu m$.

the roughly the same focal plane as the emission cameras. Given that the emission path is split by a custom lens system, this confocality was verified by removing all dichroic and emission filters from the optical path, imaging Tetraspeck beads and turning on the CRISP LED. Two images were acquired, one of the beads and another of the CRISP LED. Figure 2.14B and C demonstrates that both systems were in focus. Despite the efforts to make the system in focus with the cameras, and despite frequent contact with the manufacturer, the CRISP system was never able to correct for axial drift. This is one of the main reasons why it was decided to develop the system discussed in the next section.

2.2.2.2 3D Cross-Correlation by Static Reference

Correcting drift using cross-correlation has the advantage, when compared to the CRISP system, that it can also perform lateral drift correction in real-time. SMLM samples are often fixed but images of blinking fluorophores are inherently variable, which means the raw data of an SMLM acquisition cannot be matched to a reference image. In order to obtain an image of the sample that can be matched to

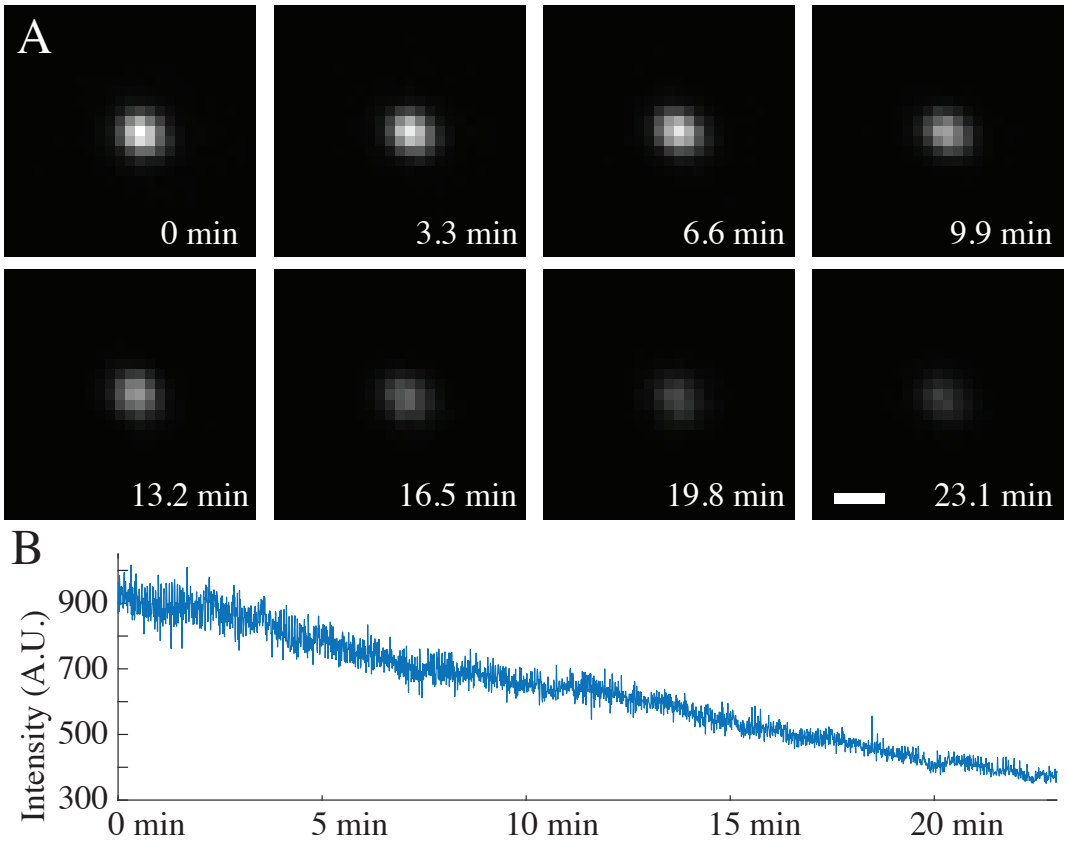

Figure 2.13: Measurement of axial drift over time using Tetraspeck beads. A - frames from a time series of a clump of beads drifting away from focus; B - plot of the average fluorescence intensity (in arbitrary units) of the time series. Scale bar - 0.5μm.

a static reference, a separate transmitted IR light illumination system was installed (figure 2.15). It is based on Köhler illumination, which is an optical configuration designed to obtain homogeneous illumination (Cox, 2010). First, the CRISP system was removed and replaced by a CMOS camera (IDS Imaging, UI-1220LE-M-GL). A small cage system was mounted on a post attached to the microscope stage. It contains an IR LED (Thorlabs, LED1050E, 1050nm) and two lenses. The LED is placed at the back-focal plane of a collector lens which projects the LED light onto a condenser lens. The condenser lens then illuminates the sample on the microscope stage. The light which is transmitted through the sample is collected by the microscope objective and reflected by a dichroic onto the CMOS camera. In this way, an image of the sample can be obtained which is independent of the SMLM acquisition path.

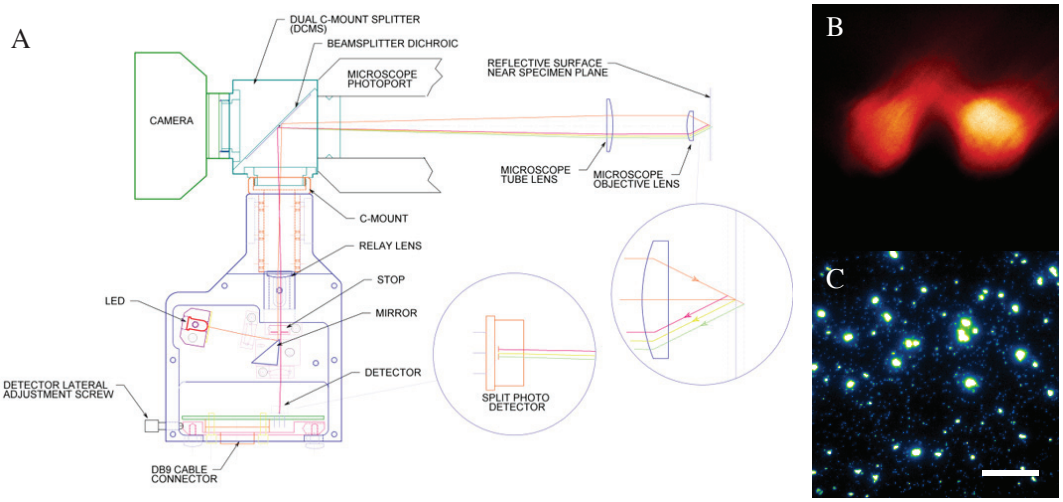

Figure 2.14: A - Illustrative diagram of the CRISP's optical path, adapted from Applied Scientific Instrumentation (2017a). Briefly, the image of an LED light source is projected on the surface of the coverslip. The reflected signal from the LED is captured by a split photodetector. Any axial shift in the coverslip will result in a lateral displacement on the split photodetector and drift can then be corrected for accordingly; B - The signal from the CRISP after the IR filter was removed from the camera path; C - Tetraspeck beads illuminated with 640nm laser light are shown to be at the same focus as the CRISP unit.

To correct for drift in real-time, a Micro-Manager plugin was developed. When the plugin is started, three reference images are acquired: one of the sample when it is in focus and two for when it is moved by a user-specified distance (s) above and below the focus. In order to calculate the lateral drift, the CCM between the in-focus reference IR image of the sample and a current IR image of the sample is calculated using equation (2.2). To detect the coordinates of the peak correlation value, we selectively upscale the correlation matrix via bi-cubic spline interpolation (Catmull et al., 1974) and find its maximum. This process has been previously described in (Guizar-Sicairos et al., 2008). The detected peak position is then subtracted from the nominal center of the image, yielding the lateral displacement. The X and Y piezo stages can then be used to corrected for the lateral displacement.

The axial displacement is calculated using a modified version of the method described in McGorty et al. (2013). First, the peak intensities of the CCMs of the in-focus image with the top image ($C_{+,0}$), bottom image ($C_{-,0}$) and itself ($C_{0,0}$), are calculated. The peak intensities of the CCMs between any new image n and all three of the reference images ($C_{+,n}, C_{-,n}, C_{0,n}$) will then be calculated. From these

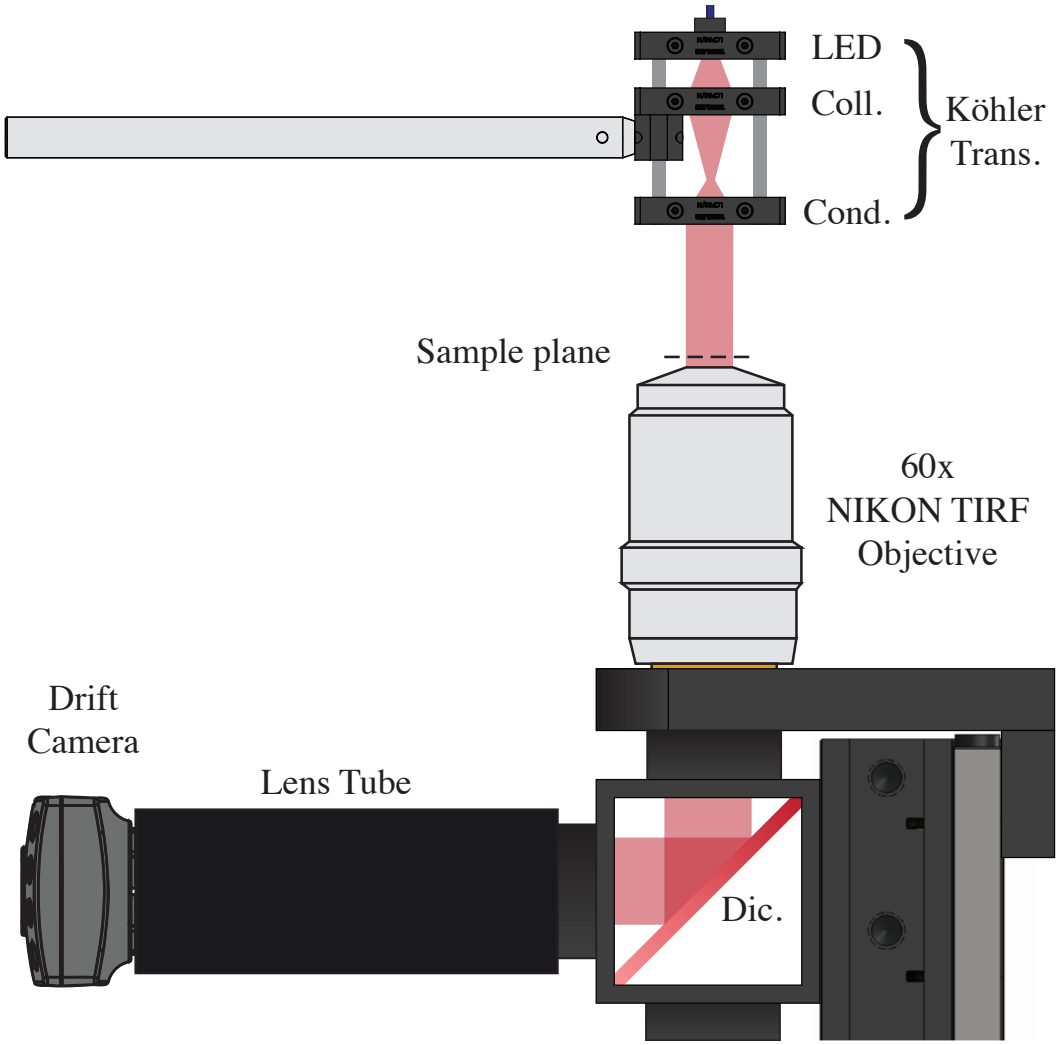

Figure 2.15: Diagram of the optical path for the drift correction hardware. It primarily consists of a Köhler trans-illuminator, a dichroic, a tube lens and a camera. Semi-transparent red areas represent IR light. Köhler Trans. - Köhler trans-illuminator; Coll. - collector lens; Cond. - condenser lens; Dic. - dichroic mirror;

values, the following equations can be used to determine the axial drift between the reference stack and the current sample position:

$$\Delta z = s\left(\frac{2(\Delta\zeta - C_{-,0})}{C_{-,0}}) - 1\right) \tag{2.3}$$

$$\Delta\zeta = \zeta_n - \zeta_0 \tag{2.4}$$

$$\zeta_n = \frac{C_{+,n} - C_{-,n}}{C_{0,n}} \tag{2.5}$$

However, the IR images require processing before the CCMs are calculated since they have a specific background pattern originating from three sources. First, the CMOS camera introduces a read-out artefact in the images that results in a thin white bar at the top and bottom of the drift correction images. The signal from the cell in the CCM is swamped by the signal from these white bars (figure 2.16A, C). Raw images need first to be cropped to remove the cross-correlation signal from the white bars (figure 2.16D). The sensor also introduces a fixed pattern in the image which is largely unnoticeable by eye. Additionally, the illumination is not completely homogenous. Both of these factors contribute to a static background pattern. Any background non-uniformity is strongly represented in the CCM and swamp the cross-correlation signal from the cells (figure 2.16D). One method to remove this background non-uniformity that does not require much prior knowledge of the sample is to filter from the images any frequencies below an arbitrary threshold, using a cut-off filter implemented in Fourier space (Cox, 2010). While this results in a significant removal of the background signal (figure 2.16E-H), there is still enough background signal that prevents the cellular signal from being identified consistently. An alternative method consists of obtaining a reference image of the background prior to any acquisition and then dividing any subsequent image by this reference. The resulting images should mostly consist of contrast derived from the cell. The reference image can be a picture of a completely empty field, but for samples which are too dense or with too much debris, this can be difficult to obtain. A solution was developed, consisting of acquiring several mostly empty fields, regardless of the presence of cells or debris, and then perform a median projection. This will result in an image where each pixel corresponds to the median value of the image sequence and if the raw images consist of mostly empty fields, the resulting image will correspond to the background. Figure 2.16E and J show two images background corrected by this method. The resulting CCM's (figure 2.16K and L) have a very clear cellular signal present, allowing the cell's drift to be identified

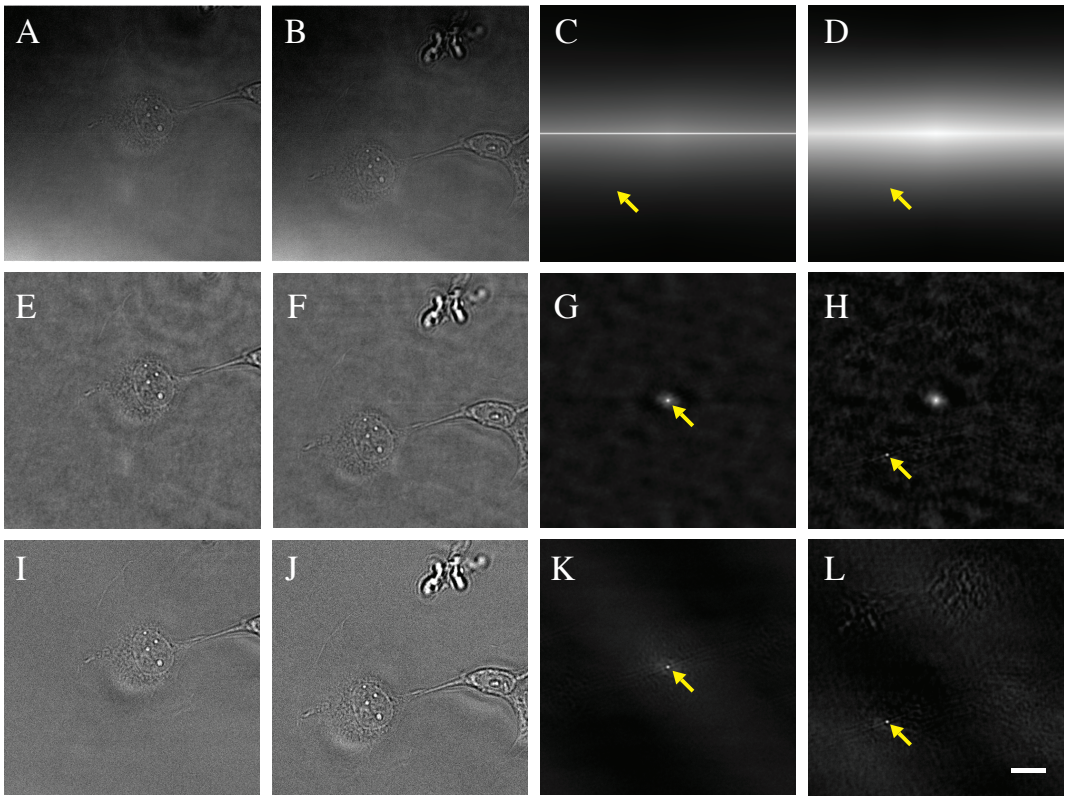

Figure 2.16: Image processing for cross-correlation. The cross correlation algorithm is sensitive to any pattern that appears in both of the images that are being compared. This includes both the structure of the cells and the structure of the background. Yellow arrows - expected location the cell's cross-correlation signal in the respective maps; A,B - cell before (A) and after (B) moving; C,D - CCM of A with B before (C) and after (D) cropping, respectively; E,F - FFT filtered images of A and B, respectively; G - CCM of E with another filtered image of the cell in the same position; H - CCM of E with F; I,J - A and B after background correction, respectively; K - CCM of I with another corrected image of the cell in the same position; L - CCM of I with J; Scale bar - 20μm.

over time, as figure 2.17 shows. It demonstrates axial drift that was measured over a 35 minute period using the CCSR algorithm.

To measure the linearity of the response of the algorithm, two stacks were acquired. In one, the piezo stage was used to move a cell in X and Y by 30μm and in another, the stage was moved 1.5μm in Z. Figure 2.18A and C demonstrate that the response of the algorithm is linear. There is, however, an error associated with the position estimate. To measure this error, a static cell was imaged over 296 frames and its position was estimated in X, Y and Z. By calculating the difference between each estimated positions and the average of the estimated position, the error can be determined from the standard deviation of the differences. In the X and Y direc-

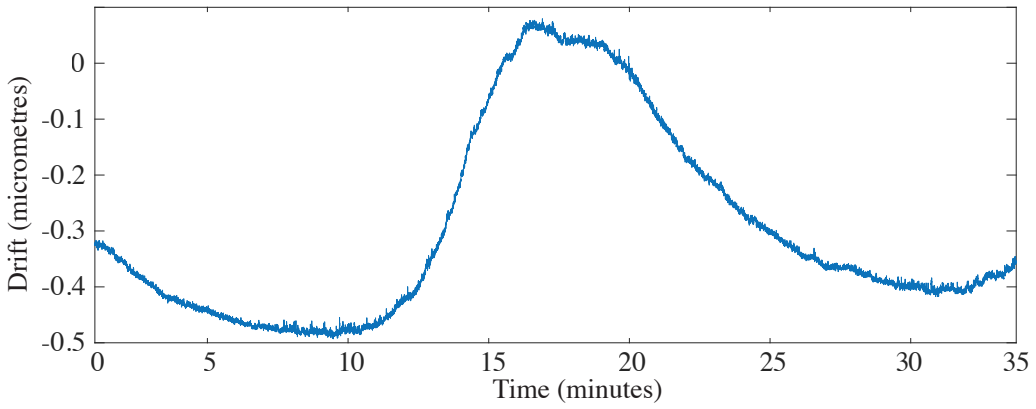

Figure 2.17: Measurement of z-displacement due to drift over a 35 minute period using the cross-correlation by static reference algorithm.

tion, the standard deviation is 4.4 nm and in Z it is 33.5 nm. If the distributions are somewhat normal, one can estimate that 95 % of the estimates will fall within 2 standard deviations above and below the mean. The histograms for the estimate errors fit well to a Gaussian distribution (XY Adjusted R-square: 0.988; Z Adjusted R-square: 0.9658). This means that one can expect a maximum deviation of $\pm 8.8nm$ in XY and $\pm 67nm$ in Z. The error in XY is below the maximum resolution that can be expected in a SMLM microscope. For most acquisitions and applications it should not meaningfully impact the final reconstruction. This means that single acquisitions would most likely not require further drift correction when correcting lateral drift using the cross-correlation signal. The drift correction error in Z is also well below the expected depth of field for our 1.49 NA objective. The depth of field corresponds to the distance above and below the nominal focus of the objective where signal from the sample remains in focus. One can estimate the depth of field of an objective by following equation (2.6) (Nikon, 2016).

$$dof = \frac{\lambda * n}{NA^2} + \frac{n}{M * NA} e \tag{2.6}$$

Here, dof is the depth of field, λ is the wavelength of light being imaged, n is the refractive index of the objective medium, NA is the numerical aperture of the objective, M is the magnification of the objective and e is the smallest distance that

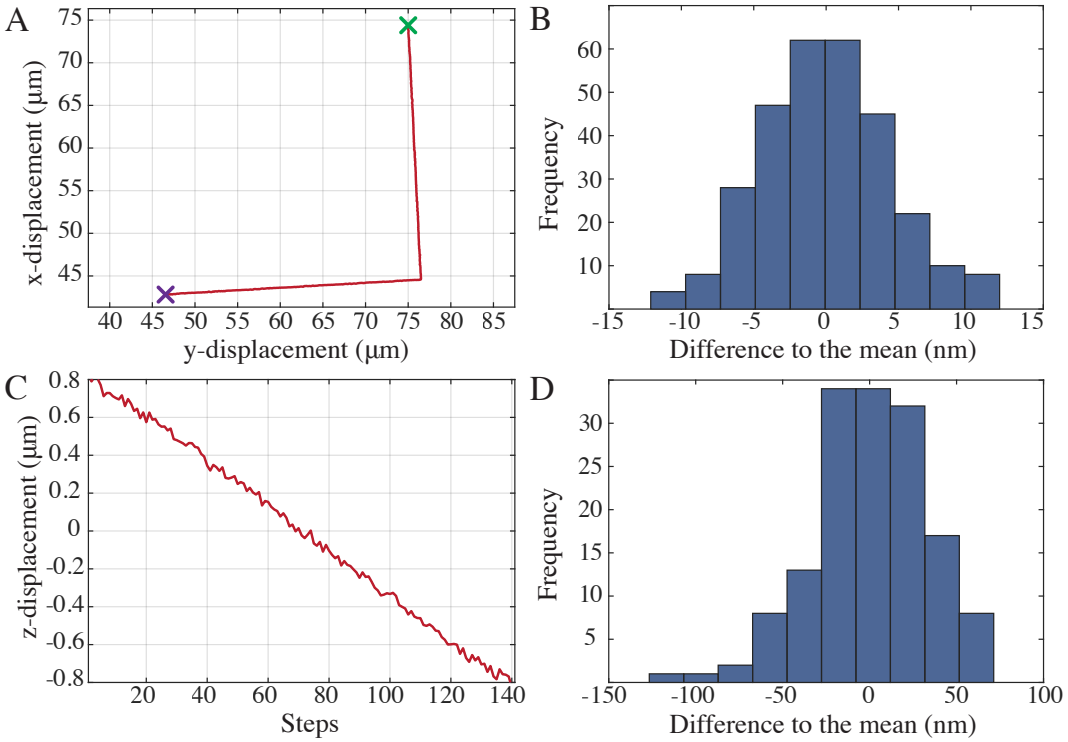

Figure 2.18: Sensitivity and linearity of the Cross Correlation by Static Reference algorithm. A - plot of the estimated movement of the cell between figure 2.16A and B, after moving 30μm in Y and 30μm in X; Green cross marks the beginning of the movement and the purple cross marks the end of the movement; B - histogram of the difference of the estimate in X or Y to the mean position of a static cell. n=296; C - estimated z-displacement from a stack with 10nm steps; D - histogram of the difference of the estimated position in Z to the mean position of a static cell. n=296.

can be resolved by a detector that is placed in the image plane. For digital systems, e corresponds to the pixel size. Calculating dof for the Alpha when imaging Alexa Fluor 647, the expected depth of field is 635nm. Given our estimated Z error of $\pm$67nm, the CCSR algorithm should be able to maintain the sample in focus without affecting imaging.

However, if vibrations are present in the system, a positive feedback-loop could created which would amplify any vibration. To test if any vibrations are present, a fluorescent bead (Thermo Fisher, T7279) was imaged for 10.000 frames at 1000 FPS. Lateral vibrations were clearly present (not shown). To quantify these vibrations, the pixel corresponding to the centre of the bead was identified on the first frame. The vibrations move the bead away from this pixel and then back to the same position, continuously. Therefore by simply measuring the intensity of this

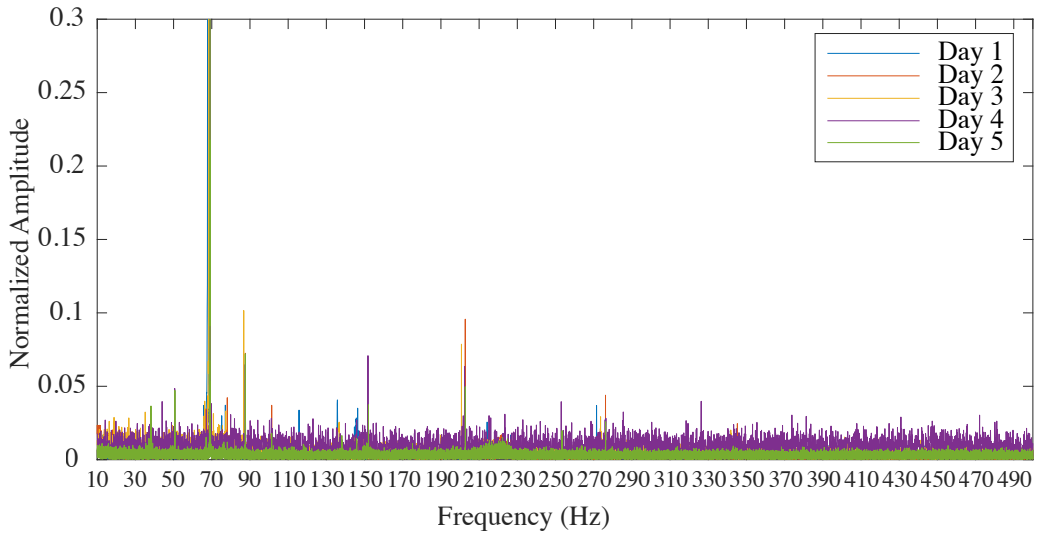

Figure 2.19: Five measurements of microscope vibrations taken at different days reveal an $\approx 70Hz$ vibration present in the Alpha. Plotted are the FFT of the intensity plot of an image pixel that corresponds to a bead location at the beginning of an image stack.

pixel throughout the entire stack will provide a direct measurement of the frequency of the vibrations present. Figure 2.19 shows the normalised Fast Fourier Transform (FFT) of the intensity plots of 5 different beads. Some higher frequency vibrations were detected at $\approx 90Hz$ and $\approx 200Hz$. But an $\approx 70Hz$ vibration is present whose amplitude is up to an order of magnitude stronger than any other vibration present. These vibrations are present even if the rooms air conditioning is turned off. Given this is within the range of vibration frequencies expected from a camera fan, the cameras are potentially the source of these vibrations. To prevent these vibrations from interfering with the drift correction algorithm, it is run at a frequency which is lower than the vibrations present in the system.

The entire algorithm was packaged as a Micro-Manager plugin (figure 2.20). While it is installed as a plugin, it also encapsulates a separate Micro-Manager instance which allows the drift correction camera, LED and piezo stage to be controlled independently of the main Micro-Manager interface. The plugin controls any hardware from the main instance in addition to any hardware that is specific to its own instance. A problem that is specific to the ASI microscope is the fact the Piezo 3D stage is identified by micro-manager as 3 separate focusing stages. The drift correction plugin allows the user to specify which stage corresponds to

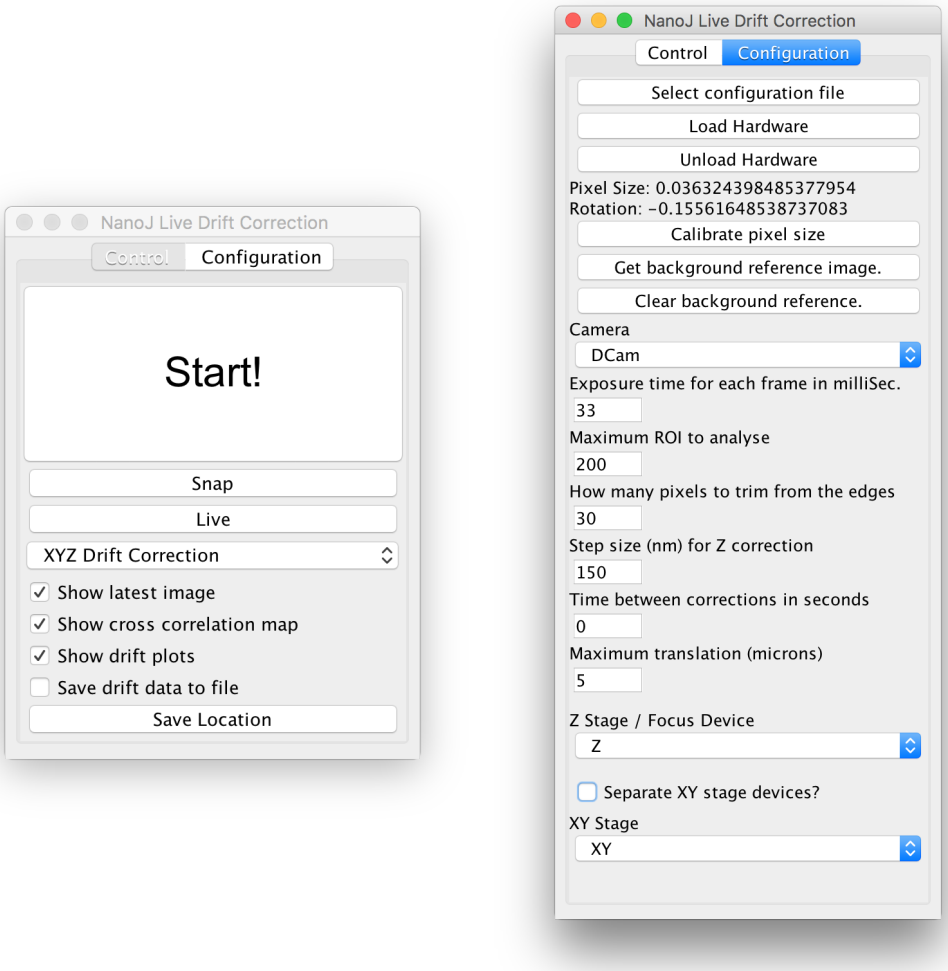

Figure 2.20: Screenshots of the drift Correction Plugin for Micro-Manager.

the X and Y axis and the plugin will treat them as a single XY device. The plugins user interface allows the user to acquire the background reference after choosing a mostly empty area of the sample. It also enables the most relevant drift correction parameters to be adjusted and the impact of these adjustments can be observed by a live view of the camera's processed output. Finally, the drift can be plotted during drift correction and saved as a Comma Separated Values (CSV) file.

2.2.3 Super-Resolution Cellular Imaging at High-throughput

Thus far, it has been established that the Alpha is capable of large FOV imaging and of correcting its own drift. To demonstrate the ability of the Alpha to perform SMLM for longer time durations, HeLa cells were methanol fixed and secondar-

ily immuno-labelled for microtubules with Alexa Fluor 647 and dSTORM imaged. Figure 2.21A shows a 40.000 dSTORM acquisition acquired at 50 FPS. The total time to acquire was ≈14 minutes over which time the drift needed to be corrected with the drift correction plugin (figure 2.21B). The fact the reconstruction in figure 2.21A is without artefacts in spite of the presence of drift demonstrates the plugin was successful in correcting for drift during the acquisition.

A dSTORM image's resolution will be a function of the localisation precision, density and sample structure. The Fourier Ring Correlation (FRC) method (Nieuwenhuizen et al., 2013; Culley et al., 2017) allows the resolution of the image to be estimated based on the super-resolution reconstructions, which will integrate all three parameters. The resolution obtained with FRC for the full dataset in figure 2.21A yields a mean resolution of 54nm (std. dev. 14nm).

The sCMOS camera allows for 1000 FPS imaging when cropped to 128x128 pixels. To test the impact of high-speed imaging, dSTORM acquisitions of 40.000 frame were also acquired at 1000 FPS. Figure 2.22 shows a representative reconstruction, demonstrating dSTORM imaging is feasible at 1000 FPS with a total acquisition time of 40 seconds. Measuring the obtained resolution using the FRC method yields a mean resolution of 86nm (std. dev. 16nm).

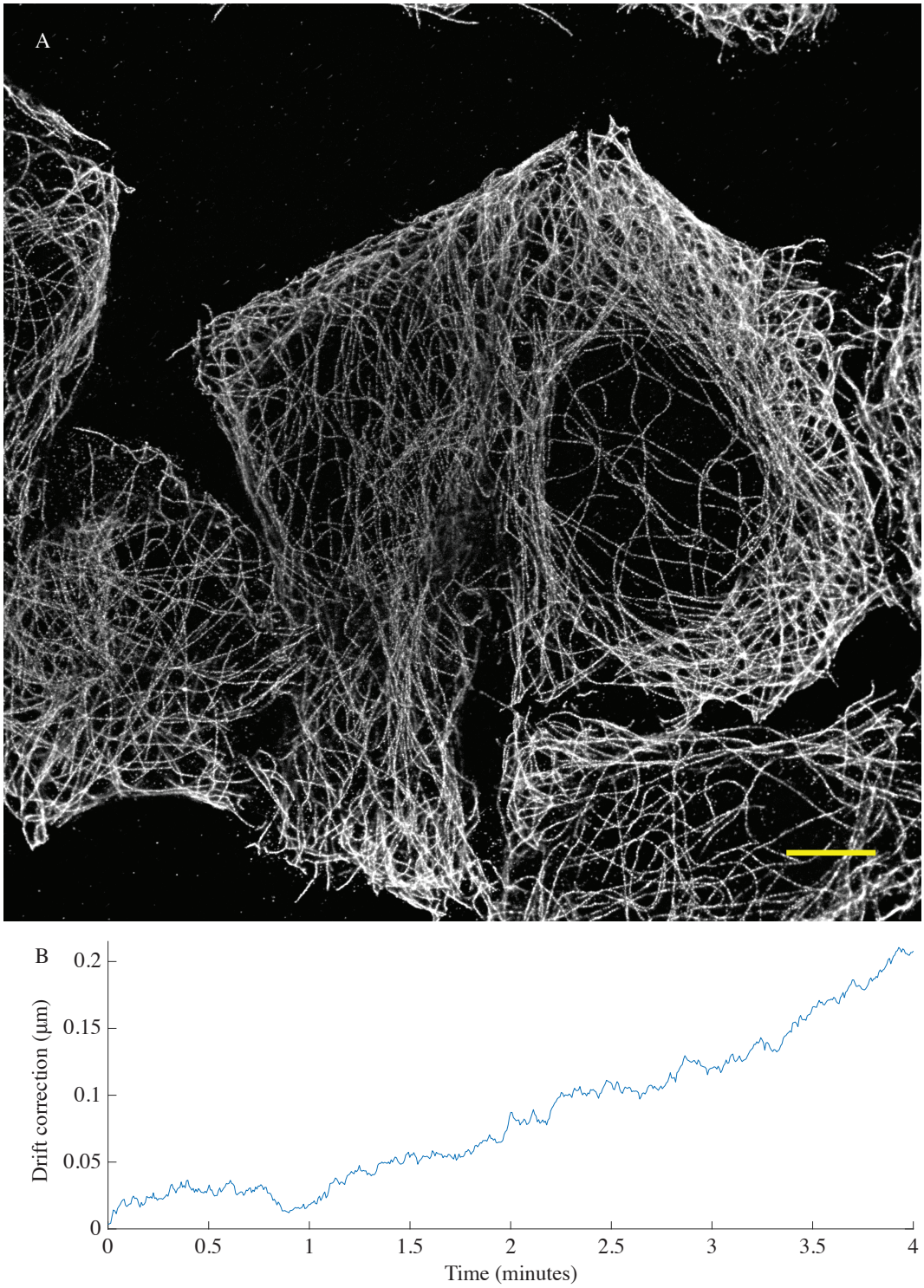

Figure 2.21: dSTORM images acquired while undergoing CCSR drift correction. Scale bar - $5\mu m$. A - dSTORM reconstruction of of cell acquired at 50 FPS; B - plot of the axial drift corrected for during acquisition.

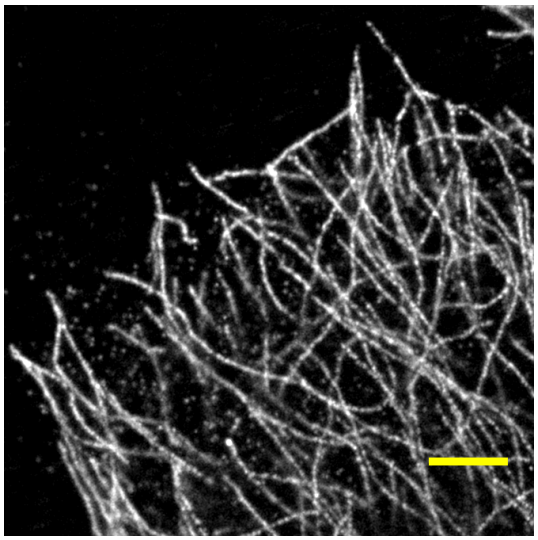

Figure 2.22: High-speed dSTORM reconstruction of cells acquired at 1000 FPS; Scale bar - $2\mu m$.

2.3 Discussion

2.3.1 Throughput of the Alpha

Most commercial systems (Zeiss, 2016; Nikon, 2017a) use EM-CCD cameras with a 512x512, ≈50hz full FOV sensor. They also tend to be illumination intensity limited as they use single-mode fibres for laser launching. As a result, the illumination will be restricted to an area of 256x256 pixels, or $25.6x25.6\mu m^2$, which can be acquired at ≈100 FPS (Andor Technology Ltd, 2016). An sCMOS camera cropped to 256x256 can acquire at an 800 FPS acquisition rate and at 400 FPS when cropped to 512x512 (Hamamatsu Photonics K.K., 2016). As a result, when comparing for the same FOV, the sCMOs is inherently ≈8x faster than an EM-CCD. Figure 2.22 demonstrates that the Alpha can achieve SMLM imaging even at 1000Hz framerates, obtaining a resolution of ≈ 86 nm. At 512x512 or $55x55\mu m^2$, an sCMOS is only 4x faster than a 256x256 EM-CCD but it will cover 4 times the area. This can significantly increase throughput further still. As an example, figure 2.21 shows two HeLa cels that were acquired simultaneously. A cropped field of 256x256 would have resulted in only a single cell being acquired, reducing throughput in half. If cells are spread relatively evenly and are of a size which is more amenable (i.e. T-cells), the Alpha's throughput can be increased by up to 4x when compared to EM-CCD's. Finally, for dual-colour experiments, the use of two cameras will inherently double the throughput. Therefore, for the simplest case of single colour, single cell per FOV acquisitions at 256x256, the Alpha has a throughout increase of 8x when compared to a commercial system. However, if imaging two-colour stained cells that are evenly spread and of an amenable size, the Alpha can have a throughput increase of up to 32x (table 2.4). When considering the entire system can be automated, the Alpha design is demonstrably capable of performing high-throughput SMLM acquisitions.

2.3.2 Illumination Intensity and Throughput in SMLM

By comparing table 2.3 with the results of Lin et al. (2015), it becomes clear that illumination intensity is the Alpha's main limiting factor for high speed full

	Commercial systems	Alpha	Throughput increase
Cameras	1	2	2x
FOV	$25.6x25.6\mu m^2$	$55x55\mu m^2$	4x
Frame-rate	100 Hz	400Hz	4x
Total throughout:			32x

Table 2.4: Comparison of how different elements of the Alpha increase throughput when compared to commercial systems.

FOV SMLM imaging. To obtain the best resolution possible with the current 512x512 FOV, the laser illumination intensity should match the FOV frame-rate (400 FPS). Lin et al. (2015) saw the best results at $\approx 31\,\mathrm{kW\,cm^{-2}}$ for 400 FPS, which would require 16x more laser illumination intensity than currently installed, corresponding to a 2.4W laser. If, furthermore, the entire $221x221\mu m^2$ FOV of the Flash4 were to be required, the laser illumination intensity should match the full FOV frame-rate of 100 FPS. Lin et al. (2015) obtain the best resolution at 100 FPS when imaging at $\approx 8\,\mathrm{kW\,cm^{-2}}$. To be able to cover 16x larger area with 4x the current illumination intensity, the 640nm laser would need to be replaced for a laser source with up to 64x higher illumination intensity ratings, or 9.6W. Such high illumination intensity ratings (2.4-9.6W) are either not generally available commercially or prohibitively expensive but Zhao et al. (2017) have recently demonstrated a vibrated multi-mode fibre system which merges several laser inputs into a single fibre. They make use of a custom-made fused biconical taper (FBT), a fibre component which merges the output of an arbitrary number of multi-mode fibres (4 in their case) into a single multi-mode fibre. By combining the output of four 2W 639nm lasers, they are able to achieve the required illumination intensity for full FOV sCMOS imaging. Should larger FOV be required, this method would be immediately applicable to the Alpha as the main illumination system is already a vibrated multi-mode fibre. However, there is a significant cost associated with such laser systems and as such the 512x512 FOV of the Alpha probably represents a good trade-off between cost, FOV, speed and resolution.

At 50 FPS acquisition rate, the Alpha was shown to obtain reconstructions with a resolution close to what would be expected for the given samples. Considering

a microtubule has a diameter of around 25nm in size and antibodies have a size of around 10nm, the observed size of a secondarily labelled microtubule is expected to range around 45nm (Ries et al., 2012). By imaging at 50 FPS, and with the Alpha's $\approx$2 kW cm^{-2} illumination density, around 54nm resolution was achieved. Lin et al. (2015) achieve similar FRC resolution at a comparable acquisition rate and illumination intensity which indicates this is the ideal acquisition rate for the Alpha. However, since resolution also depends on localisation density, better resolution could be obtained through longer acquisitions. For example, by only considering half of the dataset in figure 2.21, the resolution is lowered to a mean of 64nm (std. dev. 11nm); when considering only a quarter of the frames, the resolution is further lowered to 73nm (std. dev. 21nm). This indicates that larger datasets may improve the obtained resolution. When imaging at 1000 FPS, the system achieved a resolution of around 86nm. However, it also only obtained around half the localisation density when compared to 50 FPS imaging (not shown). When imaging at a similar laser illumination intensity and at 800 FPS, Lin et al. (2015) obtain around 70nm resolution. It remains possible that the lower resolution at 1000 FPS imaging on the Alpha is the result of insufficient localisations being acquired for this particular dataset. The reduction in resolution can potentially be compensated by acquiring longer datasets without substantially affecting throughput, considering the dataset was acquired 20x faster. For a SMLM high-throughput experiment, it then becomes important to determine before-hand what is an acceptable resolution as some samples or labels won't require as much resolution. Any high-throughput experiment should first test the target structures for the kind of resolution they require and determine from there what is the smallest dataset and fastest data-rate that is safe to acquire.

2.3.3 Vibration dampening

There is still, however, room for further improvement. The vibrations present in the system (figure 2.19) are a potential a source of reduced resolution since they can blur the PSF of single molecules, thereby reducing SNR. The most likely culprit are the camera fans which are the only vibrating elements present on the optical

table. To correct for this, fiducial markers can be used during imaging. By applying the Shannon-Nyquist criterion and imaging at rates higher than 70*2.3=161 FPS, any vibration can be detected and corrected for from the movement of the fiducial markers. Ideally the vibrations should be removed from the system altogether. An alternative camera cooling system is water-cooling. This consists of water flowing in a closed system between the camera and a radiator. The radiator will have fans attached to it, which allows the water to be cooled but any vibrations should not be efficiently transmitted to the cameras through the water hoses. The Flash4 cameras present on the Alpha already have water-cooling fittings (Hamamatsu Photonics K.K., 2016). In the future, installing an enclosed water-cooling system on the Alpha could completely remove the need for fiducial markers to correct for vibrations in the system.

2.3.4 Drift Correction in High-throughput

One particular bottleneck is the ability to perform drift corrections at multiple locations. Currently, the drift correction plugin stores only a reference image stack corresponding to one location, it is currently the limiting factor for high-throughput acquisitions. However, it is straightforward for the plugin to store references for different locations. Micro-Manager's multiple location list is programatically accessible through its API. Micro-Manager also allows plugins to keep track of system devices. For multi-position drift correction, in the future the plugin will keep a reference tied to each position on Micro-Manager's list. Whenever the stage is moved to a previous position on the list, or a new position, the drift correction can detect this movement automatically and use the correct reference image stack for that particular position. Additionally, it can potentially detect any new position automatically and acquire a reference stack without user intervention. This should be particularly useful for any multi-position experiment that requires visiting all positions on the list repeatedly.

2.4 Methods

2.4.1 Cell Culture

HeLa and CHO cells were cultured at 37°C in 60*mm* plastic petri dishes using Dulbecco's Modified Eagle's Medium (Thermo-Fisher, 31053-028) supplemented with 10% FBS (Sigma, F9665), 1% GlutaMAX (Thermo Fisher, 35050-038) and 1% penicillin-streptomycin (Thermo-Fisher, 15140122). Every two to three days they were split by washing the media with pre-warmed Phosphate Buffered Saline (PBS: NaCl 137*mM*; KCl 2.7*mM*; Na_2HPO_4 10*mM*; KH_2PO_4 1.8*mM*; pH 7.4), replacing the PBS with 3*mL* of pre-warmed Trypsin-EDTA (Thermo-Fisher, 5400-054) and incubating until the cells were seen to be in suspension by phase-contrast microscopy. To maintain the culture, 7*mL* of pre-warmed media was added to the cell suspension and cells were diluted to new dishes at a typical ratio of 1:10, adjusted according to confluency. For imaging experiments, 100μL of cell suspension was added to 35*mm* glass-bottom cell culture dishes (Ibidi, 80606) with 2*mL* of pre-warmed media. The cells were allowed to grow overnight and were washed twice with pre-warmed Ringer's solution (0.12*M* NaCl, 1.5*mM* $CaCl^2$, 5*mM* KCl, ph 7.3) before staining or imaging.

2.4.2 Immuno-Staining

Cells were fixed while at 37°C with pre-warmed 4% Paraformaldehyde (Taab Laboratories, P026) diluted in PBS for 10 minutes. Subsequent staining steps were performed at room temperature. Cells were washed three-times for 3 minutes with PBS and permeabilised by adding 0.1% Triton-X/PBS (Sigma, T8787) for 10 minutes. Cells were blocked by incubating in 5% bovine serum album and 0.5% Tween-20 (Sigma, P9416) in PBS for 30 minutes prior to incubating for 1 hour with an Alpha-tubulin primary antibody at 1/200 dilution (Sigma, T6199). Cells were washed three-times for 3 minutes with PBS and incubated for 1 hour with a Goat anti-mouse secondary antibody labelled with Alexa Fluor 647 at a 1/200 dilution (Thermo Fisher, A-21236) Cells were washed three-times for 3 minutes with PBS and imaged in PBS.

2.4.3 dSTORM Imaging

Cells were first immersed in a dSTORM buffer: 150mM Tris (Sigma, T3253) pH 8, 1% glucose (Sigma, G8270), 1% glycerol (Sigma, G2025), 10mM NaCl (Sigma, S3014), 40$\mu g/mL$ catalase (Sigma, C40), 0.5mg/mL glucose oxidase (Sigma, G2133) and 1% β-mercaptoethanol (BME; Signa, M6250). 640nm laser intensity was set to maximum and the fluorophores were allowed to reach a low density state, which required 30 seconds. The camera then acquired a sequence of 40.000 frames (unless otherwise stated) at a given frequency (mentioned in the text). The resulting images were analysed with the ThunderSTORM SMLM package (Ovesný et al., 2014). The settings were as follows: images were filtered using a B-Spline wavelet filter (Order: 3, Scale 2); the molecule localisation was first determined using the local maximum method and this localisation was further refined using the maximum likelihood estimator. After the localisations were obtained, drift was corrected for using ThunderSTORM's cross correlation facility. Reconstructions of the super-resolved localisations were done using the average shifted histograms method.

2.4.4 Software Development and Image Analysis

All Java software was written using IntelliJ and the Beanshell scripting facility of Micro-Manager was used to prototype code sections and test microscope control through Java. All image processing and analysis was performed in FIJI (Schindelin et al., 2012), and Python was used to both automate processing tasks and prototype Java classes. The frequency analysis in figure 2.19 was performed in Matlab from intensity measurements obtained in FIJI as described in the text. The tracks in 2.18 were obtained as described in the text, using custom Java classes controlled by Python scripts inside FIJI. The error measurements in 2.18 were obtained using Matlab to calculate the histogram values of measurements obtained in FIJI, as above. Firmware code for Arduino was written and tested using the Arduino IDE.

2.4.5 Bead preparations

To track drift (figure 2.17), test vibrations (figure 2.19), register the two camera channels (figure 2.12), and test the CRISP system (figure 2.14), fresh bead preparations were used. $1\mu L$ of $100nm$ fluorescent beads were diluted in $100\mu L$ PBS, and vortexed. The bead solution was then added to a cell culture dish and allowed to settle for 30 minutes before imaging.

2.4.6 Laser Intensity Measurements

Laser intensity was measured with a photodiode power pensor (Thorlabs, S121C) attached to a digital hand-held power meter (Thorlabs, PM100D).

2.5 Bibliography

Almada, Pedro, Siân Culley and Ricardo Henriques. 'PALM and STORM: Into large fields and high-throughput microscopy with sCMOS detectors.' In: *Methods (San Diego, Calif.)* 88 (Oct. 2015), pp. 109–21. ISSN: 1095-9130. DOI: 10.1016/j.ymeth.2015.06.004.

Andor Technology Ltd. *iXon EMCCD Cameras | Andor*. 2016. URL: http://www.andor.com/cameras/ixon-emccd-camera-series (visited on 10/02/2017).

Applied Scientific Instrumentation. *CRISP Autofocus System | ASI*. 2017. URL: http://www.asiimaging.com/index.php/products/focus-tracking-stabilization/crisp-autofocus-system/ (visited on 01/08/2017).

— *Modular Infinity Microscope (MIM) | ASI*. 2017. URL: http://www.asiimaging.com/index.php/products/modular-infinity-microscope/modular-infinity-microscope-mim/ (visited on 01/08/2017).

— *Modular Infinity Microscope (MIM) Rapid Automated Modular Mounting (RAMM) And Video Test Stand (VTS-2100) Systems Instruction Manual*.

— *Rapid Automated Modular Microscope System (RAMM) | ASI*. 2017. URL: http://www.asiimaging.com/index.php/products/complete-system-solutions/rapid-automated-modular-microscope-ramm-system/ (visited on 01/08/2017).

Arduino. *Arduino - Home*. URL: https://www.arduino.cc/ (visited on 21/08/2017).

Bates, Mark et al. 'Multicolor super-resolution imaging with photo-switchable fluorescent probes.' In: *Science (New York, N.Y.)* 317.5845 (Sept. 2007), pp. 1749–53. ISSN: 1095-9203. DOI: 10.1126/science.1146598.

Catmull, Edwin and Raphael Rom. 'A Class of Local Interpolating Splines'. In: *Computer Aided Geometric Design*. Vol. 14. 97. Elsevier, 1974, pp. 317–

326. ISBN: 9780120790500. DOI: 10.1016/B978-0-12-079050-0.50020-5.

Cox, Guy. *Optical Imaging Techniques in Cell Biology, Second Edition*. CRC Press, 2010, p. 316. ISBN: 1439848254.

Culley, Siân et al. 'NanoJ-SQUIRREL: quantitative mapping and minimisation of super-resolution optical imaging artefacts'. In: *bioRxiv* (2017).

Fujimaki, Yosuke and Hirokazu Taniguchi. 'Reduction of speckle contrast in multimode fibers using piezoelectric vibrator'. In: ed. by Alexis V. Kudryashov et al. Vol. 8960. Mar. 2014, 89601S. DOI: 10.1117/12.2037431.

Guizar-Sicairos, Manuel, Samuel T. Thurman and James R. Fienup. 'Efficient subpixel image registration algorithms.' In: *Optics letters* 33.2 (Jan. 2008), pp. 156–8. ISSN: 0146-9592. DOI: 10.1364/OL.33.000156.

Gustafsson, Nils et al. 'Fast live-cell conventional fluorophore nanoscopy with ImageJ through super-resolution radial fluctuations'. In: *Nature Communications* 7 (Aug. 2016), p. 12471. ISSN: 2041-1723. DOI: 10.1038/ncomms12471.

Hamamatsu Photonics K.K. *ORCA-Flash4.0 V2 Digital CMOS camera C11440-22CU | Hamamatsu Photonics*. 2016. URL: https://www.hamamatsu.com/us/en/product/category/5000/5005/C13440-20CU/index.html (visited on 10/02/2017).

Huang, Bo et al. 'Three-dimensional super-resolution imaging by stochastic optical reconstruction microscopy.' In: *Science (New York, N.Y.)* 319.5864 (Feb. 2008), pp. 810–3. ISSN: 1095-9203. DOI: 10.1126/science.1153529.

Huang, Fang et al. 'Video-rate nanoscopy using sCMOS camera-specific single-molecule localization algorithms.' In: *Nature methods* 10.7 (July 2013), pp. 653–8. ISSN: 1548-7105. DOI: 10.1038/nmeth.2488.

Inoué, Shinya and Kenneth R. Spring. *Video Microscopy: The Fundamentals*. Springer, 1997, p. 741. ISBN: 0306455315.

Juette, Manuel F et al. 'Three-dimensional sub-100 nm resolution fluorescence microscopy of thick samples.' In: *Nature methods* 5.6 (June 2008), pp. 527–9. ISSN: 1548-7105. DOI: 10.1038/nmeth.1211.

Leica. *Leica adaptive Focus control*. 2015. URL: https://www.leica-microsystems.com/fileadmin/downloads/Leica%20DMi8%20for%20Advanced%20Imaging/Brochures/Leica%7B%5C_%7DDMi8%7B%5C_%7DAFC-Flyer%7B%5C_%7Den.pdf (visited on 31/07/2017).

Lewis, J P. 'Fast Normalized Cross-Correlation'. In: *Vision Interface* 10.1 (1995), pp. 120–123.

Lin, Yu et al. 'Quantifying and optimizing single-molecule switching nanoscopy at high speeds.' In: *PloS one* 10.5 (2015), e0128135. ISSN: 1932-6203. DOI: 10.1371/journal.pone.0128135.

Linde, Sebastian et al. 'Direct stochastic optical reconstruction microscopy with standard fluorescent probes.' In: *Nature protocols* 6.7 (July 2011), pp. 991–1009. ISSN: 1750-2799. DOI: 10.1038/nprot.2011.336.

Mattheyses, Alexa L, Sanford M Simon and Joshua Z Rappoport. 'Imaging with total internal reflection fluorescence microscopy for the cell biologist.' In: *Journal of cell science* 123.Pt 21 (Nov. 2010), pp. 3621–8. ISSN: 1477-9137. DOI: 10.1242/jcs.056218.

McGorty, Ryan, Daichi Kamiyama and Bo Huang. 'Active Microscope Stabilization in Three Dimensions Using Image Correlation.' In: *Optical nanoscopy* 2.1 (2013), pp. 1–7. ISSN: 2192-2853. DOI: 10.1186/2192-2853-2-3.

Mlodzianoski, Michael J. et al. 'Sample drift correction in 3D fluorescence photoactivation localization microscopy'. In: *Optics Express* 19.16 (2011), p. 15009. DOI: 10.1364/OE.19.015009.

Nieuwenhuizen, Robert P J et al. 'Measuring image resolution in optical nanoscopy.' In: *Nature methods* 10.6 (Apr. 2013). ISSN: 1548-7105. DOI: 10.1038/nmeth.2448.

Nikon. *Depth of Field and Depth of Focus | MicroscopyU*. 2016. URL: https://www.microscopyu.com/microscopy-basics/depth-of-field-and-depth-of-focus (visited on 21/08/2017).

— *Specifications | N-STORM Super-Resolution | Super-Resolution | Products | Nikon Instruments - Microscopes and Imaging Systems*. 2017. URL: http://www.nikoninstruments.com/en%7B%5C_%7DGB/Products/Super-Resolution/N-STORM-Super-Resolution/Specifications (visited on 07/01/2016).

— *The Nikon Perfect Focus System (PFS) | MicroscopyU*. 2017. URL: https://www.microscopyu.com/tutorials/the-nikon-perfect-focus-system-pfs (visited on 31/07/2017).

Olympus. *Z drift compensator*. 2017. URL: https://www.olympus-lifescience.com/en/microscopes/inverted/ix83/ix3-zdc2/ (visited on 31/07/2017).

Ovesný, Martin et al. 'ThunderSTORM: a comprehensive ImageJ plug-in for PALM and STORM data analysis and super-resolution imaging.' In: *Bioinformatics (Oxford, England)* (Apr. 2014). ISSN: 1367-4811. DOI: 10.1093/bioinformatics/btu202.

Pawley, James B., ed. *Handbook Of Biological Confocal Microscopy*. 3rd. Boston, MA: Springer US, 2006, p. 988. ISBN: 978-0-387-25921-5. DOI: 10.1007/978-0-387-45524-2.

Ries, Jonas et al. 'A simple, versatile method for GFP-based super-resolution microscopy via nanobodies.' In: *Nature methods* 9.6 (June 2012), pp. 582–4. ISSN: 1548-7105. DOI: 10.1038/nmeth.1991.

Rust, Michael J, Mark Bates and Xiaowei Zhuang. 'Sub-diffraction-limit imaging by stochastic optical reconstruction microscopy (STORM).' In: *Nature methods* 3.10 (Oct. 2006), pp. 793–5. ISSN: 1548-7091. DOI: 10.1038/nmeth929.

Schindelin, Johannes et al. 'Fiji: an open-source platform for biological-image analysis.' In: *Nature methods* 9.7 (July 2012), pp. 676–82. ISSN: 1548-7105. DOI: 10.1038/nmeth.2019.

Thompson, Russell E, Daniel R Larson and Watt W Webb. 'Precise nanometer localization analysis for individual fluorescent probes.' In: *Biophysical journal*

82.5 (May 2002), pp. 2775–83. ISSN: 0006-3495. DOI: 10.1016/S0006-3495(02)75618-X.

Wang, Yina et al. 'Localization events-based sample drift correction for localization microscopy with redundant cross-correlation algorithm.' In: *Optics express* 22.13 (2014), pp. 15982–91. ISSN: 1094-4087. DOI: 10.1364/OE.22.015982.

Winterflood, Christian M. et al. 'Dual-Color 3D Superresolution Microscopy by Combined Spectral-Demixing and Biplane Imaging'. In: *Biophysical Journal* 109.1 (2015), pp. 3–6. ISSN: 00063495. DOI: 10.1016/j.bpj.2015.05.026.

Wolter, S et al. 'Real-time computation of subdiffraction-resolution fluorescence images.' In: *Journal of microscopy* 237.1 (Jan. 2010), pp. 12–22. ISSN: 1365-2818. DOI: 10.1111/j.1365-2818.2009.03287.x.

Zeiss. *Definite Focus*. 2017. URL: https://www.zeiss.com/microscopy/int/products/light-microscopes/axio-observer-for-biology/definite-focus.html (visited on 31/07/2017).

— *ELYRA superresolution microscopy*. URL: http://www.zeiss.com/microscopy/en%7B%5C_%7Dde/products/superresolution-microscopy.html%7B%5C#%7Ddownloads (visited on 07/01/2016).

Zhao, Zeyu et al. 'High-power homogeneous illumination for super-resolution localization microscopy with large field-of-view'. In: *Optics Express* 25.12 (June 2017), p. 13382. ISSN: 1094-4087. DOI: 10.1364/OE.25.013382.

Chapter 3

Open-Source fluidics for *In-situ* Liquid Exchange

3.1 Introduction

3.1.1 Microfluidics for Microscopy

Microfluidic technology has enabled many applications which are unique to the field like lab-on-a-chip diagnostic devices (Sackmann et al., 2014), organ-on-a-chip research models (Bhatia et al., 2014), cell-sorting (Reece et al., 2016) and others (Duncombe et al., 2015). These applications can be achieved by leveraging the unique properties of fluid flow at small scales (Beebe et al., 2002). The ability to control the pressure and fluid flow inside the device also allows mechanosensory systems to be studied in living cells (Polacheck et al., 2013). Because PDMS can be covalently bonded to glass, flow-cell devices allow cells to be imaged on a microscope at high-resolution while the cellular environment can be manipulated. This combination of microscopy and microfluidics allows, for example, super-resolution fixed imaging to be correlated with live-cell imaging of the same cells (Tam et al., 2014). Microfluidic devices have also been used to imobilize yeast (Bell et al., 2013) and mouse embryonic stem cells (Zhou et al., 2016) for prolonged periods, enabling PALM imaging to be performed on live-cells. Microfluidics are then capable of enhancing imaging experiments and specifically, super-resolution experiments. To achieve this, microfluidic systems need to be designed with imaging in

mind and these generally follow a common architecture composed of 3 main components: a PDMS flow-cell, the connecting tubing and a pumping system.

3.1.2 Microfluidic Flow-Cells

To make a PDMS device, there are three main steps: design, mould fabrication and assembly. The design step involves using Computer Aided Design (CAD) software to draw the overall outline of the desired microfluidic pattern. These designs can include complex features such as valves, fluid mixers and pumps (Beebe et al., 2002) and fluid simulation software can be used to predict the behaviour of the device (Chován et al., 2002). The pattern is then reproduced on a mould using one of a variety of techniques. A common method to make moulds for PDMS devices is photolithography, which allows for features as small as $1\mu m$ to be made in the mould. Photolithography is often performed inside clean-rooms, or filtered air environments, to prevent any defects in the mould which may arise from dust in the air. Once the mould is made, a mixture of PDMS elastomer and a curing agent is mixed and poured on to the mould. While the PDMS may cure at room temperature over a 24 hour period, it can also be cured in a few hours if heated. Once the PDMS is cured, any number of required inlets and outlets can be cut out using a hole-punch (figure 1.3). A hole-punch is a hollow metal cylinder with sharp edges. It can be made to punch through the PDMS, resulting in a cylinder of the material being cut-out of the device. Finally, a coverslip and the PDMS device are activated using an oxygen plasma reactor. The plasma creates silanol functional groups (SiOH) on the surface of the PDMS which allow it to covalently bond to the glass surface of the coverslip (Duffy et al., 1998). The PDMS is carefully placed on to the coverslip, bonding to it and thereby creating a microfluidic device. The holes which were previously punched can now be interfaced to tubing, forming inlets and outlets to allow liquid flow. Liquid can be injected through the tubing and it will flow through the channels which have been imprinted on the PDMS by the mould. Because these devices act as contained cells where liquid flows through, they are also called flow-cells.

3.1.3 Plumbing for Fluidics

To connect the pumps to the fluidic devices themselves, some form of tubing is also required. Most commonly, flexible and chemically inert polymer tubing (such as Tygon brand tubing) are used. Another option the silica capillaries used in High-Performance Liquid Chromatography (HPLC). HPLC instruments are designed around flowing small amounts of liquid through tubing and are therefore designed to minimize the volume required for one experiment. These instruments use silica capillaries with internal diameters as low as $0.2\mu m$ and have manifolds which allow many capillaries to merge into one path with minimal dead volume (see below). One thing to consider with tubing is the dead volume, or the minimum volume required for liquid to reach the cells. As an example, a 1 metre length of tubing with an internal diameter of $0.8mm$ will have an internal volume of $500\mu L$. This means a syringe needs to have at least $500\mu L$ of liquid as well as enough liquid to fill other sources of dead volume, as well as the volume of the flow-cell itself. For expensive substances such as antibodies or drugs, this is not a reasonable volume. Therefore the tubing should have as low an internal diameter as possible.

3.1.4 Pump Types for Fluidics

In a flow-cell device, the liquid can be made to flow by using pumps. Syringe pumps, pressure pumps and peristaltic pumps are all commonly used for this purpose. Peristaltic pumps move liquid inside a flexible tube by using rollers which constrict the tubing at several points along its length (figure 3.1 A). One end of the tube is placed inside a reservoir of liquid and the other end is connected to a microfluidic device. A motor then moves the rollers along the tubing, forcing the contents inside to move along the direction of the motor rotation, moving the liquid from the reservoir to the device. Pressure pumps (figure 3.1 B) work by increasing the air pressure inside a sealed container containing both liquid and air (figure 3.1 B:C). An inlet tube connects to the top of the container, and the entrance for an outlet tube is placed at the bottom of the container. The generated pressure at the top of the container forces the liquid at the bottom of the container through the outlet

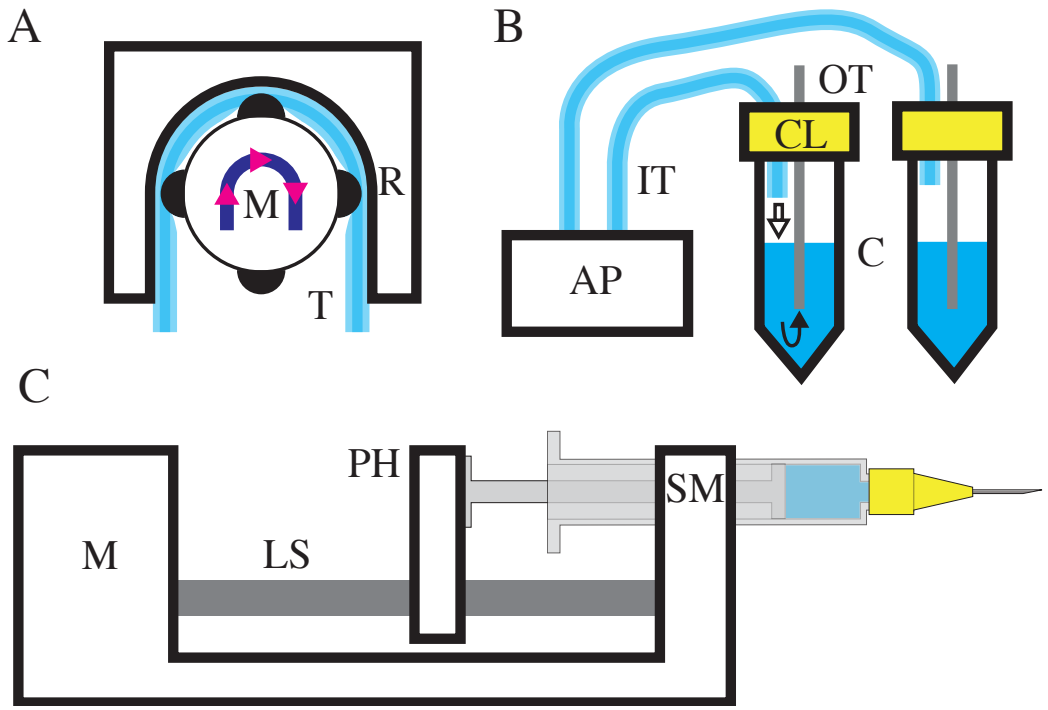

Figure 3.1: Diagrams for two different pump types. A - Peristaltic pump. Arrows show direction of the pump motion and liquid flow. T - Tubing; M - Motor; R - Roller; B - Pressure pump. White arrow - direction of air pressure; Black arrow - direction of liquid movement; AP - Air Pressure generator; IT - Inlet tube; OT - Outlet tube; CL - Container Lid; C - Containers; C - Syringe pump. M - Motor; LS - Lead Screw; PH - Plunger holder; SM - Syringe mount.

tube, wich is connected to the flow-cell. To control the flow-rate out of the outlet, pressure pumps precisely control their internal pressure by opening and closing pressure valves in a fast manner. Syringe pumps operate by using a syringe as a reservoir and simply push on the plunger to inject liquid. Figure 3.1 C shows a diagram of a syringe pump with a syringe mounted on it. The syringe plunger is held by a plunger holder, and the plunger holder attaches to a lead screw through a lead nut. When the motor inside the pump housing rotates the lead screw, the lead nut moves along the screw, resulting in the plunger being pushed (or pulled, depending on direction) and in liquid injection. Syringe pumps are more versatile, precise and create a more stable flow than peristaltic or pressure pumps. Partially this is because syringe pumps use stepper motors instead of the Direct Current (DC) motors used in peristaltic pumps and the pressure valves in pressure pumps. DC motors run freely when a current is applied but stepper motors move in pre-determined steps.

This stepping motion requires a complex electronic scheme where pulses of electric current are sent to separate circuits to achieve a step motion. DC motors can run at high RPM but will not achieve high torques and it is difficult to get DC motors to achieve a precise number of rotations. Stepper motors move in precise steps and can achieve high torques but are significantly costlier and are limited in the speeds they can achieve. For complex multi-step experiments, such as immuno-stainings, several pump devices may be required; one for each buffer or solution. One advantage of pressure pumps is a single air pressure source can control several containers by using different valve systems (figure 3.1 B). However, these systems are significantly more costly than syringe pumps or peristaltic pumps due to the complexity of the pressure valve systen and its associated electronic control schemes. One other consideration is the fact most pumps have their own proprietary software which does not integrate with microscope software for integrated acquisition.

3.1.5 Open-Source Fluidics for *In-situ* Liquid Exchange

Microfluidic devices have largely been designed to leverage the physics of small scale fluid flow. However, there are many microscopy applications which require only a simple fluid exchange. For example, imaging mitosis in mammalian cells is difficult due to the low number of cells which are undergoing mitosis at any given time. Cells can be synchronised by growing them with a cell cycle inhibiting drug. If the medium containing the drug is exchanged for fresh medium without the inhibitor, the cells will enter mitosis synchronously and this will greatly increase the number of cells which can be used in a particular experiment (Rosner et al., 2013). More generically, other types of drugs can be added/removed/exchanged to a cell's medium to study cellular function. Additionally, cell fixation can be achieved by replacing the medium with a fixative of the correct percentage or by adding a concentrated fixative solution and allow it to dilute *in-situ* to the correct concentration. By staining after for any number of targets of interest, live and fixed imaging can be correlated, reintroducing the dynamic context of the cell to the fixed imaging data. An example of a more complex series of exchange steps is immunocytochemistry. Performing an immuno-staining on fixed cells is achieved by a sequence of

steps (Breu et al., 2010): adding and removing a fixative; washing by adding and removing buffer; permeabilising the cells by adding and removing a detergent; detecting antigens by adding and removing a dilute antibody solution; etc... With an automated fluidic system, all of the above processes (drug application, fixation and immuno-staining) can be performed in the same sample in a straightforward manner.

For imaging experiments, fluid manipulation steps have commonly been performed separately from the imaging process. Cells are commonly drugged, fixed and stained before they are imaged. The ability to perform any of the steps described above while imaging cells can greatly enhance the informative power of an experiment. For example, focal adhesions are cellular structures which are important for cell motility (Burridge et al., 1996; Parsons et al., 2010). These cellular structures, which are important for cell motility, are inherently a dynamic, a critical aspect that is lost when imaging fixed cells. For example, if any change in the structural components of focal adhesions results in higher or lower cellular speed, this can not be determined from fixed cell imaging. To make such a link, a researcher would have to find a method to influence cell speed, either by using drugs or through genetic manipulation. The impact of this manipulation would have to be thoroughly characterised on both experimental and control populations. Following this, imaging the structural components of focal adhesions for both populations would have to be performed and finally, both the cell speed and structural imaging datasets would have to be correlated together to establish a potential link between both. By imaging live cells on a microscope, followed by fixing, staining and imaging the exact same cells, a direct observation of this relationship would be possible in a single experiment. Such an observation would have greater statistical power as variability arising from measuring control and experimental conditions would not be conflated with the variability inherent to cellular processes.

To perform *in-situ* experiments, researchers have manually applied drugs to the cells while imaging on a microscope but this is a fraught and error-prone process. It is therefore attractive for biological researchers to have a method to exchange or add

liquids with minimal disruption to samples while these are mounted on the microscope. Ideally, these steps would be performed in a reliable and automated manner and one way to achieve this is through the use of PDMS microfluidic devices and automated pumps. Despite this, the use of PDMS flow-cells has not been considerably popularised. This is likely due to the complexity of microfluidic systems, the cost of specialised equipment and software, as well as a skill-set and a knowledge base which most biological researchers lack.

It is the goal of this chapter to describe a fluidic framework, NanoJ-Optofluidics, which is accessible to most biological researchers, is highly multiplexed, is capable of addressing many simple fluid exchange protocols, can perform experiments *in-situ* during live-imaging and is capable of integrating with the microscope acquisition. In addition, to facilitate wide availability, all components will be made publicly available through the Open Science Framework website (Center for Open Science, 2017) as an Open-Source project.

3.2 Results

3.2.1 A Fluidic Platform for Liquid Exchange *In-situ*

3.2.1.1 LEGO-based Syringe Pumps

The goal of an open-source hardware project is to make the end-product widely accessible to a large audience. There are several considerations that enable this: cost; access to materials; simplicity of design; compatibility with current materials; and speed of assembly and repair. LEGO bricks were designed as mass-produced modular building blocks for children's toys. One key feature of their industrial production is the very low tolerance of brick manufacturing, down to $20\mu m$, resulting in highly standardized parts (The LEGO Group, 2014; Allain, 2013). Since their introduction to market, they have become readily and affordably available worldwide and many researchers readily have access to LEGO-bricks of many types. The introduction of the LEGO Technic brand has made electronic elements available which are compatible with LEGO-bricks, including DC motors and linear actuators. Overall, LEGO parts possess the ideal combination of features which can enable and open-source hardware project to be widely accessible. Given this, the NanoJ-Optofluidics framework was developed using LEGO parts.

The LEGO Technic brand does not include stepper motors and early designs of peristaltic fluid pumps using LEGO were unreliable. Therefore, the NanoJ pumps were designed to be DC motor driven syringe pumps. To make a syringe inject liquid, its plunger needs to be pushed into the body of the syringe in a linear motion. LEGO Technic parts include linear actuators which convert the rotary motion of motors to linear motion, and this motion can be used to push the syringe plunger. The syringe pumps were designed around these linear actuators (figure 3.2 A). A pump unit consists of one DC motor (figure 3.2 M), two linear actuators (figure 3.2 LA) and a set of gears (figure 3.2 G). For many microfluidics applications, the native speed of the DC motors was found to be too high and the relatively small torque was also found to result in insufficient force to push some syringes. Aside from power transmission, the primary purpose of the gear train is to reduce the

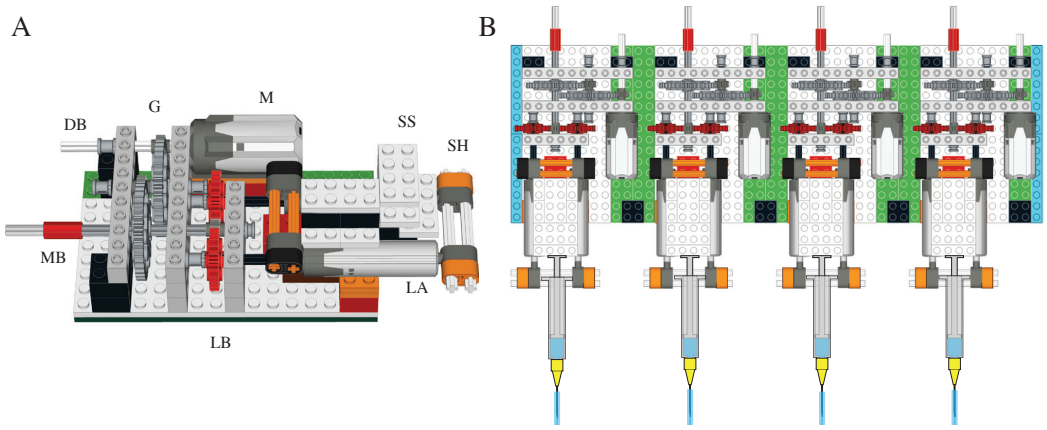

Figure 3.2: A - 3D diagram of a fully retracted single NanoJ-Optofluidics pump device. The linear actuators are usually extended to allow a full syringe to be mounted (see B). M - DC motor; G - Gear train; DB - Motor disengagement bar; MB - Manual control bar; LA - Linear actuators; SS - Syringe stop; SH - Syringe holder; LB - LEGO boards; B - 3D diagram of four multiplexed NanoJ-Optofluidics pump devices with syringes. Note the linear actuators are fully extended, whereas in A they are fully retracted.

DC motor's speed and increase torque. The total gear ratio of the gear train leads to a 75-fold speed reduction. Because any decrease in speed due to the gear ratio also increases torque proportionally, the gear train of the LEGO pumps results in a 75-fold amplification of the motor torque. This has been found adequate for most subsequent microfluidics applications. The gear train transmits the rotary motion of the motor to two linear actuators which are mounted parallel to each other. A solid lego block sits in between the actuators and the ends of the actuators are connected by two bars for rigidity. The space between the solid block and the bars is the syringe mounting point (mounted syringes can be seen in figure 3.2 B). The syringe body is held to the bars (figure 3.2 SH) by means of rubber-bands and the plunger sits flush against the solid block (figure 3.2 B). The weight of a fully loaded syringe means they tend to tip over the front of the pump. To prevent this, a small LEGO plank is placed on top of the solid block (figure 3.2 SS) to hold the plunger in place and prevent the syringe from tipping over. The entire assembly is mounted on two LEGO boards (figure 3.2 LB) which both increases the rigidity of the pump as well as enables the pumps to be multiplexed when the boards are placed in a staggered arrangement (figure 3.2 B).

The speed of injection (or flow-rate) of a syringe pump will be a function of

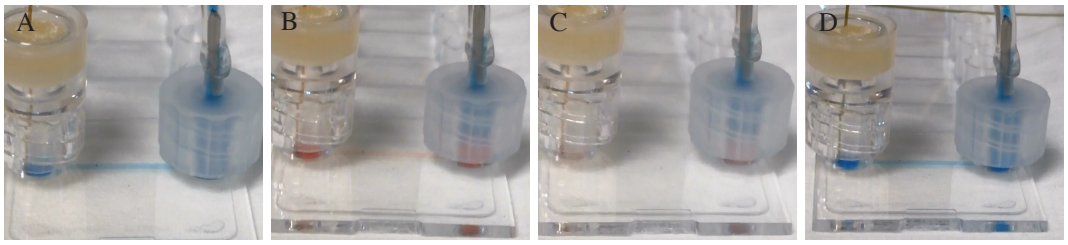

Figure 3.3: Demonstration of liquid exchange on a commercial microfluidic slide. The inlet is shown in the left-hand side of the images and the outlet on the right-hand side. Liquid was merged using silica capillary tubing and the manifold shown in figure 3.8. First, a Methyl-Blue solution flowed through the slide (A); This was then exchanged by a Phenol-Red solution (B), followed by (C) water and, finally, the water was replaced by Methyl-Blue solution (F).

the speed of the translation of the linear actuators and the internal diameter of the syringe. To determine the speed the LEGO pumps can achieve, a pump was mounted with a 1ml syringe (BD, 300013; internal diameter of 4.699mm) and with a flat piece of Parafilm placed at the mouth of the syringe. By applying a 9V voltage to the motor, the pump injected water at full speed for 60 seconds. Because of the parafilm, the water beaded up, allowing it to be easily retrieved. The mean recovered volume was 137μL (n=12, std. dev. 9μL or 6.4% of the mean). Thus, the maximum flow-rate of the lego pumps will be 2.3$\mu L/s$, at least for syringes with an 4.699mm internal diameter. To determine the accuracy of the pump, the motor was run for 43.48 seconds at maximum speed with the intention of achieving 100μL of injected water. The recovered mean volume was 98.4μL (n=10, std. dev. 3.43μL or 3.5% of the mean). Nevertheless, the pump design shown in figure 3.2 has been used to exchange liquids reliably and figure 3.3 demonstrates liquid exchange on a commercial flow-cell device (Ibidi, 80606) using a multiplexed array as shown in figure 3.2 B.

Given a reference flow-rate and diameter, the flow-rate for any other syringe diameter (R_d) can be determined using equation (3.1):

$$R_d = R_r \left(\frac{d}{d_r} \right)^2 \tag{3.1}$$

Where d is the syringe diameter, d_r is the reference diameter and R_r is the refer-

ence rate. Given equation (3.1), the operating flow-rate for all other syringe types is determined using the calibrated value of $2.3\mu L/s$ for a $4.699mm$ diameter syringe. This method has shown consistent results when using syringes from different manufacturers (BD and Terumo) and volumes ranging from $2ml$ to $50ml$ (not shown). Table 3.1 shows the calculated flow-rates expected for different syringe sizes, which demonstrates the ability of the pumps to cover a broad range of speeds, depending on the syringe diameter. Because the range of the linear actuators is limited, a syringe may not be able to be loaded with the plunger fully retracted, which limits the volume that can be loaded on a syringe. Table 3.1 also shows the maximum volume that can be loaded into a given syringe.

Nominal Vol.	Max. L. Vol.	Inner Dia.	Max. F.R	Min. F.R
1	0.75	4.699	2.3	0.6
2	2.5	8.7	7.9	2.0
5	4.8	11.989	15.0	3.7
10	6. 5	14.427	21.7	5.4
20	11	19.05	37.8	9.5
50	22	26.594	73.7	18.4

Table 3.1: Flow-rates obtained from equation (3.1) for several BD Plastipak syringes. The minimum flow-rate was given as 25% of the maximum value (see section 3.2.1.3). Nom. Vol. & Max. L. Vol.- Nominal and maximum loading volume in *mL*; Inner Dia. - Internal diameter in *mm*; Max. F.R. & Min. F.R - maximum and minimum flow-rates in $\mu L/s$, respectively.

3.2.1.2 3D Printed Syringe Pump

While LEGO is ubiquitous, the Technic brand only provides DC motor functionality. To leverage the precision and torque of stepper motors, another approach is required. 3D printing is slowly becoming ever more available, enabling many researchers to produce their own parts. While not as ubiquitous as LEGO, 3D printing can provide a universal method to fabricate standardised parts without requiring specialised tools. As a theoretically more precise alternative to LEGO pumps, a 3D printed pump prototype was created to leverage the precision of stepper motors (figure 3.4), and this was based on a prior multiplexable Open-Source design (Negrier, 2015).

The pump is built around a stepper motor (figure 3.4 SM) which is attached to

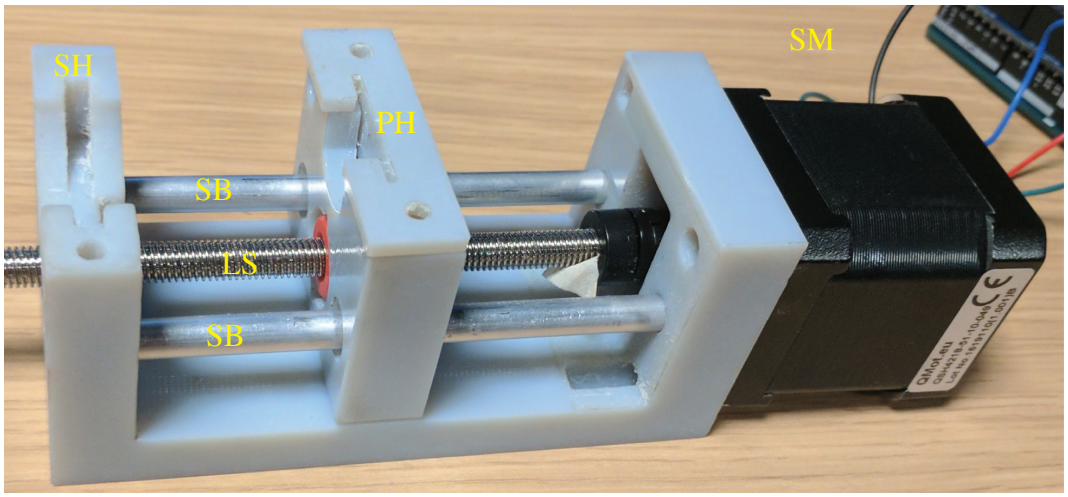

Figure 3.4: 3D printed syringe pump prototype. SM - Stepper motor; LS - Lead screw; SB - Support bar; PH - Plunger holder; SH - Syringe holder.

a lead screw (figure 3.4 LS). The lead screw is rotated in place by the stepper motor. Running along-side the lead screw are two support bars (figure 3.4 SB) which serve as rails for the syringe plunger holder (figure 3.4 PH). The holder slides smoothly on the bars and they help to ensure the holder moves along a straight line. To make the plunger holder move, a lead nut connects it to the lead screw. The rotating motion of the lead screw pushes or pulls on the lead nut depending on the direction of rotation, leading to motion of the plunger holder. A syringe's body is attached to the syringe holder (figure 3.4 SH) by means of a slotted adapter (not shown) and the action of the plunger holder pushes the syringe plunger towards the syringe body. In this way, a syringe can be made to inject liquid. The prototype can translate the plunger holder but requires refinement, as it has yet to achieve stable motion. This is most likely due to observed differences between the expected required size of the printed parts versus the non-printed parts. The electronic control scheme (see section 3.2.1.3) also requires work as the motor seems to stall frequently.

3.2.1.3 Control Systems for Integrated Microscope and Fluidic Applications

To design the pump array as a fully automated system, a complete software and electronic control scheme is needed that is suited for multiple DC motors and, potentially, stepper motors. When choosing the electronic control scheme, the cri-

teria mentioned above also apply: cost; access to materials; simplicity of design; compatibility with current materials; and speed of assembly and repair. The Arduino open-source hardware project (Arduino, 2017) fits these criteria. It was created in 2004 with the goal of developing hardware controllers which are widely available, low-cost, thoroughly documented and with a large community of developers providing support. Figure 3.5 shows an exponential growth of mentions of Arduino in scholarly articles in both the Google Scholar and Web of Science platforms.

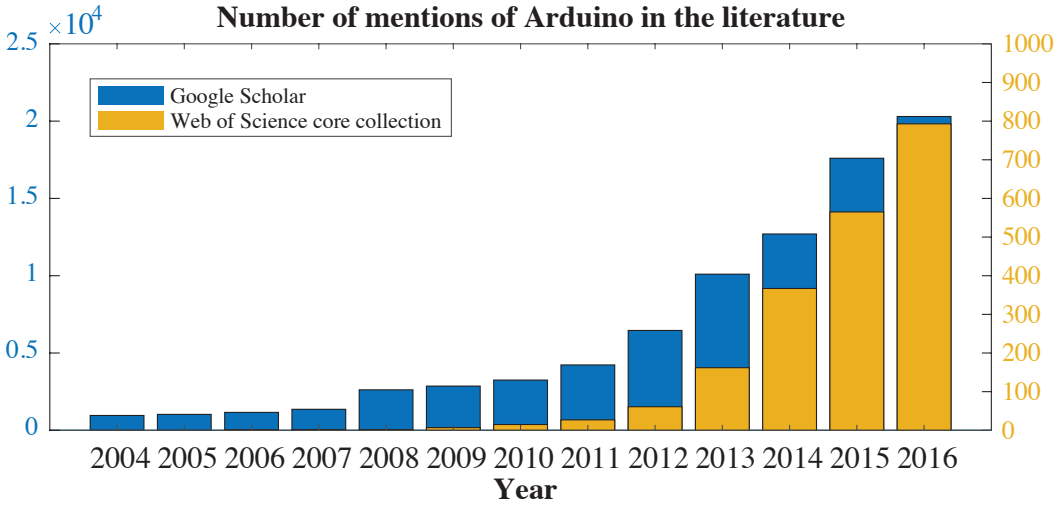

Figure 3.5: Number of mentions of Arduino in scholarly articles. Exponential fits of the Google Scholar (Adjusted R-Squared: 0.9866) and Web of Science (Adjusted R-Squared: 0.9796) data show an exponential growth of interest in the platform.

The electronic controller was chosen to be an Arduino Uno. This Arduino electronic controller can connect to a computer through a USB cable and uses the RS-232 (Serial) protocol for communication. This makes it widely compatible with the majority of modern computer operating systems and hardware. To modulate the pump flow-rate, the motor speed can be controlled using Pulse Width Modulation (PWM). This is an electronic control method where, instead of applying a constant DC current, the electronic controller sends pulses of DC current at a fixed frequency. With PWM, the speed of the motor s follows equation (3.2):

$$s = s_m \left(\frac{pl}{f} \right) \tag{3.2}$$

Where s_m is the maximum speed of the motor, pl is the length of time a pulse lasts and f is the pulse frequency. By controlling the pulse length, the speed of the motor can be modulated. The control scheme needs to be able to be able to perform PWM and to start and stop an electric current to multiple motors at different times. While the Arduino Uno does not provide these capabilities by itself, it is designed to be easily extended with additional electronic components called shields, which are simply plugged on top of the Arduino Uno. The Adafruit motor shield (*Adafruit Motor Shield V2 for Arduino* 2015) allows up to 4 DC motors or 2 stepper motors to be controlled with PWM from a single shield and can be stacked with up to 32 shields of the same type. Thus, the combination of an Arduino Uno and Adafruit motor shields stacked together can provide a single electronic controller capable of controlling up to 128 DC motors or 64 stepper motors in parallel. Figure 3.6 A shows an Arduino stacked with 3 motor shields. While the Arduino Uno draws power from a USB connection to the computer, a separate 9V power supply (not shown) is used to provide power to the motors separately to prevent electric noise from the computer power to the Arduino from affecting motor operation. However, when performing PWM, the torque is reduced and the DC motors may not have sufficient torque push the syringe plunger at lower speeds. For the LEGO Tecnic motors, the speed could not be lowered beyond 25% or it would stall and the minimum pump speed was set at 25% of the maximum flow-rate for any given syringe.

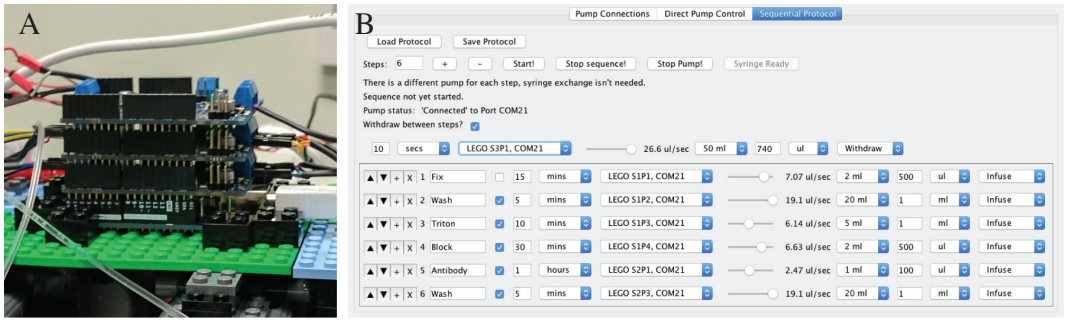

Figure 3.6: NanoJ-Optofluidics control systems. A - Arduino board with three Adafruit Motor Shields; B - Screenshot of the sequential protocol section of the NanoJ-Optofluidics control software.

The combination of multiplexed LEGO syringe pumps and Arduino/Adafruit controllers compose the hardware component of the NanoJ-Optofluidics frame-

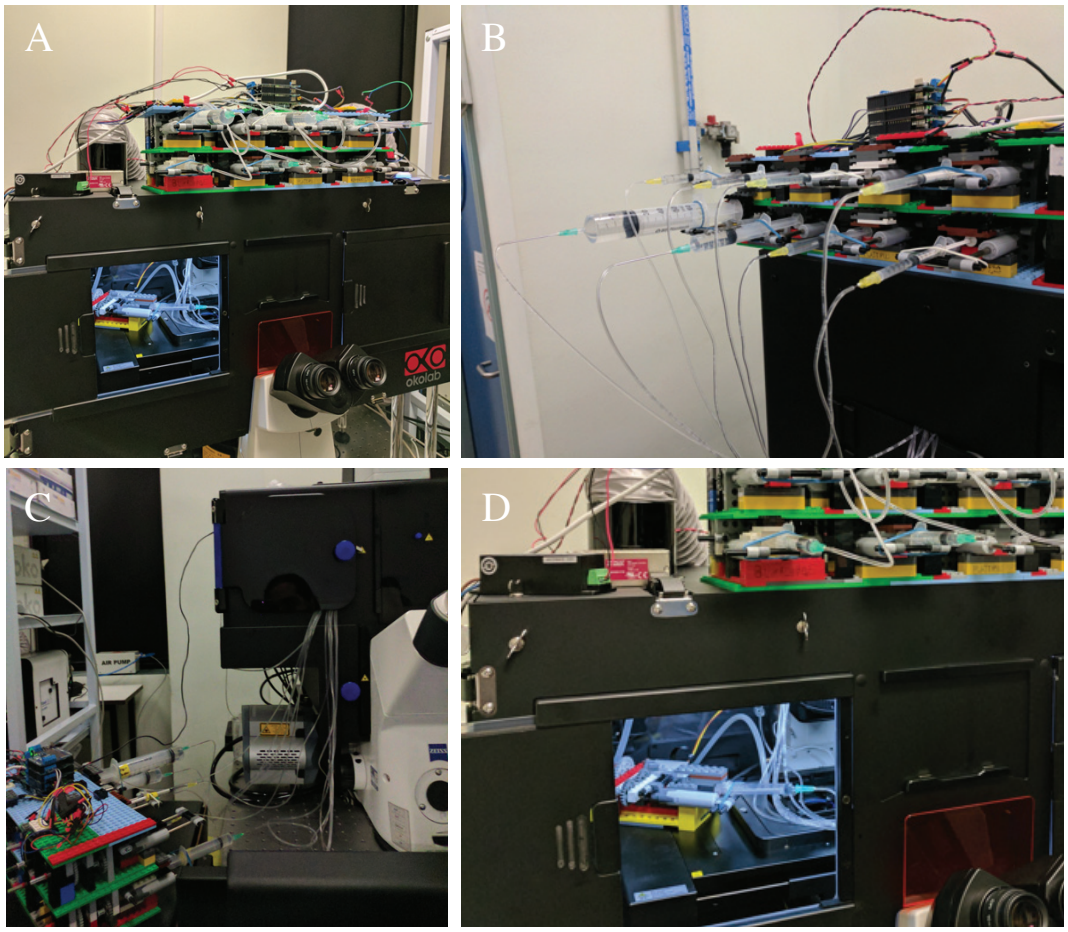

Figure 3.7: NanoJ-Optofluidics hardware is easily adapted to commercial systems. A,B - Pumps assembled on a Nikon NSTORM microscope with different sized syringes; C - Pumps assembled on a Zeiss Elyra PS.1; D - Single pump with syringe inside the incubator of a Nikon NSTORM microscope to equilibrate the liquid's temperature with the sample.

work. The simplicity of the underlying elements means that an entire 8 pump array can be assembled in a day, including the electronics. It is also light and compact enough that it can be easily mounted on most microscopes (figure 3.7). Single pumps (figure 3.7 D) in particular are small enough to be placed inside microscope enclosures, which allows whatever liquid is loaded on the syringe to be temperature equilibrated with the sample.

To control the motors from a computer, an Arduino firmware was created. Any software which can establish RS-232 communication to the Arduino can use the commands shown in listing 3.1 to control the pumps. This command scheme is designed to allow easy communication through a serial port. The Arduino con-

Listing 3.1: List of commands and command notation

```
g = get status of all pumps
a = stop all pumps
p = get number of pumps
axxy = stop pump xxy
sxxynnn = for pump xxy set speed nnn
rxxydttttt = Start pump xxy in direction d
                    for ttttt seconds

The commands use the notation:
d = 1 is forward, d = 2 is backwards
xx = shield address {Min: 01; Max: 32}
y = motor/pump address {Min: 1; Max: 4}
nnn = speed {Min: 000; Max: 255}
ttttt = duration {Min: 00001; Max: 99999}
\label{lst:commands}
```

troller automatically parses the commands and responds appropriately. While the command scheme is straightforward, it requires a piece of software on the computer to send the commands. For automated control, this software needs to know the commands scheme and, for sequential fluidic protocols, to be able to send them at appropriate time intervals. To integrate pump control with the Micro-manager microscope control software, a complete software package was developed in Java (figure 3.6 B). It can function either as a stand-alone application or as a Micro-Manager plugin and includes a plugin system, several programmatic interfaces, and a Graphical User Interface (GUI).

First, the software package was developed to be independent of the hardware control scheme. To achieve this, the command scheme for each pump type (for example, a commercial pump or the Arduino command scheme shown above) is wrapped as a plugin. When first run, the software automatically loads each available plugin and makes that particular pump type available for control. The software can create any number of new instances for each pump type. This allows the addition of several pumps and combining several different pump types. At the time of writing, plugins are available for the NanoJ LEGO syringe pumps, the NanoJ 3D printed pumps, a commercial syringe pump (Harvard Apparatus, Pump 11 Elite)

and a virtual pump for testing. To create a plugin for a new pump type, a programmer needs only to extend a `Pump` Java class. Each plugin defines how to initiate the connection to the pump, which makes the software package as a whole independent of any specific hardware. However, the package does provide access to MicroManager's serial connection capabilities, so little effort is needed to create a plugin for devices which communicate using the serial protocol. This is advantageous as the majority of scientific hardware uses the serial protocol for communication.

The programming interfaces also allow full control of any pump system. For example, `Pump` instances can be generated for any pump type and controlled directly. A `PumpManager` class manages connections to multiple pumps if more than one controller is used. A `Sequence` class is also available which allows a sequence of several `Step` instances to be created. Each `Step` defines what to do at a particular time point: which pump to use, how much volume to inject, and for how long to wait before the next step is triggered. The `SequenceManager`, once started, goes through a given `Sequence` and uses the `PumpManager` to initiate the instructions given in each `Step`. All of the above mentioned classes are available to control through the BeanShell scripting language of MicroManager, enabling complete and integrated automation of both microscope acquisition and microfluidic manipulation of the sample.

The GUI (figure 3.6 B) allows any researcher without programming experience to control the NanoJ-Optofluidics framework. First, the connection tab lists available serial ports and plugins, allowing a user to connect as many pump controllers as required. This is essentially a graphical method to instruct the `PumpManager` which pumps need connecting to. The second tab lists all currently connected pumps (from `PumpManager`), a list of known syringe types, and allows a user to instruct a pump to inject or withdraw a specified volume. The Sequential Protocol tab is where a user can design and start a `Sequence` of `Steps`. A list of `Steps` is presented where each individual element of the particular `Step` can be altered. Any number of `Steps` can be added to the `Sequence`. Each `Step` can be moved further up or down in the `Sequence`, can be deleted or duplicated through

the GUI. Importantly, the Sequential Protocol tab allows a withdrawal step to be defined. This means that, in between each `Step`, a specific pump is always run in the same manner. Usually this will be a pump whose task it is to withdraw the liquid from the sample. This withdrawal step thus enables liquid exchange to occur for every step. However, any individual `Step` can tell the `SequenceManager` to skip the withdrawal step. This means the step will only add liquid to the sample, instead of exchanging liquid. Applying drugs or fixatives to the medium of live cells can be achieved in this way. The tab can also save and load protocols to disk for later access. The GUI itself is also programatically accessible, which means that a user can connect to the pumps and design a protocol entirely in the GUI but use BeanShell scripts to control the `Sequence`. This simplifies integration with Micro-Manager since BeanShell scripts can also capture microscope acquisition settings from the Micro-Manager GUI. By having graphical methods to define a microscope acquisition and a microfluidic protocol, BeanShell scripts can be designed which are generic and independent of any specific microscope acquisition setting or sequential protocol.

3.2.2 Fluidic Device Design for Bulk Liquid Exchange *In-situ*

3.2.2.1 Channel-type Microfluidic Devices

As can be observed in figure 3.3, commercial microfluidic devices can be used with the NanoJ-Optofluidics framework. However, there are several disadvantages to this approach. First, commercial microfluidic devices are significantly more expensive than standard coverslips or cell culture dishes. Second, the inlets use Luer-lock inlets to connect to standard fluidic components which can result in accumulation of liquid in between rounds. This problem is clearly visible in figure 3.3, where blue liquid accumulates near the outlet. When performing an immuno-staining protocol this may result in cross-talk or increased background from antibodies and other solutions which have accumulated in the reservoirs and cause dilution during long incubation periods. Finally, the shape of the inlets introduces a significant dead volume ($60\mu L$ in the device in figure 3.3). As an alternative approach to commercial devices, a PDMS microfluidic device was designed for liquid exchange. PDMS

allows for designs with low dead volume and no reservoirs. As a first approach to address these issues, a simple PDMS device was designed consisting of a simple channel, $\approx 1mm$ wide and $10mm$ long and with a single inlet and outlet.

To use tubing with a small internal diameter and compatible with manifolds with a small dead-volume, silica capillaries were used. One issue with small internal diameters is that, for any reduction in internal diameter, the fluidic resistance of the tubing will increase non-linearly, following equation (3.3) (Beebe et al., 2002):

$$R = \frac{8\mu L}{\pi r^4} \tag{3.3}$$

Where R is the fluidic resistance, μ is the fluid viscosity, L is the tube length and r is the tube radius. Since, for the same applied pressure, the flow-rate is inversely proportional to the fluidic resistance (Beebe et al., 2002), this means that exponentially more pressure is required to achieve the same flow-rates. When using $100\mu m$ diameter silica capillaries (CM Scientific, TSP100794) the syringe fittings tended to explosively disengage due to the high pressures. However, $250\mu m$ internal diameter capillaries (CM Scientific, TSP250350) had little issue with internal pressure and 1 metre of this tubing results only in a $49\mu L$ dead volume, a ten-fold reduction compared to the tygon tubing generally used in microfluidics.

Figure 3.8 shows the types of connectors used to connect silica capillary tubing to microfluidic devices. To connect capillaries to the commercial microfluidic device shown in figure 3.3, Luer syringe injection ports are used. These consist of a simple Luer cap with a silicone plug (figure 3.8 A). The Luer cap allows the port to be adapted to the commercial microfluidic device and the silica capillary is pierced through the silicone plug, which is self-sealing. But the $250\mu m$ internal diameter capillary has a $360\mu m$ external diameter and the smallest hole that could be punched through the PDMS without it collapsing was $\approx 800\mu m$. To address this, any connection to a PDMS devices used a biocompatible polymer (PEEK) adapter tubing with an external diameter of $\approx 800\mu m$ and $360\mu m$ internal diameter (figure 3.8 D). The same type of PEEK tubing is used to adapt the silica capillaries to the syringe connector (figure 3.8 B and C) and the manifold (figure 3.8 E). This

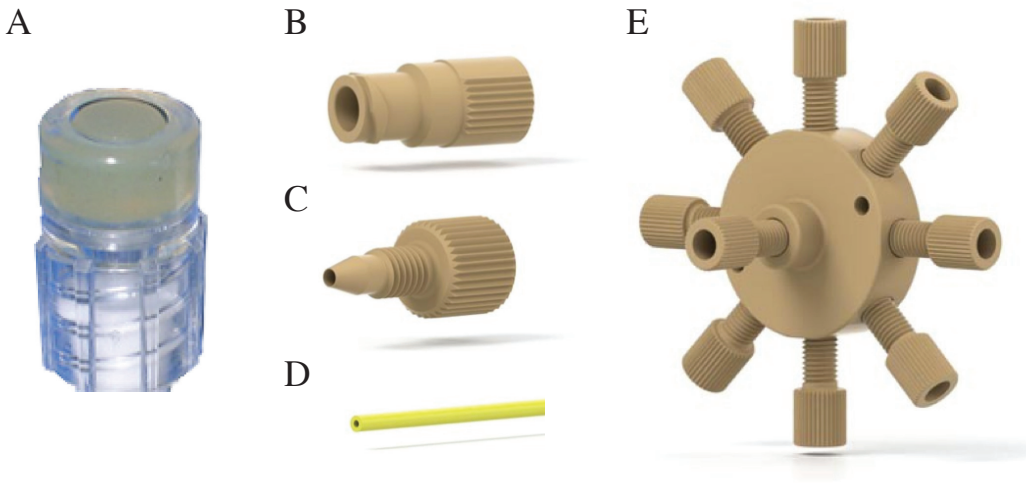

Figure 3.8: Types of fluidics connectors used with silica capillaries to enable low dead-volume connection to microfluidic devices. A - Luer syringe injection port (Mouldex, SB0067); B - Syringe Luer adapter (IDEX-HS, P-659) which connects to C - threaded cone adapter (IDEX-HS, F-120) for 1/16 inch diameter ($\approx 1.6mm$) tubing; D - Size adapter for the silica capillary made of a biocompatible polymer (PEEK; IDEX-HS, 1533); E - Manifold to connect up to 8 different input tubing to 1 output tubing (IDEX-HS, P-170).

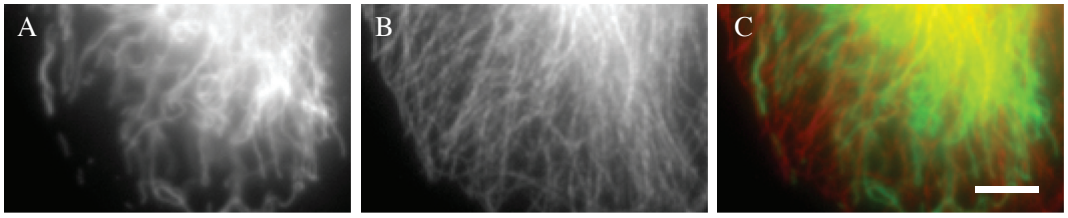

Figure 3.9: Widefield imaging of a secondary immuno-staining of CHO cells using NanoJ-Optofluidics and a PDMS straight-channel device. A - Vimentin abelled with Alexa Fluor 488; B - Microtubules labelled with Alexa Fluor 647; C - Overlay of A and B. Scale-bar: $5\mu m$.

manifold allows up to 8 input capillaries to merge into a single output capillary with a dead volume of only $2.2\mu L$.

By making use of the NanoJ-Optofluidics LEGO hardware and software package, the capillary tubing, the manifold and a straight channel PDMS device, automated fixation and immuno-staining of cells was achieved (figure 3.9). However, the use of a manifold introduced a problem. Any liquid being injected into the manifold will follow the path of least resistance. The fittings are screwed manually and apply a certain amount of pressure on the capillary, which can potentially slightly

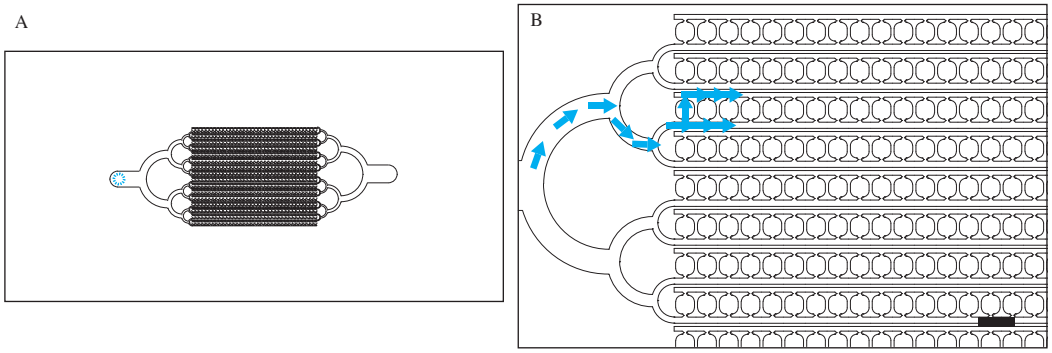

Figure 3.10: CAD designs for no-flow PDMS devices to be attached to 25x60mm coverslips. A - Overview of the no-flow design with the coverslip area outlined by a black box. The dotted blue ring marks the location where liquid is loaded. The liquid is split into 16 separate channels to increase the area covered by the device; Rectangle corresponds to 25x60mm area. B - Zoomed section of A. The blue arrows show one potential path for the liquid to follow. Scale-bar: $100\mu m$.

decrease the internal diameter and therefor increase the resistance in that particular tubing. The variability of the manual fitting sometimes caused the path of least resistance to be the path to another syringe. This meant that whatever syringe was currently injecting a liquid, would inject it into one (or more) other syringe/s instead of the PDMS device. This made the overall configuration with manifolds unreliable. Another issue arose from the use of PDMS devices with sequential labelling protocols (see section 4.2.1), where the pressure applied on the cells after using highly acidic solutions sometimes resulted in the cells being washed away (figure 4.2).

The most problematic aspect with microfluidics is the issue of air bubbles (Skelley et al., 2008). Any air which is introduced to the system will result in air bubbles which immediately destroy the cells when flowing through the channels. Some of the sequential labelling protocols (section 4.2.1) are especially prone to generating air bubbles. The many inputs of the manifold also increased the likelihood of introducing bubbles. Overall this made the straight channel PDMS design and manifold combination highly unreliable.

There are many microfluidic designs which address the issue of bubbles (for examples see Skelley et al. (2008), Kang et al. (2008) and Cambier et al. (2015)). Cambier et al. (2015) have recently described a simple design where fluid exchange of the cell's medium occurs through diffusion thereby addressing the issue

of bubbles. Given the simplicity of this so-called no-flow design, it served as the basis for a new PDMS device design (figure 3.10). The Cambier et al. (2015) design is based on the idea of asymmmetric flow. First, the device is filled with liquid in the areas marked with a blue ring in figure 3.10 A and the liquid is allowed to fill the remaining parts of the device. Figure 3.10 B shows a zoomed section of the device and the blue arrows show a potential path for the liquid to go through. When the liquid reaches the first channel, it is partially diverted to a small chamber and to a parallel channel on the top of the chamber. The design of the chip is such that liquid will preferentially travel through the parallel channels and not the chambers that punctuate the channel, which means liquid exchange with the small chambers happens only though diffusion; in the published design, a complete liquid exchange required at least 7 minutes. Any bubbles which are present in the system should also travel preferentially through the first and last chambers along the channel, which means the majority of the chambers in the middle of the device will experience no bubbles or flow. The adapted design used here (figure 3.10 A) also includes a large inlet area so each syringe pump has its own dedicated inlet, obviating the need for the manifold. While the device could be made successfully on a few occasions, the many small features in the design made it difficult to remove the PDMS from the mould without the features being destroyed. This means several attempts were required before a working device was achieved. Additionally, the loading of the device with liquid often failed to cover many of the chambers, meaning they were filled with air. This air could not be removed, making the device largely unusable.

3.2.2.2 Dish-based Microfluidic Device Design

Microfluidic flow-cell type devices are designed for applications where flow-rate, volume and concentration of solutions need to be controlled precisely. However, as has been mentioned, not all biological fluidic applications require great precision in these parameters. Traditional microfluidic devices are also usually designed to minimise dead volumes, requiring only of tens of μL's. However, such volume efficiency is not always required. The primary goals for the NanoJ-Optofluidics liquid exchange devices are ease of fabrication, high reproducibility,

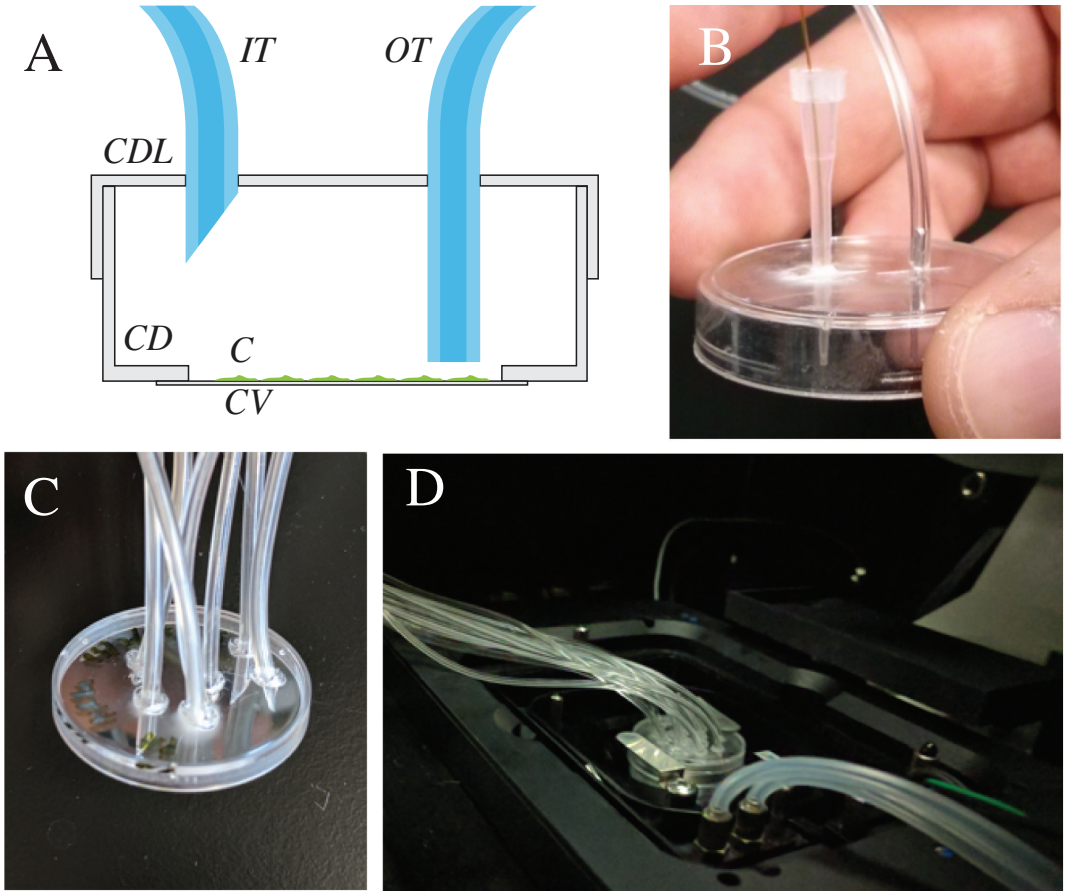

Figure 3.11: A - Schematic cross-section of the device. IT - Inlet tubing; OT - Outlet tubing; CDL - Cell culture Dish Lid; CD - Cell culture Dish; C - Cells; CV - Coverslip; B - Photograph of a lid with adapters for capillaries and silicone tubing; C - Photograph of a lid with tubing threaded through; D - Dish-based device mounted on the stage of a Zeiss Elyra PS.1.

high reliability and straightforward automation. So far, the PDMS devices described here have failed to meet either of these standards.

To address this, instead of a flow-cell type device, a fluidic device can be made from standard glass-bottom cell culture dishes (figure 3.11 A; Ibidi, 81158). While these are fluidic but not strictly *micro*-fluidic devices, volumes of $\approx 100\mu L$ are still sufficient to cover the imaging area of a cell culture dish. One particular advantage of commercial cell culture dishes is the fact most microscope stages are designed with these types of dish in mind. Therefore, a dish-based device requires no modification for use with any microscope (figure 3.11 D). These commercial dishes are also designed to be compatible with cell culture and high-resolution fluorescence

imaging. However, they are not designed with fluidic liquid exchange in mind. To address this, inlets and an outlet holes are made through the lid, allowing tubing to reach the cells (figure 3.11 A). Tubing is threaded through the inlets and outlet holes. The inlets are kept at the level of the lid to prevent any liquid from diffusing to the sample before it is required. The outlet tubing is kept at the level of the cells to allow most liquid to be removed. It should be noted that removal is never total with this approach as a thin film of liquid tends to remain in the dish regardless of how long the removal pump operates. For most of the applications this system was designed for (such as fixation and immuno-staining) this is not an issue as either the sample will be washed several times before introducing a new liquid, or the added liquid (i.e. fixative) will not dilute significantly to affect effectiveness. Nevertheless, this design solves any problem from bubbles in the tubing, as any air in the form of bubbles will stay at the top of the device while any liquid drops down to the imaging area.

To make the holes, a few techniques were initially attempted. Using hole punches or drilling holes in the plastic tended to crack and often destroyed the lids. Figure 3.11 B shows an early drilled lid design with a visible crack. These early designs also involved the use of pipette tips to serve as adapters to thread through capillary tubing and metal adapters to adapt large internal diameter tubing to the holes and both are visible in figure 3.11 B. To overcome the cracking issue and make holes large enough that adapters are not required, a heated needle technique was developed. A syringe needle is heated on a Bunsen burner and is then used to pierce through the plastic, thereby creating a hole. Because the plastic melted during the piercing, cracking does not occur. To create a hole with the correct diameter for tubing to be threaded through (figure 3.11 C), a needle can be chosen with a diameter which matches the outer diameter of the tubing. Otherwise, a smaller needle can be used and, during the piercing process, the needle can be displaced in a circular motion around the hole, thereby increasing the diameter of the hole. Figure 3.11 C shows a lid where holes were made using this technique as well as several Tygon tubes threaded through.

With a PDMS device, a manifold is preferred to avoid complex, multi-inlet designs or designs with large reservoir areas to allow multiple inlets. However, the through-hole approach and the larger area of the lid allows for a large number of tubing to be connected to the dish with arbitrary internal and external diameters. This obviates the need for a manifold and allows the use of flexible tubing with large external diameters but small internal diameters. Given this, Tygon tubing with an internal diameter of $190\mu m$ and an external diameter of $1.99mm$ (Cole Parmer, WZ-06460-10) was used, resulting in a dead-volume of less than $30\mu L$ for each metre of tubing. To connect flexible tubing to the syringes, syringe needles can be used which have an external diameter matching the tubing's internal diameter. This needle approach was not possible with silica capillaries as the hardness and weight of the capillaries tended to bend small diameter needles, therefore requiring the adapters shown in figure 3.8 B-D.

One consideration for syringes with large volumes, is the resulting increase in torque required to inject. This is because of the greater the ratio of the internal diameter of the syringe to the internal diameter of the tubing, the greater the volume that needs to be displaced for the same displacement of the linear actuators. For syringes with a nominal volume greater than $5mL$, the LEGO pumps could not inject liquid through the $190\mu m$ internal diameter without the syringe explosively disassembling the pump. For these larger volume syringes, tubing with an internal diameter of $760\mu m$ (Cole Parmer, WZ-06460-24) was used. This tubing has a dead volume of less than $500\mu L$ per metre of tubing, but when using such large volume syringes, the dead-volume matters less as these are used for washing solutions and other non-expensive reagents.

In the dish-based design, liquid can be injected using syringe pumps in the same manner as with flow-cell devices. However, liquid removal requires a separate pump. Liquid removal should be performed at faster pump flow-rates in a dish-based device because the cross-section of the liquid on the dish is significantly larger than the cross-section of a flow-cell. This means the same pump flow-rate will move liquid at a slower rate through the dish, for a given syringe. Therefore, li-

quid removal with the dish-based design is performed with a fast and cost-effective peristaltic pump (Adafruit, 1150). This pump has a rated flow-rate of $1666\mu L/s$ and is factory fitted with silicone tubing with an internal diameter of $\approx 2mm$. To connect the peristaltic pump to the dish, Tygon tubing with an external diameter of $2.46mm$ and an internal diameter of $760\mu m$ (Cole Parmer, WZ-06460-24) was used. The Tygon tubing slides into the pump tubing directly, and since it has an outer diameter larger than the internal diameter of the pump tubing, it creates a seal that allows it to fix firmly in place. The difference in the internal diameters of both tubing also leads to a $\approx 6.5x$ reduction in pumping speed, resulting in a flow-rate of $\approx 267\mu L/s$. Considering the cell culture dish can hold a maximum of $4mL$ of liquid and most experiments use a maximum of $2mL$ of liquid (i.e. during wash steps), this still means the whole dish can be cleared of liquid in 7 to 14 seconds.

The dish-based design, choice of tubing and syringes correspond to the wetware element of the framework. By combining these elements, the NanoJ-Optofluidics framework was used successfully to perform automated immuno-staining of cells (figure 3.12). Briefly, cells were grown on a cell culture dish and manually fixed. Syringes loaded with the different components required for an immuno-staining were mounted on a LEGO pump array and a staining protocol was designed with the NanoJ-Optofluidics software. After the software went through the entire procedure, the cells were imaged on a widefield microscope and a correct immuno-staining was observed (figure 3.12). The staining was uniform throughout the entire dish, and was qualitatively similar to the one obtained for NanoJ and straight microfluidic channels.

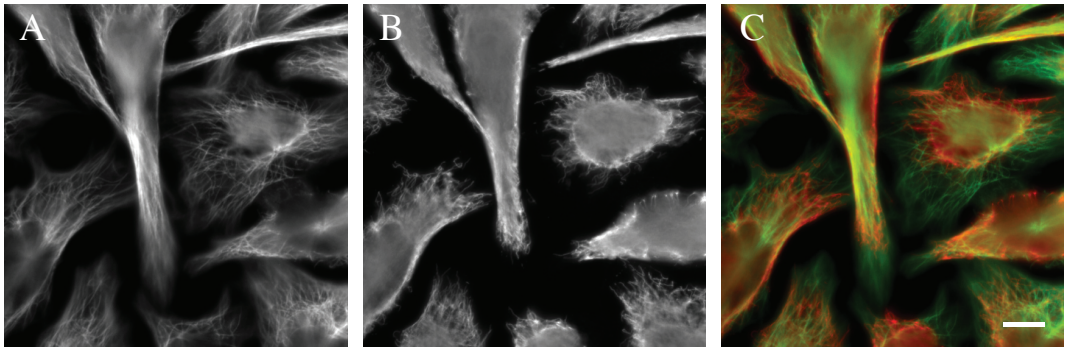

Figure 3.12: Widefield imaging of a HeLa cells immuno-labelled using NanoJ-Optofluidics and a dish-based design. A - Microtubules labelled with Alexa Fluor 488; B - Vimentin labelled with Alexa Fluor 647; C - Overlay of A and B. Scale-bar: $10\mu m$.

3.3 Discussion

3.3.1 Dish-based Devices

The dish-based devices are simple, inexpensive and have functioned consistently well. Their geometry means fluid exchange can probably be accelerated. Given how the liquid is distributed at the bottom of the dish, the flow-rate observed at the cell height is not necessarily the same as the flow-rate at other heights of the liquid column. When imaging living cells, determining the actual flow-rate they experience is important, as this will determine what shear stress is exherted on them. Shear stress is the stress resulting from liquid flowing around the cells and can be determinant of cell fate and modulate cellular behaviour (Cambier et al., 2015; Polacheck et al., 2013). To determine the flow-rate experienced by the cells beads could be injected and removed while imaging their movement near the cell surface. Imaging at different heights would also allow the overall flow profile of the dish to be determined, and the maximum flow-rates for the device could be estimated. Alternatively, the flow-rate limits of liquid exchange could be tested empirically for both live and fixed cells by injecting and removing liquid at different pump flow-rates while imaging. In this case, observed cell structure and viability could serve as qualitative measures of acceptable flow-rates. Having determined the flow-rate limits, this means liquid can potentially be removed at greater speeds than is currently done, enabling greater temporal resolution for any liquid exchange experiment.

3.3.2 NanoJ Pumps

The small size of the LEGO pumps enables them to be placed inside a microscope's incubator. For SMLM in particular, this can be beneficial. If solutions are added to a sample at a temperature which is different to that of the microscope, then there is a change that sample drift can be exacerbated. By being able to add solutions at a temperature which matches the microscope, issues with drift can potentially be reduced.

The gear-ratio of the LEGO pumps was sufficient for the systems tested, but the flexibility of the LEGO design should allow for further optimisation. For example,

if the flow-rates of the dish-based flow-cell can be increased when compared to the PDMS devices, then the LEGO pump design may be altered to have a lower gear ratio, thereby increasing speed. However, the concomitant reduction in torque would have to be tested for different syringe and tubing internal diameters. It is possible different pump designs may be created for different syringe volumes, tubing diameters and flow-rates, as desired. The current linear actuators also limit the total volume that can be used in a given syringe (table 3.1). Different methods to press on the plunger may have to be considered if larger syringe volumes are required.

The pumps have also yet to be fully characterised. The reproducibility, accuracy and precision of the pumps with different syringe volumes should be measured in a systematic manner. Importantly, due to the nature of the LEGO design, inter-pump variability should also be determined. While little deviation has been observed for experiments involving liquid exchange, knowing these parameters would allow the LEGO pumps to be used for more stringent applications. For example, PDMS devices still offer applications that are not possible with the dish-based designs and operating pumps with PDMS devices requires precise control of flow-rates and pressure.

The 3D printed pumps would perhaps offer much more precise control of flow-rates and volumes but require further refinement. There are many parts of the pump which are not printed: the supporting rods (and bearings); the lead screw; the screw nut and the adapters for the pump and lead screw. The choice of all of these parts requires optimisation as some are larger than expected or do not fit together as expected. The current 3D printed mount is also not long enough for $20mL$ and $50mL$ syringes and requires redesigning. Finally, the plunger holder as originally designed (Negrier, 2015), fits only $10mL$ syringes. To be able to hold syringes ranging from $1mL$ to $50mL$, the holder also requires a redesign. The electronic control of stepper motors is complex and the current plugin is a work in progress since the stepper motors have been observed to stall frequently during testing. The cost of these devices could be up to 4-fold higher than that of a LEGO pump. This is still an order of magnitude cheaper than a commercial syringe pump, and if fully optimized, this

could make 3D printed pumps highly attractive to current researchers who require absolute fluid control precision in PDMS microfluidics. Nonetheless, these pumps require access to a 3D printer and are not easily repaired or modified. Assembling LEGO pumps requires no special equipment, are less expensive, are easily repaired and modified, and their design can potentially be improved to address many of the same applications 3D printed pumps can.

3.3.3 Software

The NanoJ-Optofluidics software can control different microfluidics hardware and can be programmatically integrated with the microscope acquisition. If this integration could be extended to a unified graphical user interface, the software package could have applications beyond the scope of the framework itself. However, currently, the software package can only accommodate syringe pumps and not other types of devices. Further development will correct for this and allow many different types of devices. For example, the peristaltic pump is not accounted for properly in the software, as it does not require a syringe and the expected flow-rates are different. Pressure pump systems could also be added to the software package, as these are commonly used with microfluidics. The `Pump` class underlying the current software model allows for this abstraction since it is independent of pump behaviour and it creating different pump subtypes from this class has been found to be straightforward (i.e. the commercial Harvard Apparatus syringe pump). Other devices such as valves and path selectors would allow complex fluidics layouts to be controlled in one simple graphical user interface. For complex steps where, aside from the pump action, valves and path selectors also need to be set, the different configurations could be defined as a new `FluidPath`. The user interface will have a new tab where combinations of different hardware could be created as new `FluidPaths`. Each `Step` in the `Sequence` would have a single `FluidPath` associated with it, and at the appropriate time in the protocol, would update all of the individual component accordingly. This type of software abstraction and user interface will circumvent researchers having to write scripts which need to take into account many separate control schemes for different device types. These kinds of

scripts tend to be uni-functional and are usually not easily translated to different applications, whereas the software design outlined here would be a generic approach and immediately functional for most researchers.

The integration with Micro-Manager is also under development, as it currently requires scripts to be able to integrate microfluidic protocols with acquisition. Micro-Manager includes a GUI for complex microscope acquisitions and these protocols can be controlled programmatically. To address integration of the microfluidics software with Micro-manager, a new plugin will be developed with a GUI to control a sequence of steps, where each step would consist of a microfluidic protocol, or a microscope acquisition or even both simultaneously. In this way, users of the software would not need to know any programming language, further broadening the availability of the framework.

3.3.4 Conclusions

It is the overarching goal of the NanoJ-Optofluidics framework to lower the barrier for biological researchers to perform fluidic exchange experiments while simultaneously imaging. Here, the feasibility of the approach has been demonstrated by performing an immuno-staining outside a microscope but chapter 4 will demonstrate further uses of the system where both imaging and fluidics are leveraged. The entire process can also be done at a cost which is an order of magnitude lower than what would be required for a commercial pump system and PDMS devices. The NanoJ-Optofluidics framework consists of three components: hardware, software and wet-ware. All three have been designed to enable researchers to assemble their own systems and be ready for imaging in a short period of time. Assembling a 12 pump array, electronic components and imaging chambers requires a maximum of a day. This includes testing the pumps for issues during assembly and testing injection with syringes. Planning and mounting the fluidic layout requires less than 2 hours, depending on experience. With PDMS devices, designing, obtaining a high-resolution photo-mask, making a mould, making the device and troubleshooting can take from several days to several weeks depending on suppliers, materials and equipment availability. Since optimisation will be required in the

above steps (PDMS device design, making the mould and fabrication), the process can be extended to several months before an experiment can be started. Once a design and mould have been optimised, PDMS devices take at least half a day to make and the fluidic connections can be prone to fail. The entire fluidic assembly of the tubing also requires great care and optimisation to prevent bubbles. With the dish-based design, air bubbles are not an issue and once a lid with inlets has been made, it can be reused. When combined with the hardware and software elements of the framework, these elements make NanoJ-Optofluidics an easily accessible platform for researchers to begin performing fluidics experiments.

3.4 Attribution

The wafer moulds for the PDMS devices were fabricated by Anna Bove and Jessica Davies, of the Guillaume Charras lab. The parts for the 3D printed pump were kindly printed by Ravi Desai of the Making Lab, Francis Crick Institute. The 3D design of the printed pumps was largely based on designs created by Negrier (2015).

3.5 Methods

3.5.1 Fluidic Device Fabrication and Intubation

To make PDMS flow-cell devices, first, a mould design was drawn using AutoCAD 2014. The designs were printed on an emulsion film as a high-resolution photomask by JD Photo-tools. Using the masks, moulds were fabricated as published elsewhere (Artemenko et al., 2011) with a height of $10\mu m$. PDMS was obtained as a kit (Dow Corning, Sylgard 184). PMDS elastomer was mixed with curing agent in a ratio of 10:1 and poured onto the mould. After curing at 60°C, the device was peeled off from the mould. $0.8mm$ holes were punched to interface with an inlet and outlet. PDMS and glass surfaces were activated using air plasma (30 seconds, 50 W, 0.3-0.4 mBar) before both were bonded together. To connect Tygon tubing to the devices, 21G syringe needles (VWR, 613-2023) had their beveled ends cut and were then inserted in the punched holes. To connect the silica capilaries, these were first threaded through PEEK tubing (IDEX-HS, 1533), and both were inserted together in the punched holes. A manifold (IDEX-HS, P-170) was used to connect multiple capillaries the PDMS device when warranted. Capillaries were adapted to the manifold using a threaded cone adapter (IDEX-HS, F-120) in conjunction a PEEK adapter (IDEX-HS, 1533). A Luer adapter (IDEX-HS, P-659) was used to adapt capilaries to syringes, in conjunction with a threaded cone adapter (IDEX-HS, F-120) and a PEEK adapter (IDEX-HS, 1533).

To adapt capilaries to a commercial flow-cell device (Ibidi, 80606), a Luer syringe injection port (Mouldex, SB0067) was used. Since the capilaries could not pierce through the silicone membrane, the capilaries were first threaded through the inside of a 21G needle. This needle was used to pierce the silicone membrane, and as the needle was removed from the membrane, the capilarie was left behind and the silicone membrane formed a tight seal with the capilary.

When loading syringes, at the beginning of the measurements, the syringe plunger sometimes caught on the walls of the body, resulting in delayed pump action. In these cases, the mean recovered volume was lower than expected. For a

$\approx 100\mu L$ nominal injection volume, $\approx 86\mu L$ were recovered versus the $\approx 98.4\mu L$ achieved elsewhere. However, the syringe plunger performs consistently after the issue first occurs and these values were discarded as outliers. The problem can be mitigated by moving the syringe plunger up and down the body repeatedly before any liquid is loaded.

3.5.2 Cell Culture and Immuno-staining

Cell culture was performed as described in section 2.4.1 with the exception of PDMS device seeding and the following antibodies were also use: Rabbit anti-Vimentin, 1/250 (Abcam, ab92547); Goat anti-mouse labelled with Alexa Fluor 488 1/200 (Thermo Fisher, A11029); Goat anti-rabbit labelled with Alexa Fluor 647 1/200 (Thermo Fisher, A27040); Goat anti-rabbit labelled with Alexa Fluor 488 1/200 (Thermo Fisher, A-11008).

Prior to seeding in PDMS devices, cells were concentrated by trypsinizing as before, centrifuging at a 1500 relative centrifugal force for 5 minutes, removing the supernatant and resuspending in $1mL$ of medium. The concentrated cell solution was seeded on PDMS devices by manually injecting the device and, after the entire solution flowed through, the cells were allowed to grow overnight prior to imaging. Immuno-stainings were performed as in section 2.4.2, except the staining was carried out using the NanoJ-Optofluidics system. Cells in figure 3.9 were imaged on a Zeiss Elyra PS.1 microscope, with a 100x TIRF objective and an Andor iXon897 camera. Cells in figure 3.12 were imaged in a Leica DMi8 widefield microscope using a 63x 1.25NA PL FLUOTAR objective and a Leica DFC365 FX camera.

3.5.3 Software Development

Software development was performed as described in section 2.4.4.

3.6 Bibliography

Adafruit Motor Shield V2 for Arduino. URL: https://learn.adafruit.com/adafruit-motor-shield-v2-for-arduino/overview (visited on 29/10/2015).

Allain, Rhett. 'Why Are LEGO Sets Expensive?' In: *Wired* (Oct. 2013).

Arduino. *Arduino - Home*. URL: https://www.arduino.cc/ (visited on 21/08/2017).

Artemenko, Yulia, Kristen F. Swaney and Peter N. Devreotes. *Cell Migration*. Vol. 769. 2011, pp. 287–309. ISBN: 9781617792069. DOI: 10.1007/978-1-61779-207-6_20.

Beebe, David J., Glennys A. Mensing and Glenn M. Walker. 'Physics and Applications of Microfluidics in Biology'. In: *Annual Review of Biomedical Engineering* 4.1 (Aug. 2002), pp. 261–286. ISSN: 1523-9829. DOI: 10.1146/annurev.bioeng.4.112601.125916.

Bell, Laurence et al. 'A Microfluidic Device for the Hydrodynamic Immobilisation of Living Fission Yeast Cells for Super-Resolution Imaging'. In: *Sensors and Actuators B: Chemical* (Oct. 2013). ISSN: 09254005. DOI: 10.1016/j.snb.2013.10.002.

Bhatia, Sangeeta N and Donald E Ingber. 'Microfluidic organs-on-chips'. In: *Nat Biotech* 32.8 (2014), pp. 760–772. ISSN: 1087-0156. DOI: 10.1038/nbt.2989[doi]. arXiv: 1408.1149.

Breu, FX, S Guggenbichler and JC Wollmann. *Immunocytochemical Methods and Protocols*. Ed. by Constance Oliver and Maria Célia Jamur. Vol. 588. Methods in Molecular Biology. Totowa, NJ: Humana Press, 2010. ISBN: 978-1-58829-463-0. DOI: 10.1007/978-1-59745-324-0.

Burridge, Keith and Magdalena Chrzanowska-Wodnicka. 'Focal Adhesions, Contractility, and Signaling'. In: *Annu. Rev. Cell Dev. Biol* 12 (1996), pp. 463–519. ISSN: 1081-0706. DOI: 10.1146/annurev.cellbio.12.1.463.

Cambier, Théo et al. 'Design of a 2D no-flow chamber to monitor hematopoietic stem cells.' In: *Lab on a chip* 15.1 (Jan. 2015), pp. 77–85. ISSN: 1473-0189. DOI: 10.1039/c4lc00807c.

Center for Open Science. *OSF | Home*. 2017. URL: https://osf.io/ (visited on 06/09/2017).

Chován, Tibor and András Guttman. 'Microfabricated devices in biotechnology and biochemical processing'. In: *Trends in Biotechnology* 20.3 (Mar. 2002), pp. 116–122. ISSN: 01677799. DOI: 10.1016/S0167-7799(02)01905-4.

Duffy, David C. et al. 'Rapid prototyping of microfluidic systems in poly(dimethylsiloxane)'. In: *Analytical Chemistry* 70.23 (1998), pp. 4974–4984. ISSN: 00032700. DOI: 10.1021/ac980656z. arXiv: 1106.3015.

Duncombe, Todd A., Augusto M. Tentori and Amy E. Herr. 'Microfluidics: reframing biological enquiry.' In: *Nature reviews. Molecular cell biology* 16.9 (Sept. 2015), pp. 554–67. ISSN: 1471-0080. DOI: 10.1038/nrm4041.

Kang, Joo H, Yu Chang Kim and Je-Kyun Park. 'Analysis of pressure-driven air bubble elimination in a microfluidic device.' In: *Lab on a chip* 8.1 (2008), pp. 176–178. ISSN: 1473-0197. DOI: 10.1039/b712672g.

Negrier, Aldric. *3D Printed Syringe Pump Rack: 29 Steps (with Pictures)*. 2015. URL: http://www.instructables.com/id/3D-Printed-Syringe-Pump-Rack/ (visited on 09/09/2017).

Parsons, J. Thomas, Alan Rick Horwitz and Martin A. Schwartz. 'Cell adhesion: integrating cytoskeletal dynamics and cellular tension'. In: *Nature Reviews Molecular Cell Biology* 11.9 (2010), pp. 633–643. ISSN: 1471-0072. DOI: 10.1038/nrm2957. arXiv: NIHMS150003.

Polacheck, William J et al. 'Microfluidic platforms for mechanobiology.' In: *Lab on a chip* 13.12 (2013), pp. 2252–67. ISSN: 1473-0189. DOI: 10.1039/c3lc41393d. arXiv: NIHMS150003.

Reece, Amy et al. 'Microfluidic techniques for high throughput single cell analysis.' In: *Current opinion in biotechnology* 40 (2016), pp. 90–96. ISSN: 1879-0429. DOI: 10.1016/j.copbio.2016.02.015.

Rosner, Margit, Katharina Schipany and Markus Hengstschläger. 'Merging high-quality biochemical fractionation with a refined flow cytometry approach to monitor nucleocytoplasmic protein expression throughout the unperturbed mammalian cell cycle.' In: *Nature protocols* 8.3 (Mar. 2013), pp. 602–26. ISSN: 1750-2799. DOI: 10.1038/nprot.2013.011.

Sackmann, Eric K, Anna L Fulton and David J Beebe. 'The present and future role of microfluidics in biomedical research.' In: *Nature* 507.7491 (2014), pp. 181–9. ISSN: 1476-4687. DOI: 10.1038/nature13118.

Skelley, Alison M and Joel Voldman. 'An active bubble trap and debubbler for microfluidic systems.' In: *Lab on a chip* 8.10 (2008), pp. 1733–1737. ISSN: 1473-0197. DOI: 10.1039/b807037g.

Tam, Johnny et al. 'A Microfluidic Platform for Correlative Live-Cell and Super-Resolution Microscopy'. In: *PLoS ONE* 9.12 (2014), e115512. ISSN: 1932-6203. DOI: 10.1371/journal.pone.0115512.

The LEGO Group. *Company Profile - The LEGO Group - About Us LEGO.com*. 2014. URL: https://www.lego.com/en-gb/aboutus/lego-group/company-profile (visited on 02/09/2017).

Zhou, Ying et al. 'A microfluidic platform for trapping, releasing and super-resolution imaging of single cells'. In: *Sensors and Actuators, B: Chemical* 232 (2016), pp. 680–691. ISSN: 09254005. DOI: 10.1016/j.snb.2016.03.131.

Chapter 4

Online Fixation and Sequential Labelling for High-Throughput Super-Resolution

4.1 Introduction

4.1.1 Sequential Labelling *In-situ*

An antibody's affinity to its antigen depends on many intrinsic and extrinsic properties such as its secondary structure, temperature and pH (Reverberi et al., 2007). Researchers can harness all of these properties to try and dissociate an antibody from its antigen. The temperature can be raised by placing the sample on a heating plate (Micheva et al., 2007), or even by microwaving it (Kolodziejczyk et al., 1986). A sample's pH can be altered by using highly basic or acidic solutions. Chaotropic agents, molecules which affect hydrogen bonds, can also be used to attack the binding of the antibody directly (Reverberi et al., 2007). In microscopy, early antibody elution techniques attempted to dissociate antibodies from tissue sections by using highly acidic solutions (pH 1.8-2.2), sometimes in conjunction with moderately denaturing conditions (Nakane, 1968; Vandesande et al., 1975; Vandesande et al., 1976; Tramu et al., 1978). Heating samples at up to 130°C has also been used to perform triple stainings (Kolodziejczyk et al., 1986). These early protocols tended to be unreliable and to not elute all antibodies, especially if

these were of high-affinity (Vandesande et al., 1976; Gendusa et al., 2014). Many other techniques have been tested and developed since these first protocols, using low pH (Micheva et al., 2007; Pirici et al., 2009), chemical denaturing (Pirici et al., 2009; Gendusa et al., 2014; Murray et al., 2015; Bolognesi et al., 2017), chaotropic agents (Pirici et al., 2009; Bolognesi et al., 2017), or combinations of these elements (Wählby et al., 2002; Pirici et al., 2009). One thing in common with all of these techniques is that they were developed with tissue sections in mind and all of them involve manual handling and heating the sample to temperatures above 50°C. This kind of heating can not be performed *in-situ*, with the sample on the microscope, as it would damage the microscope equipment. This may explain why none of these techniques have been adapted to a fully automated, high-throughput, *in-situ* labelling system.

More recently, there have been attempts to develop antibody removal protocols on cells grown on coverslips, and at room temperature. Lin, Fallahi Sichani and Sorger (2015) developed a method using proteases (papain, pepsin or trypsin) to digest the antibodies from the sample, but this required careful optimisation as each antibody and sample reacted differently to different proteases. Unfortunately, they disavowed their own protease approach the following year, indicating the tendency to destroy the sample (Lin, Fallahi Sichani, J.-y. Chen et al., 2016). Yi et al. (2016) have developed a technique of antibody elution for dSTORM imaging called madSTORM (multiplexed antibody size-limited dSTORM). Reasoning that low pH may negatively impact cell morphology, they tested different mild chemical denaturing and chaotropic methods with pH's ranging from 4.0 to 6.0. They report using a chaotropic agent ($3.5M$ $MgCl_2$) with mild detergent (0.1% Tween-20) was the most successful protocol to remove Alexa FLuor 647 directly labelled primary antibodies. However, they do not achieve complete removal of Alexa Fluor 647 signal. The whole signal must be removed or the images acquired in the next step in the sequence may partially include the previous signal. Even if the signal simply appears as diffuse background, this may reduce the quality of the reconstruction as SMLM is highly sensitive to any background signal. To address this, Yi et al. (2016)

combine the elution method with bleaching using the microscope illumination. By using directly labelled primary antibodies, they achieved sequential labelling of up to 25 epitopes on T-cells. Nonetheless, this method was performed manually.

In contrast to antibody removal protocols, bleaching based protocols have, however, been adapted to fully automated *in-situ* systems (Gerdes et al., 2013; Schubert et al., 2006). By using commercially available and fully validated directly labelled primary antibodies, these systems have been demonstrated to achieve up to 100 labelling rounds. Three major methods to bleach fluorescence have been used: using microscope illumination (Schubert et al., 2006; Nanguneri et al., 2012); a basic hydrogen peroxide solution (Gerdes et al., 2013; Lin, Fallahi Sichani and Sorger, 2015; Lin, Fallahi Sichani, J.-y. Chen et al., 2016); sodium borohydride (Tam et al., 2014) or a combination of sodium borohydride and microscope illumination (Valley et al., 2015). Most prior work has focused on widefield or confocal imaging of tissue sections. Lin, Fallahi Sichani and Sorger (2015) have extended the hydrogen peroxide method to single cells and, interestingly, when testing the bleaching rate of different fluorophores, they found Alexa Fluor 647 to bleach the most effectively. However, they found 1 hour is required to fully bleach all forms of fluorescent dyes. Tam et al. (2014) and Valley et al. (2015) extended the bleaching concept to dSTORM and focus on sequential imaging steps that use only Alexa Fluor 647, as it is the best performing dSTORM dye (Dempsey et al., 2011). Both works demonstrate multi-colour dSTORM imaging by bleaching Alexa Fluor 647 in between imaging and staining cycles. Their method uses 0.1% sodium borohydride for a period of 10 minutes, which can be useful for high-throughput super-resolution imaging as any reduction in processing time results in an increase in throughput. Valley et al. (2015) also measure the efficiency of sodium borohydride to fully remove fluorescence in SMLM and determined an additional laser illumination bleaching step is required to achieve full removal. With an automated *in-situ* system, this would be straightforward to implement and could be done simultaneously with the sodium borohydride incubation.

In addition to eluting or bleaching standard antibodies, probe exchange tech-

niques have recently been developed which enable highly multiplexed super-resolution imaging (Jungmann, Avendaño et al., 2014; Kiuchi et al., 2015; Agasti et al., 2017). These techniques are largely based on the points accumulation for imaging in nanoscale topography (PAINT) method (Sharonov et al., 2006). In PAINT, the sample media contains a dye which binds to a target of interest. Whenever a dye-molecule attaches to its target, it will either attach transiently and then diffuse away, or it will be bleach after a period of time. If the dye concentration is sufficiently low, these events will be registered as a single molecule events, enabling SMLM imaging. Sharonov et al. (2006) demonstrated PAINT by imaging a membrane dye, Nile Red, binding in supported membrane bilayers and Giannone et al. (2010) extended the concept by imaging ligands transiently binding specific membrane molecules. One incarnation of the concept, the Binding-activated localisation microscopy (BALM) method, has been developed to image deoxyribonucleic acid (DNA) by using DNA-binding dyes (Schoen et al., 2011) such as YOYO-1. To study DNA origami (DNA nano-structures which have been engineered to adopt a specific shape) Jungmann, Steinhauer et al. (2010) modified the PAINT concept to perform SMLM imaging of DNA origami by using short ($\approx$10 base pairs) single-stranded DNA (imaging strands) which transiently complement target strands on a DNA origami. This technique, termed DNA-PAINT, was then extended to biological imaging by modifying antibodies with the complementary (target) strand (Jungmann, Avendaño et al., 2014). While there has been prior work using erasable complex DNA-antibody conjugates to enable multiplexing (Schweller et al., 2012), DNA-PAINT simplified the antibody labelling scheme while enabling SMLM imaging. DNA-PAINT does not require strong laser illumination, a buffer whose effectiveness degrades over time or SMLM specific fluorophores. Importantly, bleaching of the sample is not an issue with DNA-PAINT because there is a practically infinite source of replacement imaging strands. DNA-PAINT also allows imaging over arbitrarily long time periods, enabling higher SMLM localisation densities and therefore, higher resolution (Legant et al., 2016). One drawback is the fact there are multiple DNA strands in solution during imaging, meaning the entire sample

has a constant background of dye which has to be rejected by some method like TIRF (Schnitzbauer et al., 2017). An alternative method uses Förster Resonance Energy Transfer (FRET), where the fluorescence signal observed is a result of dyes in the imaging strands coming into close contact with the target strands, enabling background-free DNA-PAINT imaging (Auer et al., 2017).

DNA-PAINT also enables straightforward multiplexed SMLM imaging. A sample can be labelled with multiple antibodies, each with a unique target DNA strand. To image antibody A, the sample is immersed in imaging strands which complement the target strands on A. The sample is imaged and the imaging strands are washed away. A new imaging strand can then be added for antibody B, followed by imaging. These cycles of washing and imaging can be repeated for as many targets as required, and it is called the Exchange-PAINT method (Jungmann, Avendaño et al., 2014; Agasti et al., 2017). This type of probe exchange sequential imaging has the advantage that, when compared to the previously mentioned sequential labelling techniques, only one staining step is necessary and the probe exchange step requires only 10 to 20 minutes of washing (Schnitzbauer et al., 2017). On the other hand, the constant diffusion of background molecules also implies exposure times lasting hundreds of milliseconds are often preferred to minimize spurious detections (Schnitzbauer et al., 2017). Such long exposure times can increase acquisition times to last more than an hour, potentially offsetting the benefit offered by not requiring a staining step.

Regardless of the method (antibody removal, bleaching or probe exchange), sequential labelling has yet to be implemented in a high-throughput super-resolution context. While the benefits offered by sequential labelling have yet to be fully harnessed, online fixation is also an under-explored technique.

4.1.2 Adhesion of Migratory Animal Cells During Cell Division

As a demonstration of the power of online fixation, the NanoJ-Optofluidics framework was used to address the origin of adhesion during mitosis. Most animal cells in culture undergo dramatic cell shape changes as they progress through mitosis. First of these is the process of cell rounding, requiring extensive remodel-

ling of the cell's cytoskeleton and cellular adhesion (Ramkumar et al., 2016). Migratory animal cells adhere to the extracellular matrix through integrins, and these link to the actin cytoskeleton through focal adhesions (Parsons et al., 2010). These are complex multi-molecular assemblies (Kanchanawong et al., 2010) important for cell migration (Parsons et al., 2010), mechano-transduction (Bershadsky et al., 2003) and cytoskeleton regulation and signalling (Burridge et al., 1996; Geiger et al., 2001). For cells to undergo the cell shape changes required for mitosis, these focal adhesions must be disassembled (Marchesi et al., 2014) but cells retain adhesion to their substrate by means of retraction fibres (Mitchison, 1992). These are narrow, actin-rich, membrane tubes which are established as the cell changes shape for cell division. They have been shown to be able to support significant forces despite lacking myosin II and are important in orienting the metaphase spindle (Théry et al., 2005; Fink et al., 2011) and assisting with cellular re-spreading after mitosis (Cramer et al., 1993; Mali et al., 2010). Despite their importance, the adhesion mechanism and the origin of retraction fibres remains unclear. Interestingly, Toyoshima et al. (2007) have shown mitotic cells orient their spindle using an unknown form of integrin-mediated, actin-dependent adhesion. Since retraction fibres adhere to the substrate and are also important for spindle orientation, it is possible the integrin-dependent effect they have observed is due to retraction fibres. This would imply retraction fibres adhere to their substrate through integrins, which are usually deposited by focal adhesions.

4.1.3 Dynamics of Adhesion Nano-clustering During T-cell Motility

Beyond either performing online fixation or sequential labelling, microfluidics allows both techniques to be combined in a straightforward manner. The ability to perform super-resolution imaging also adds target specific structural information which would be difficult to acquire otherwise. By combining information regarding a cell's dynamic behaviour, multiplexed labelling and nano-scale structural information, an integrated microfluidic and imaging system can provide unparalleled access to biological information. As a demonstration of this, the NanoJ-Optofluidics

framework was used to address questions regarding the impact of nano-clustering of signalling components of adhesions on T-cell mobility.

T-cells or T-lymphocytes are part of the immune system and originate in the thymus (hence the name). Naïve T-cells encounter antigens in the lymph nodes or periphery on contact with antigen-presenting-cells, at which point they become effector T-cells (Janeway, 2001). Effector cells are highly motile and can achieve velocities as fast as $25\mu m/min$ inside a mouse (Miller, 2002). This increased velocity is required for T-cells to find pathogens in the body (Dustin, 2004; Woolf et al., 2007; Teijeira et al., 2017). They migrate along the vasculature, between endothelia (diapedesis), within tissues and along dendritic cells in the lymph nodes (Friedl et al., 2008). Different types of integrins assist T-cells to adhere to other cells, the extracellular matrix or other substrates as well as assist with intercellular signalling (Shannon et al., 2015). In particular, the Lymphocyte function-associated antigen 1 (LFA-1) integrin connects flowing actin with the substrate below in a system called the 'molecular clutch' using many well known focal adhesion molecules to make the actin link, such as Paxillin, Talin and Vinculin (A. Smith et al., 2005; L. Chen et al., 2012; Katakai et al., 2013). LFA-1's function is important for T-cell function as it is require for T-cells to establish contact with antigen-presenting-cells (Janeway, 2001). LFA-1 groups into nano-scale clusters upon binding to its cognate ligand Intercellular Adhesion Molecule 1 (ICAM-1), and therefore super-resolution is required to identify these nano-clusters (Shannon, in preparation; Shannon et al., 2015). These adhesive nano-clusters are still not fully understood. One question is how these nano-clusters relate to normal adhesions. In other motile cells such as fibroblasts, cellular adhesions begin as small nascent adhesions at the leading edge of a cell. Nascent adhesions turn-over quickly (≈ 60 seconds) but some will grow in size, and eventually mature into elongated focal adhesions with $\approx 3\mu m$ in diameter and $\approx 3-10\mu m$ in length (Parsons et al., 2010). If nano-scale clusters are related to normal adhesions, they should bear the same markers and follow similar maturation patterns. Nascent adhesions can specifically be identified by focal adhesion kinase proteins which are phosphorylated at tyrosine 397 (pFAK) (Swaminathan

et al., 2016). As nascent adhesions mature, they activate Src family kinases (SFK) by phosphorylating them (Schlaepfer et al., 1999; Zhang et al., 2008). Work in the Owen lab indicates LFA-1 nano-clusters have a fast turn-over, and co-localise with pFAK and SFK proteins, similarly to normal cellular adhesions (Shannon, in preparation). Additionally, the same work has suggested that, when T-cell speed is affected through drug perturbation or genetic manipulation, nano-clustering of LFA-1 is affected (Shannon, in preparation). Whether this is a side-effect of the perturbations or there is a natural dependence between T-cell speed and LFA-1 nano-clustering remains unclear. The only way to address this is to know the speed of each individual cells as well as their individual cluster patterns, meaning this question can only be answered by imaging cells live and fixing them *in-situ*.

4.1.4 Chapter Scope

It is the goal of this chapter to demonstrate the development of an effective sequential labelling technique for *in-situ* imaging with microfluidics. Different elution and bleaching techniques were tested in the context of both cell culture dishes and PDMS devices. The NanoJ-Optofluidics framework is then used as a proof of principle for a high-throughput compatible, *in-situ* sequential labelling experiment. To demonstrate biological applicability, the NanoJ-Optofluidics framework addresses the retraction fibre hypothesis using online fixation. The framework is also used for online fixation, sequential labelling and super-resolution imaging of T-cells to explore the relationship between T-cell speed and adhesion nano-clustering.

4.2 Results

4.2.1 Methods for High-Throughput Sequential Labelling *In-situ*

In a high-throughput context, any sequential labelling protocol ideally requires as short a processing time as possible. However, secondary labelling simplifies experimental design since it allows the use of off-the-counter, reliable commercial secondary antibodies. Secondary labelling also significantly increases label density and the more labels there are present in an image, the faster a super-resolution image can be acquired (Agasti et al., 2017). Therefore, if the linkage-error arising from having two antibodies stacked can be accepted, secondary labelling can potentially compensate for the increased labelling time in a high-throughput SMLM experiment. As a first approach, a Glycine acidic solution (pH 2.0) was tested as established by Nakane (1968), but several hours were required before a significant signal reduction was observed and this was not pursued further.

Next, the method established by Tramu et al. (1978) was attempted using NanoJ-Optofluidics. While more recent implementations of this method (Micheva et al., 2007) heat the sample, the original paper did not. These techniques were established in tissue samples, where heating the sample for antigen retrieval is common. Cultured cells often require no heating and have shorter processing times. Since the newer paper does not justify the use of heating, it is not unreasonable to consider heating is added to accelerate the chemical process, but may not be necessary. The acidic buffer was tested to elute secondarily labelled cultured cells at room temperature. Initial attempts made use of PDMS devices and were successful in removing all signal from cells (figure 4.1). However, the tendency of the acidic buffer to generate bubbles proved it inadequate for use in PDMS. Simultaneously, transmitted light imaging during the elution process revealed severe alteration of cell structure, to the point where flowing liquid in the PDMS device could strip cells from the glass substrate (figure 4.2). Because of this impact, the acidic solution was not pursued further.

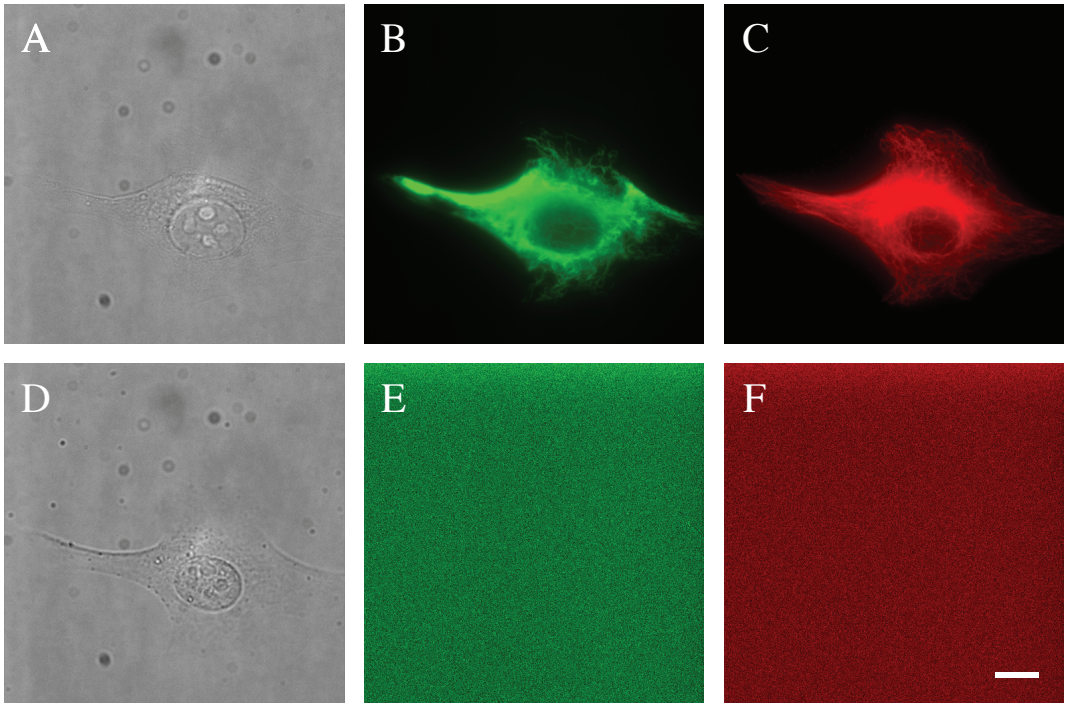

Figure 4.1: HeLa cell having its signal removed by an acidic buffer. A - Transmitted light image of the cell; B - Vimentin secondarily labelled with Alexa Fluor 488; C - Microtubules secondarily labelled with Alexa Fluor 647; D-F - Channels A-C after 70 seconds of incubation in acidic buffer, respectively. Contrast was adjusted to demonstrate only camera noise is visible after incubation in buffer. The mean of the camera grey values for signal resulting from the cell is $\approx 21,000$ in B and $\approx 10,000$ in C, whereas E and F both have a mean value of $\approx 1,570$. Scale-bar: $10\mu m$.

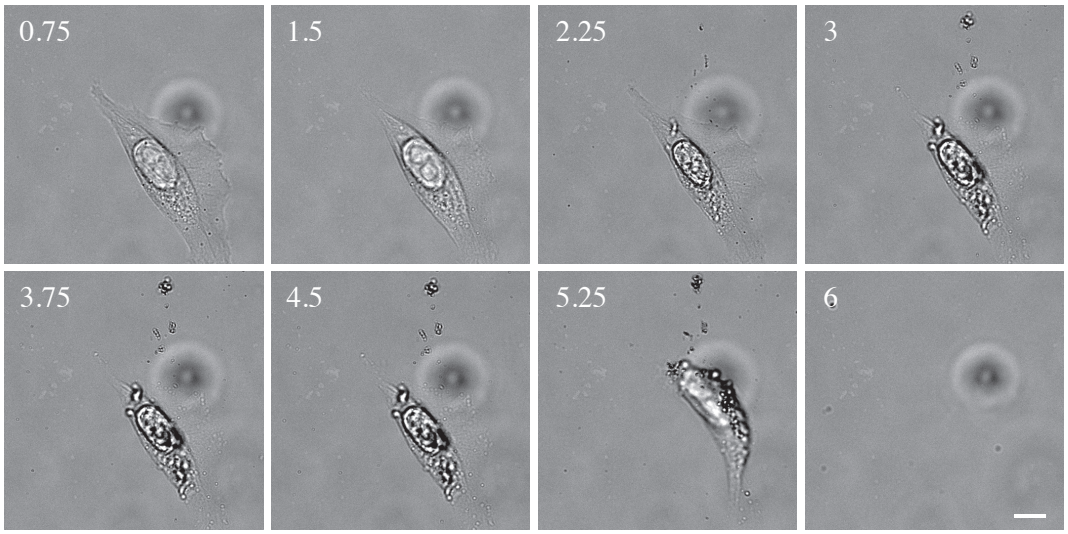

Figure 4.2: Cells being washed away in a PDMS device after acidic buffer elution. Images are shown after background correction and frames are labelled by their time-stamps in minutes. Scale-bar: $10\mu m$.

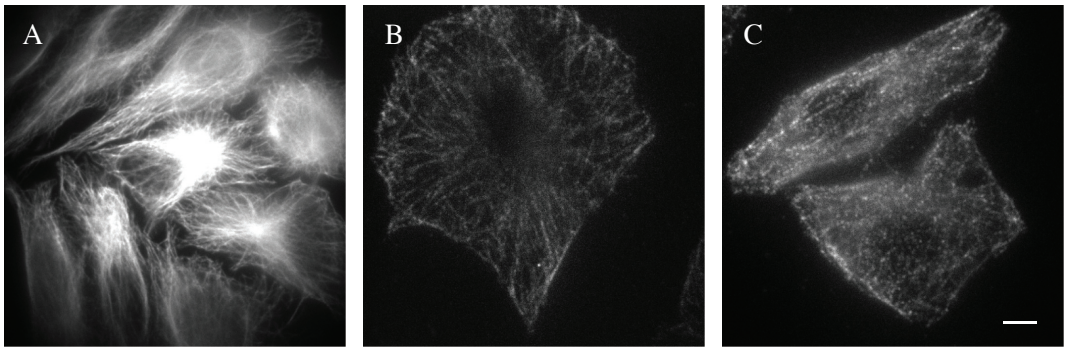

Figure 4.3: HeLa cell having its signal removed using the madSTORM buffer. A - Microtubules labelled with Alexa Fluor 647 prior to elution; B - Cell signal is reduced by $\approx 90\%$ after 5 washes of 1 minute each. Contrast was adjusted to demonstrate structure is still present; C - Cell signal remains stable after 10 further washes of 5 minutes each. Contrast was adjusted to demonstrate structure is still present. Scale-bar: $5\mu m$.

One way to elute antibodies is through denaturation, as demonstrated by methods which primarily use heating to remove antibodies (Kolodziejczyk et al., 1986). Biochemical *in-vitro* assays of antibody function use dithiothreitol (DTT) to reduce the disulphide bonds that make up an antibody's secondary structure. Disulphide bonds keep together the two components of an antibody, the light and heavy chains, and the binding site for antigens is found between these two chains (Moser et al., 2010). One *in-vitro* DTT assay (Hong et al., 2009) tested the structural changes over time caused by DTT and yielded that within 5 minutes, no more effect is seen on antibody structure. Here, DTT was tested as a possible fast elution agent, using cell culture dishes and manual procedures. Cells secondarily labelled for microtubules (Alexa Fluor 488) and vimentin (Alexa Fluor 568) were incubated for 10 minutes in 20mM DTT, with the DTT solution replaced once during the incubation period. Despite the fact the 20mM concentration corresponds to twice the concentration used in the *in-vitro* assay, only a 20-30% reduction in signal was observed, and subsequent incubations with DTT did not further decrease the signal (not shown). It is possible that the light and heavy chains were indeed separated, but this did not significantly affect the ability of the individualised chains to bind to their targets. Because the fluorophores can be in either chain, we posited that this might not be sufficient to clear the signal. Given the inability to achieve significant signal reduction, DTT denaturing was not pursued further.

Chaotropic agents are also frequently used to elute antibodies from affinity purification columns (Narhi et al., 1997). After early attempts at establishing a protocol using a 3.5M MgCl solution (not shown), Yi et al. (2016) published the madSTORM buffer, also based on a 3.5M MgCl solution, but they demonstrate that the addition of a detergent, Tween-20, assisted with the elution process. Interestingly, many other successful elution methods have included the detergent Sodium dodecyl sulfate (SDS) (Pirici et al., 2009; Gendusa et al., 2014; Bolognesi et al., 2017). The Yi et al. (2016) method, called madSTORM, requires only 3 washes of 2 minutes each with the buffer to achieve elution in T-cells labelled with directly labelled primary antibodies. To test if the same buffer could elute secondarily labelled cells, HeLa cells were fixed and stained for microtubules with Alexa Fluor 647 in cell culture dishes. After washing manually 5 times for 1 minute with the madSTORM buffer, $\approx 90\%$ of the signal was removed, but some structure was still visible (figure 4.3 A,B). Repeating the process on the same cells 10 times for 5 minutes each, the signal was never completely removed (figure 4.3 C), even after incubating the cells in madSTORM buffer overnight (not shown). Overall, with secondarily labelled cells, the signal could be significantly removed, but never completely, which makes the madSTORM buffer applicable only for experiments with directly-labelled primary antibodies.

To achieve a complete signal removal with madSTORM, the remaining signal must be bleached. As a complementary strategy, signal removal by bleaching was also tested. Two solutions were tested: hydrogen peroxide and a 0.1% sodium borohydride solution. Both of these solutions generated significant air bubbles, which made them inapplicable for use with PDMS devices, but worked well with cell culture dishes (not shown). While signal removal could be achieved with both, sodium borohydride was found to act the fastest (10 minutes versus 1 hour). Signal removal was accelerated when simultaneously exciting the samples with the illumination laser (not shown; as previously described in (Lin, Fallahi Sichani and Sorger, 2015; Valley et al., 2015)).

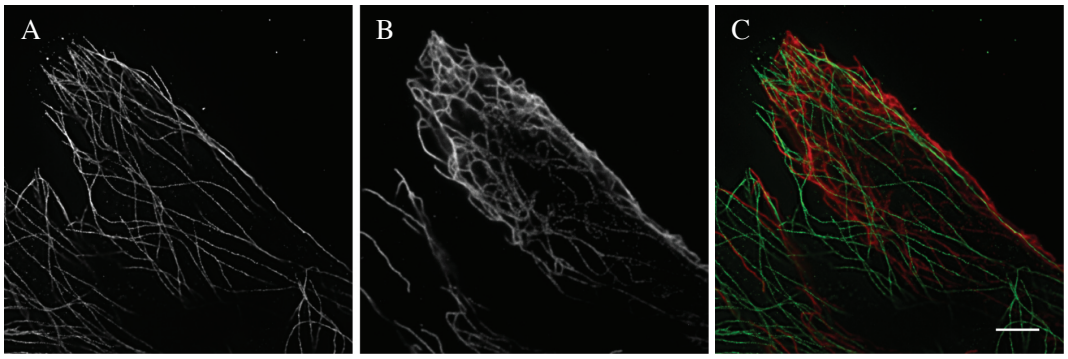

Figure 4.4: Super-resolution Exchange-PAINT imaging of HeLa cells secondarily immuno-labelled for microtubules and vimentin. A - DNA-PAINT reconstruction of Microtubules; B - DNA-PAINT reconstruction of Vimentin after the microtubule strand was washed away; C - Overlay of A and B. Scale-bar: $3\mu m$.

4.2.2 Multi-modal, Sequential Labelling Super-Resolution Imaging Enabled by Automated Microfluidics

While madSTORM and bleaching can remove a labelling from a cell, both techniques require the sample to be restained before a new target can be imaged. With Exchange-PAINT, however, only one staining step is required. As an alternative approach, super-resolution exchange paint was tested with the NanoJ-Optofluidics platform. Cells were manually fixed and stained for microtubules and vimentin using DNA-PAINT tagged antibodies. First, to image microtubules, cells were immersed in imaging strands which complement the target strands attached to the microtubule's secondary antibody (figure 4.4 A). After imaging the cells, they were washed of imaging strand, immersed in new strands targeting vimentin's secondary antibody and imaged (figure 4.4 B,C). This process was achieved *in-situ*, without requiring the sample to be removed from the microscope, but was achieved manually.

It is worth noting that any of the above mentioned techniques can be performed in tandem. Therefore, different techniques can be used according to experimental preference. The NanoJ-Optofluidics platform also offers the option to perform online fixation, meaning cells can be imaged live, fixed *in-situ*, immuno-stained and imaged without ever needing to be removed from the microscope. As a proof of concept, HeLa cells stably expressing Tubulin-GFP were cultured on a glass bottom

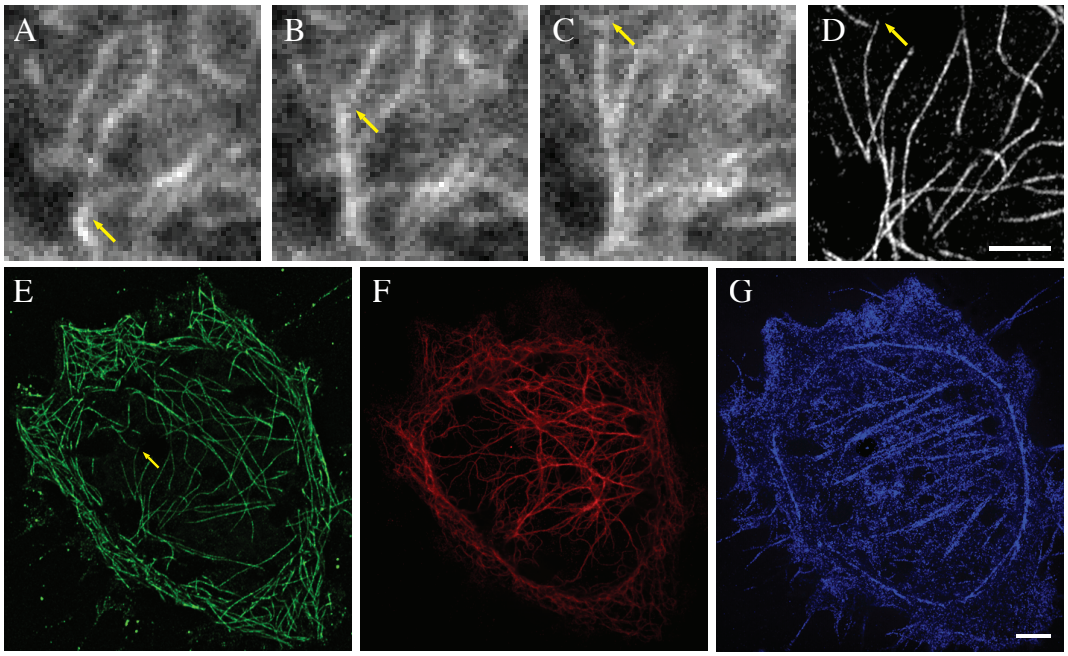

Figure 4.5: Multi-modal super-resolution imaging with NanoJ-Optofluidics. Live TIRF and online fixed super-resolution imaging of the cytoskeleton of a representative HeLa cell. A-C) Live TIRF imaging of tubulin-GFP. A microtubule (yellow arrows) could seen growing just prior to fixation; D) DNA-PAINT imaging of the same microtubule. Scale-bar: $2\mu m$; E) Full cellular view of the DNA-PAINT imaging of the microtubules and dSTORM imaging of vimentin (F) and actin (G). Scale-bar: $3\mu m$.

cell culture dish and imaged live for 6 minutes while immersed in $1.5mL$ of Ringer's solution. 19 cells were imaged by visiting multiple FOV's throughout the time-lapse. Using NanoJ-Optofluidics, $0.5mL$ of 16% PFA was added to the dish, resulting in a working concentration of 4%, and cells were fixed for 10 minutes (figure 4.5 A-C). After fixation, the cells were permeabilised, stained using a primary antibody against tubulin, washed and secondarily stained using a DNA-PAINT labelled antibody. After staining, the cells were immersed in imaging strands and DNA-PAINT super-resolution imaging was performed (figure 4.5 E). It should be noted microtubules are notoriously sensitive to temperature and fixation, and the PFA dilution method using NanoJ-Optofluidics has shown consistent fixation performance throughout several experiments (not shown). The resulting super-resolution fixed images show good correlation with the live images (figure 4.5 C-D). After imaging, the DNA-PAINT strands were washed away, and the cells were stained for vimentin with a primary antibody directly labelled with Alexa Fluor 647. Having washed the

antibody away, the pumps added dSTORM imaging buffer, allowing dSTORM imaging to be performed (figure 4.5 F). Once vimentin imaging was finished, the label was bleached using 0.1% sodium borohydride and the microscope's illumination for 10 minutes. This permitted a new staining, with Phalloidin-Alexa Fluor 647, followed by new addition of fresh dSTORM buffer (figure 4.5 G). As a result, automated three-colour SMLM has been achieved (figure 4.5 E-G). Overall, figure 4.5 demonstrates the NanoJ-Optofluidics platform has enabled cultured cells to be online fixed, immuno-stained and sequentially labelled *in-situ* in an automated manner. In a collaboration with the Jungmann lab, who developed Exchange-PAINT, the cell culture dish technique described in chapter 3 was adopted in (Schnitzbauer et al., 2017), further demonstrating the simplicity of the approach.

4.2.3 Online Fixation Reveals Origin and Adhesion Mechanism of Retraction Fibres

Having succeeded in a proof of principle experiment, the NanoJ-Optofluidics platform was applied the study of retraction fibres. Here, it is hypothesized that retraction fibres adhere to the substrate through integrins. Should this be true, it can be further hypothesized that these integrins would be deposited by focal adhesions, which disassemble prior to mitosis. To test this, an adherent and migratory human cell line, the Retinal Pigmented Epithelial cell line (RPE1), was used. To track focal adhesion dynamics, RPE1 cells were stably transformed with a Zyxin-GFP plasmid. Zyxin is a dynamic cytoplasmatic signalling component of focal adhesions which also interacts with actin (Burridge et al., 1996; Kanchanawong et al., 2010; M. A. Smith et al., 2014) and here serves as a marker for functional focal adhesions. Live-imaging with Zyxin-GFP shows focal adhesions are disassembled prior to mitosis (figure 4.6 D, green channel). Paxillin in RPE1 cells, an important focal adhesion scaffold protein (Parsons et al., 2010; M. C. Brown, 2004), recapitulated the observed Zyxin-GFP signal over similar time-scales (data not shown), as previously described (Marchesi et al., 2014). To enrich the population of mitotic cells, cells were seeded in imaging dishes and synchronised prior to mitosis by incubating them in media containing $9\mu M$ Ro-3306, a CDK1 inhibitor. Us-

ing the NanoJ-Optofluidics framework, cells had the media containing the inhibitor washed away, and it was replaced with 1.5mL of fresh media. Taking advantage of the highly automated capacity of the NanoJ-Optofluidics it was possible to approach this problem in a high-throughput manner, selecting several random stage positions to be imaged over a 26 minute period, at 1.5 minute intervals. The cells were then fixed by adding 0.5mL of 16% PFA to the media, diluting the PFA *in-situ* to a working concentration of 4%. The cells were then stained with DAPI, Phalloidin-TRITC and secondarily immuno-labelled for integrin using Alexa Fluor 647.

Roughly 25% of the stage positions contained dividing cells (two replicates: 40 out of 180 and 30 out of 100 FOV), whereas one experiment performed without incubating cells in the inhibitor yielded only roughly 5% of stage positions containing mitotic cells (4 out of 80 FOV). This demonstrates the synchronisation step performed with the NanoJ-Optofluidics resulted in an $\approx$ 5-fold increase in mitotic cells being acquired. Fixed cells which appeared mitotic through the DAPI signal (figure 4.6 A) contained retraction fibres (figure 4.6 C,I-III) and, at the coverslip surface, all of the observed retraction fibre signal coincided with an integrin signal (figure 4.6 I-III). By comparing the fixed integrin signal with the Zyxin-GFP live imaging signal, it was observed the integrin signal always coincided with past locations of Zyxin positive focal adhesions (figure 4.6 D). The same pattern was consistent throughout the 3 replicates of the experiment. One interesting additional observation is that while in fixed interphase cells integrin consistently locates to Zyxin-GFP sites (figure 4.7), when cells enter mitosis, the Zyxin signal seems to stop correlating with the integrin signal. In figure 4.6 D, this can be seen in the difference between timepoints 12 and 15, and this effect was consistently observed on all imaged cells.

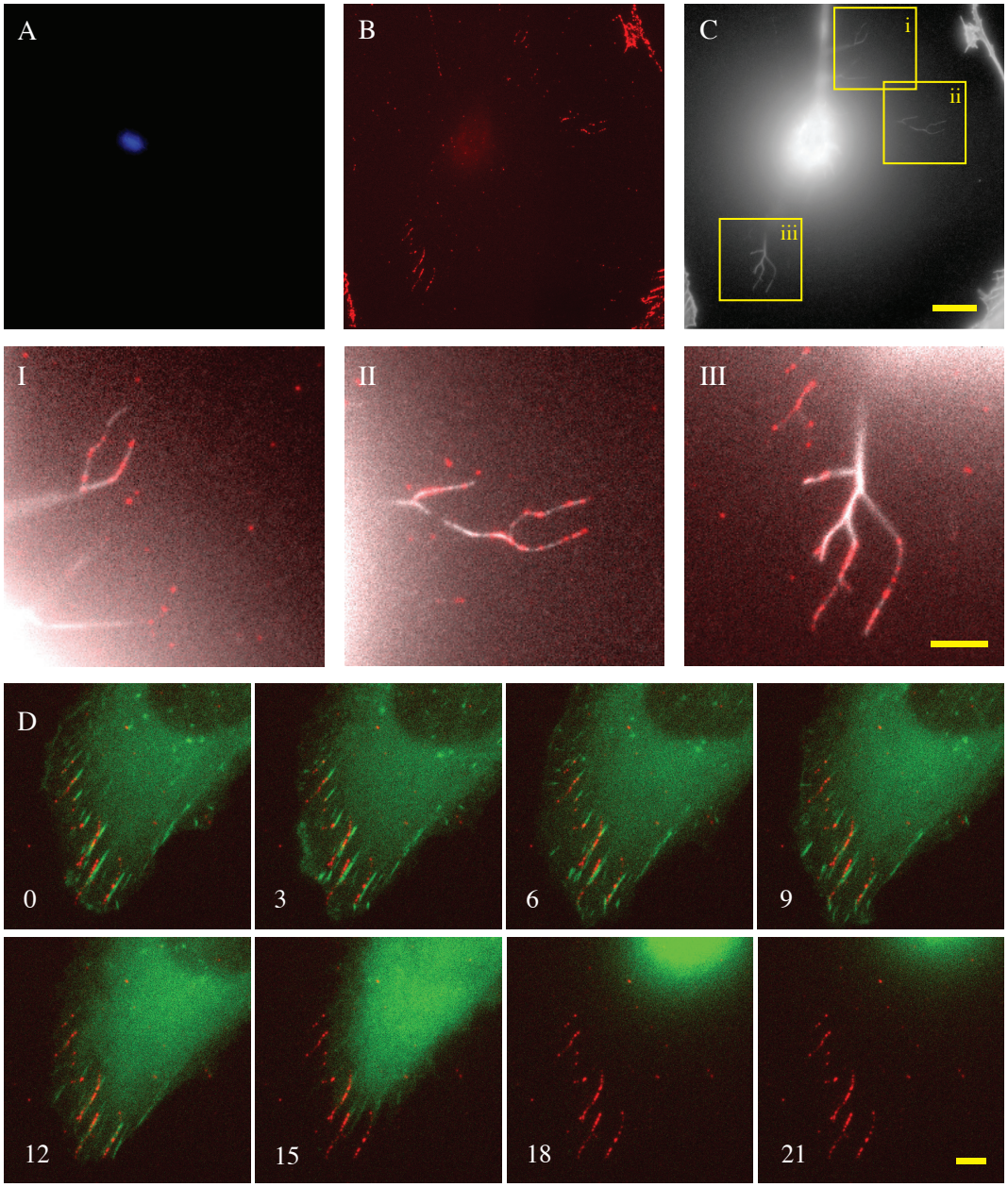

Figure 4.6: Online fixation reveals integrin link to retraction fibres and a focal adhesion associated origin. Shown is a representative mitotic RPE1 cell which was imaged live, fixed and stained using the NanoJ-Optofluidics framework. A - DAPI signal of chromosomes in metaphase above the focus; B - Integrin signal; C - Phalloidin signal. The cell body has a much more intense signal than the retraction fibres and therefore the image was gamma adjusted to enhance visibility ($\gamma = 0.05$). Scale-bar: $15\mu m$; I-III - Zoom of the regions of image C labelled as i-iii, with the integrin signal (B) overlaid. Scale-bar: $5\mu m$; D - Time-lapse of the cell shown in A-C prior to fixation. Green channel - Live zyxin-gfp imaging; Red channel - post-fixation integrin signal (B). Frames are labelled by their time-stamp in minutes. Scale-bar: $5\mu m$.

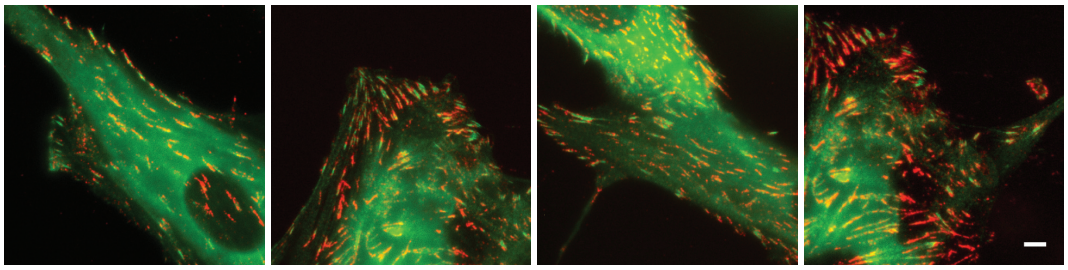

Figure 4.7: Four example interphase cells demonstrating integrin signal corresponds to focal adhesion (Zyxin-GFP) sites. Green channel - Fixed Zyxin-GFP imaging; Red channel - Fixed integrin signal; Scale-bar: $5\mu m$.

4.2.4 Online Fixation and Super-Resolution Sequential Labelling Reveals Link Between T-cell Speed and LFA Cluster Size

Having demonstrated a biological application for online fixation and staining, NanoJ-Optofluidics was next used to study T-cell motility and adhesion. T-cells adhere to other cells through LFA-1 (Janeway, 2001; A. Smith et al., 2005; L. Chen et al., 2012; Katakai et al., 2013) and their motility is important for their immunological function (Dustin, 2004; Woolf et al., 2007; Teijeira et al., 2017). Work in the Owen lab has indicated a potential link between T-cell motility and LFA-1 nano-clustering (Shannon, in preparation). To address this, NanoJ-Optofluidics was used to automatically fix cells after measuring their speed and immuno-stain for LFA-1. Primary T-cells were seeded on ICAM-1 coated dishes and allowed to settle. By tiling fields of view 6x6, and imaging over a period of 10 minutes with transmitted light, the cells could be tracked even if they left their starting FOV. After fixation, these cells were immuno-stained with a directly labelled antibody for LFA-1, dSTORM imaged and the resulting data was analysed using a Bayesian cluster analysis algorithm (Griffie et al., 2016). Because Bayesian cluster analysis is dependent on the size of the ROI to provide an accurate answer, several ROI's were measured for each cell. The insets in figure 4.8 A and B show two representative cells, cell tracks and cluster data. Overall, the average per-cell size and LFA-1 density of the clusters was uncorrelated with cell speed (not shown). However, the number of clusters for each cell was inversely correlated with T-cell speed (n=16,

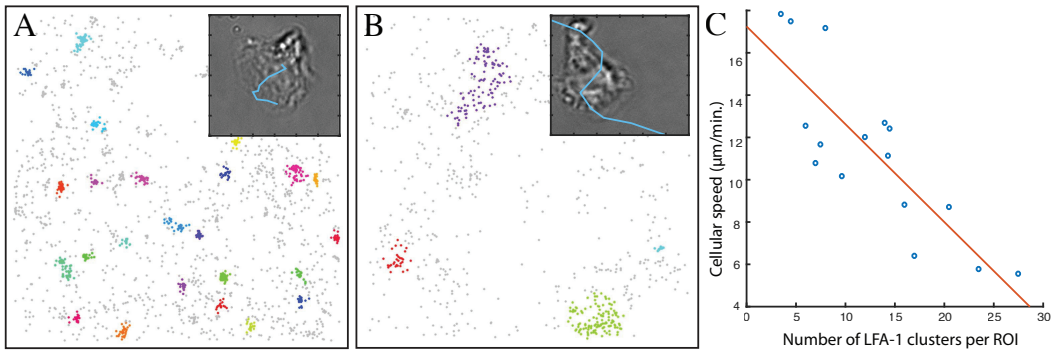

Figure 4.8: Online fixation and super-resolution imaging reveals a correlation between T-Cell speed and the number of LFA clusters. A,B) Example images of clusters identified on slow (A) and (B) fast cells. Insets show representative cells and their relative cell track difference; C - Number of clusters measured per ROI on each T-cell versus average cell speed. Blue dots correspond to individual cells whereas the orange line shows the least squares fit (see table 4.1).

figure 4.8 and table 4.1). This demonstrates that T-cell speed naturally correlates to the number of LFA-1 clusters.

Motile cells continuously disassemble their adhesions as they migrate. T-cells are highly motile and it seems that this speed leads to a reduction in the number of adhesive clusters. It can then be hypothesised that this speed does not allow enough time for adhesions to mature in the same way as nascent adhesions in non-leukocytes. Were this to be true, faster cells should have a smaller number of mature adhesions. pFAK and phosphorylated SFK proteins (pSFK) can serve as markers for different stages of nascent adhesion maturation (Swaminathan et al., 2016; Schlaepfer et al., 1999; Zhang et al., 2008). To test the above hypothesis, pFAK and pSFK were sequentially labelled using directly labelled primary antibodies and imaged in the same cells as in figure 4.8. Because focal adhesions are tightly packed structures (Kanchanawong et al., 2010), elution should be helpful to reduce steric hindrance and therefore the madSTORM protocol was used[1]. While pSFK showed a weak correlation to cell speed, pFAK, which appears earlier in maturation than SFK phosphorylation (Zhang et al., 2008), showed no correlation (table 4.1). Therefore these results do not allow a conclusion to be reached regarding T-cell adhesion maturation. Nevertheless, the results demonstrated NanoJ-Optofluidics was suc-

[1]This protocol was optimised in the Owen lab for primary antibodies. See section 4.3.4.

Marker	Pearson Coef.	Adjusted R-Squared	p-value
LFA-1	-0.851	0.704	$2.9218e^{-5}$
pSFK	-0.540	0.241	0.031
pFAK	0.1616	0.0434	0.550

Table 4.1: Correlation values between the number of clusters of different adhesion markers and T-cell speed. Pearson Coef. - Pearson correlation coefficient; Adjusted R-Squared and p-value are given for a least squares linear fit.

cessfully used for online fixation, staining, super-resolution imaging and sequential labelling to address a biological question.

4.3 Discussion

4.3.1 Antibody Elution Methods for Microscopy

The elution methods tried in section 4.2.1 yielded mixed results, with bleaching and Exchange-PAINT demonstrated as the more straightforward approaches. However, it is interesting to note the use of madSTORM sequential labelling in section 4.2.4. These results were obtained in collaboration with the Owen lab, which had previously tested the madSTORM protocol successfully. The madsSTORM buffer was not observed to elute efficiently in section 4.2.1, but there are several differences between the two experiments. Most importantly, the T-cell results were obtained using primary antibodies, whereas prior tests were performed on secondarily immuno-labelled cells. It is often the case that different antibodies can have different affinities for their targets (Eisen, 2014; Pierobon et al., 2011), and this is especially the case if the antibody is provided as polyclonal stocks, like those used here. Polyclonal stocks contain several species of antibodies which are selective for the same target protein, but not necessarily for the same antigen (Saerens et al., 2008; Pierobon et al., 2011). Antibody suppliers tend not to provide biochemically assayed affinity values such as a the k_d, or equilibrium constant. This constant determines what concentration is require to achieve an equilibrium between binding and dissociating antibodies (Reverberi et al., 2007). The lower this value, the greater the affinity of an antibody to its target. As a proxy for this value, the concentration a supplier recommends to perform a staining can be used. The primary antibodies used in section 4.2.1 had recommended concentrations ranging from 0.025 to $1\mu g/mL$, whereas the secondary antibodies ranged from 0.1 to $1\mu g/mL$. In section 4.2.4, the primary antibody against LFA-1 has a recommended concentration of $\approx 9\mu g/mL$ and the pFAK antibody has a recommended concentration of $1-2\mu g/mL$. *A posteriori* coupling to a fluorescent dye can lower affinity as well. It is possible the signal removal with these primary antibodies succeeded because elution was more successful with antibodies of potentially lower affinity. Additionally, the antigen abundance is orders of magnitude greater for microtubules

and vimentin than for LFA-1, pFAK or SFK.

In the original madSTORM paper, they attempt to distinguish between bleaching and elution by comparing cells stained with one antibody and these were either fixed with 4% PFA after the staining (post-fixed) or were not post-fixed (Yi et al., 2016). The post-fixed cells required more washes with the elution buffer, implying the antibodies were not being removed as effectively due to PFA cross-linking the antibodies to the cell. Yi et al. (2016) do not claim to fully remove the prior signal and never validate their elution process by performing a secondary staining against any remaining primary antibody. When performing sequential labelling with primary antibodies, this is generally not a concern as there is no issue of antibody cross-talk. This means that they can not distinguish elution from bleaching when they observe a signal reduction. In fact, to ensure full signal removal in section 4.2.4, bleaching was performed during elution by shinning the sample with the microscope illumination at full power. Overall, the madSTORM protocol can potentially be considered a combination of elution and bleaching, limiting the use of the protocol to sequential experiments using primary antibodies. Nonetheless, this is still a useful approach for dense multi-molecular structures such as the T-Cell receptor complex studied in the madSTORM paper and the nano-clustered focal adhesions studied in section 4.2.4.

There are many examples of other multi-molecular structures throughout the cell. Therefore, elution approaches still warrant further investigation. Specifically, the low pH approach shown in figure 4.1 could be optimised to reduce the impact on cellular structure. First, the flow-rates used in the PDMS devices (figure 4.2) were not fully optimised and it is possible that, using the cell culture dish approach, the elution process is more gentle. Second, tissues undergo prolonged fixation and paraffin embedding which is likely to increase structural integrity. Because of the extracellular matrix, tissue sections are also potentially more stable than single cells attached to glass. The fixation step used in most of the protocols used in this thesis has been a standard 4% PFA fixation for 10 minutes. Greater cellular stability could be achieved by performing more efficient fixation, either by incubating longer, using

glutaraldehyde in addition to PFA, or by using the PFA pH-shift method (Berod et al., 1981; Eldred et al., 1983). This method is based on the fact PFA is more efficient at high-pH levels and by fixing first at a physiological ph (≈ 7.4) and then shifting to a more basic environment, cells could be fixed more efficiently. Should the protocol be optimised sufficiently to not cause structural damage to the sample, it is still not clear whether the signal removal that was observed was due to elution or bleaching. Cells would have to be eluted and then counter-stained using secondary antibodies to determine the efficiency of elution. PDMS-based flow-cells could not be used with this elution buffer due to the air bubbles generated, and the shear stress generated from flow-rates inside the channels could damage eluted cells. The NanoJ-Optofluidics platform however, can be used to perform any these protocols due to reduced shear stress and regardless of the presence of bubbles.

4.3.2 Multiplexing Methods for High-Throughput Super-Resolution Microscopy

The need to perform multiple rounds of staining can be limiting in a high-throughput experiment. Liquid exchange is fast when compared with the amount of time an antibody incubation can take. For researchers using microscopes in microscopy facilities that charge imaging time, any time that is lost while performing imaging can be prohibitively expensive. There are methods to reduce staining times, however. With secondary antibody stainings, the secondary incubation step may be skipped if primary antibodies are pre-labelled with fluorescently-tagged Fab fragments (J. K. Brown et al., 2004; Smolinski et al., 2006). The antibody incubation time itself can be optimised, as the standard 1 hour incubation is a generic guideline and high-affinity antibodies can have shorter incubation times (Johnstone et al., 1990; Reverberi et al., 2007). This can be improved with higher temperatures, as these reduce the time required to each equilibrium, so for an *in-situ* staining with a microscope incubator set at 37C, the incubation time can be reduced further (Johnstone et al., 1990; Reverberi et al., 2007). Increasing the antibody concentration will also reduce the total required incubation time. Usually, working antibody solutions are diluted considerably to reduce cost but with the small volumes used

with the NanoJ-Optofluidics framework, the solutions can be concentrated slightly and yet still significantly assist with reducing incubation times.

It would be ideal for *in-situ* high-throughput experiments to not require a staining step at all. Recently, the IRIS, or integrating exchangeable single-molecule localisation method, has been developed (Kiuchi et al., 2015). IRIS uses a concept similar to PAINT in that a sample is immersed in a probe which only temporarily binds to its target. SMLM is achieved by imaging these binding events. IRIS is different from DNA-PAINT in that it does not require a DNA-labelled probe that is stably attached to it's target, like an antibody. This means the sample only needs to be immersed in the probe, and imaging can be done without requiring a staining protocol. Kiuchi et al. (2015) use Lifeact, an actin specific peptide probe (Riedl et al., 2008), to achieve high-density SMLM imaging of the actin cytoskeleton. This can be achieved because life-act has a binding half-life of only 44ms (Kiuchi et al., 2015). To image other targets, they tested the ability to wash away and the binding half-life of cellular proteins known to bind to specific structural targets, such as CLIP-170 (Komarova et al., 2002). CLIP-170 only binds to growing microtubules, but nonetheless, it allowed them to image these with super-resolution SMLM. By testing several different cellular proteins for different targets, like intermediate filaments and focal adhesions, IRIS achieved 4 colour multiplexed imaging.

By combining the ability to perform bleach-free single molecule imaging, simple multiplexing and removing the need for a staining step, the IRIS approach is very promising for multiplexed, high-throughput SMLM imaging. The approach of Kiuchi et al. (2015) to obtain probes other than Lifeact was to test cellular proteins with known binders. However, all that is required is a probe which is specific, but has a short binding time/low affinity to its target. In principle, a specific but low affinity antibody could be used. Current monoclonal antibodies could be genetically perturbed to reduce their affinity, thereby enabling IRIS imaging. In recent years, several new types of synthetic probes have also been engineered against arbitrarily defined targets (*Nanobodies*; Holliger et al., 2005; *Aptamers* Iliuk et al., 2011; *Adhirons* Tiede et al., 2014; *Affimers* Bedford et al., 2017). These could be developed

to be specific but with low affinity, thereby enabling IRIS to be extended to any number of arbitrary targets. NanoJ-Optofluidics could then leverage these new probes to perform highly multiplexed SMLM imaging without requiring any staining steps in between imaging rounds, and therefore greatly increasing throughput.

4.3.3 Integrin from Focal Adhesions Determines Retraction Fibre Adhesion Sites

By performing live imaging, online fixation and staining with the NanoJ-Optofluidics platform, a single experiment was able to show retraction fibre attachment sites to the cell-substrate are rich in integrin signal, and this signal corresponds to sites of prior focal adhesions. Overall, this indicates that focal adhesions leave behind integrin adhesions sites during their disassembly, which serve as anchoring sites for the retraction fibres that appear as mitosis progresses and cells become rounded. While previously published data hinted at such a possible mechanism (Cramer et al., 1993; Toyoshima et al., 2007), attempts to address it by directly labelling integrin for live imaging in the Baum lab have previously failed (not shown). By using an *in-situ* fluid exchange experiment, these issues were obviated by being able to directly correlate live imaging and fixed imaging of the same cells.

In our data, the fixed integrin signal was always tightly correlated with the Zyxin signal in interphase cells (figure 4.7). In the time-lapse in figure 4.6 D, it can also be seen the fixed integrin does not overlap exactly with the live Zyxin-GFP signal until the 12 minute frame, just prior to mitosis. This is likely due to integrin constantly being deposited and recycled by focal adhesions and therefore the fixed integrin signal will only correspond to the focal adhesion's last site of attachment before these were disassembled for mitosis. However, one interesting observation is that at frame 15, after the cell has begun rounding up, the integrin signal no longer overlaps exactly with the Zyxin signal at this point. This means integrin stopped correlating with focal adhesions between the 12 and 15 minute mark. The focal adhesions are still seen at minute 15 but they seem to move towards the rounding cell body, whereas the integrin signal stays behind. This movement of Zyxin signal towards the cell body while leaving the integrin signal behind is consistent for all

observed cells. This leads to an hypothesis where, prior to mitosis beginning, there is a severing of the connection between focal adhesions and integrins, allowing the rounding up process to initiate even though the full macro-molecular structure of the focal adhesion has not yet been fully disassembled. Focal Adhesion Kinase (FAK), Paxillin, Talin and Vinculin all mediate integrin signalling and, when looking at their distribution in focal adhesions, are located nearer to the membrane than Zyxin (Burridge et al., 1996; Kanchanawong et al., 2010). It would be possible any of these proteins could be responsible for this severing. This severing hypothesis could be tested by performing an online fixation and sequential labelling experiment with the NanoJ-Optofluidics. Zyxin would be imaged live, and actin, integrin, FAK, Paxillin, Talin and Vinculin would all be sequentially labelled. If focal adhesions do indeed sever from integrins prior to their full disassembly, whichever proteins are dragged along with the focal adhesion will be dragged with Zyxin whereas any protein involved in the severing will either disappear or localize to integrins. Therefore, the severing hypothesis could be tested and the most likely candidate could be identified in one microfluidic experiment.

4.3.4 T-cell LFA-1 Nano-Cluster Size is Related to Cell Speed

table 4.1 shows that the the number of LFA-1 clusters in a cell is correlated with T-cell speed, demonstrating a natural relationship between both. pFAK and pSFK were also imaged to test whether these clusters show the hallmarks of nascent focal adhesions, since work in the Owen lab indicates this is the case (Shannon, in preparation). table 4.1 indicates these two markers are not correlated. However, the mean number of clusters captured per ROI was ≈ 10 for pFAK and SFK, which is fairly low. The number of measured cells (16) could be increased for greater certainty and the fact the experiment lacks replication means these results require further verification. It is also possible the ROI method required by the Bayesian analysis has introduced a sampling bias, and using a scale-independent analysis algorithm may offer a more accurate answer. Many different approaches have been developed recently (Levet et al., 2015; Mazouchi et al., 2016; Malkusch et al., 2016; Andronov et al., 2016) and a more systematic comparative approach may be required

to identify the algorithm which is most adequate for such low numbers of potential clusters. Nonetheless, the tentative correlation observed in figure 4.8 C shows promise and warrants further exploration. It is important to note this kind of single cell measurement was greatly facilitated by correlative live- and super-resolution imaging, This kind of correlation could be achieved by using gridded coverslips, but this would greatly increase the manual workload and therefore significantly increase the time it would take to acquire the data. As it is, the entire experiment described in section 4.2.4 could be performed in one day, making replication efforts straightforward.

4.3.5 NanoJ-Optofluidics Enables Dynamic and Multiplexed Super-Resolution Imaging

There are several experimental approaches which have been enabled by NanoJ-Optofluidics: drug application/release, online fixation, *in-situ* staining and sequential labelling are just the applications demonstrated here.

Capturing mitosis in animal cells is usually difficult due to the short division time (tens of minutes) compared to the length of the non-mitotic periods (12-24 hours, depending on cell line). By releasing cells from a cell cycle inhibitor (section 4.2.3), mitotic cells were enriched by up to 5-fold. This process is highly time-dependent. In early experiments, the release was performed *ex-situ* and the time required to begin the drug release, set up the microscope, and begin imaging was long enough that most cells had already begun mitosis. This reduced the number of cells which could be capture at appropriate time-points. By using NanoJ-Optofluidics to perform the release *in-situ*, most cells could be fixed at the right time, demonstrating the advantage of the approach. Any drug application experiment where timing is critical should benefit from this approach. For example, in depolymerisation assays, microtubules restart polymerisation in a matter of seconds (Vorob'ev et al., 2003; Gierke et al., 2010; Bearce, 2017). Being able to perform these assays while the cells are on the microscope should help to increase the rate of experimental success.

The ability to perform online fixation also has the potential to allow a cell's

historical behaviour to be correlated with it's fixed imaging, allowing structural information to be tied to dynamic information. The proof of principle experiment (figure 4.5 C,D) demonstrates how the dynamic behaviour of microtubules can be determined and correlated with super-resolution imaging. Two examples also demonstrate the approach is capable of revealing new biology. By imaging focal adhesions live and correlating with fixed actin and integrin imaging, a distinct origin mechanism for retraction fibres was demonstrated. Similarly, cell speed can only be measured live and nano-cluster analysis is best performed in fixed cells. By correlating both datasets directly, a tentative relationship between a nanoscale scale process and a macro-scale behaviour could be established.

Multiplexed SMLM imaging is also enabled by the NanoJ-Optofluidics platform. dSTORM imaging has largely been limited to one efficient fluorophore, Alexa Fluor 647 (Dempsey et al., 2011) and multi-colour imaging is difficult to achieve without trading off resolution in one channel. Figure 4.5 F and G demonstrate how, by using bleaching-based sequential labelling, multiple channels can be acquired using one fluorophore. Valley et al. (2015) used this same method to achieve 4 colour imaging, but through a manual process. Here, we demonstrated the protocol can be automated using NanoJ-Optofluidics. In contrast to dSTORM, Exchange-PAINT has been demonstrated to image up to 9 targets in a single cell. Up to 50 different imaging strands have recently identified as being compatible for multiplexing (Agasti et al., 2017). Figure 4.4 demonstrates that Exchange-PAINT can be achieved using NanoJ-Optofluidics and figure 4.5 E and F show how both Exchange-PAINT and dSTORM can be achieved in the same cells in an automated manner. By combining both of these techniques, researchers have a vast array of multiplexing options available to them.

4.4 Attributions

Christina Dix of the Buzz Baum lab transformed, maintained, and seeded RPE1 cells as described in the below methods. The Baum lab, and Christina Dix specifically, provided the reagents for the experiment and provided the methodological information. Where data relating to the RPE1 cells is mentioned as not shown, this data is the PhD work of Christina Dix (2017, In preparation). Michael Shannon of the Dylan Owen lab obtained T-cells, maintained them in culture and seeded cells as described in the below methods. The Owen lab, and Michael Shannon specifically, provided the reagents for the experiment and provided the methodological information. Where data relating to the T-cells is mentioned as not shown, this data is the PhD work of Michael Shannon (2017, In preparation). Pedro Matos Pereira of the Ricardo Henriques Lab labelled and tested the secondary antibodies used for DNA-PAINT in section 4.2.1 and section 4.2.2 using the immuno-staining protocol described in the below methods. Pedro also performed some of the madSTORM testing and image acquisition in section 4.2.1.

4.5 Methods

4.5.1 Cell Culture and Plasmid Transfection

Cell culture for the experiments described in section 4.2.1 and section 4.2.2 was performed as described in section 2.4.1.

hTERT-RPE1 cells for the experiments on section 4.2.3 were cultured in DMEM F-12 Glutamax (Gibco, 31331-028), with 10% fetal bovine serum (FBS), 3.4% sodium bicarbonate (Gibco, 25080-060), 1% Penstrep (Gibco, 15070-063). Plasmid transfection with the pArek1-EGFP-zyxin plasmid (Gift from A. Welman to the Baum lab; Welman et al., 2010) was carried out using Fugene HD (Promega, E2311). Positive cells were selected with $500\mu g/mL$ G418 (Calbiochem, 345812) to generate a stable cell line. Leibovitz's L-15 CO_2 independent media (Gibco, 21083-027) with 10%FBS was used as the imaging media. HeLa cells stably expressing Tubulin-GFP were a gift from the Baum lab.

To obtain T-cells, 8 week old mice were culled, lymph nodes and spleens harvested and sieved through $70\mu m$ strainers (BD Biosciences, 352350) in warm RPMI-1640 to achieve a single cell suspension. Cells were centrifuged at 300g for 5 minutes at RT and the cell pellet re-suspended in complete medium (RPMI-Glutamax, 10% FBS; Penicillin, Streptomycin, Sodium Pyruvate, 20 mM Hepes, $20\mu M$ 2ME). Cells were stimulated at a density of 3 million per ml with the addition of $1\mu g/mL$ of Concanavalin A (Sigma, L7647) for 2 days. After this time, activated cells were isolated and dead cells excluded by layering on a Ficoll gradient; cells were centrifuged for 10 minutes without a brake at 1800 rpm. Layered T cells were re-suspended at 2 million per mL in complete medium and 20ng/mL recombinant IL-2 (proleukin) added for expansion for 5 days. Cells were used for microscopy on day 5 to 9 post-stimulation with Concanavalin A. Glass bottom cell culture dishes with (Ibidi 80827) were coated with $2\mu g/mL$ murine recombinant ICAM-1 (R&D systems, 796-IC-050) for 1.5 hours at 37°C . Cells in culture were centrifuged at 350g and re-suspended in warm equilibrated serum free migration medium (RPMI-Glutamax, Pen/Strep, Sodium Pyruvate, 30mM Hepes, $20\mu M$ 2ME) to a density of

$1x10^6$ cells per mL. 200.000 cells were added to the imaging dish placed at 37 in the incubator to settle onto the glass for five minutes before live imaging.

4.5.2 Microscopy

The imaging dishes (Ibidi, 80606) used in section 4.2.1 and section 4.2.4 were seeded with nano-diamonds prior to imaging. To seed with nano-diamonds, dishes are first pre-activated with KOH $0.1M$ (Sigma, 38073-1EA) for 30 minutes. The KOH is then washed 5 times with PBS. A nano-diamond stock (Adámas Nanotechnologies, NDNV100nmMdCOOH) is briefly vortexed before removing a $5\mu L$ aliquot and diluting it in $500\mu L$ of PBS. The nano-diamond dilution is bath-sonicated for 5 minutes in 30 second pulses and centrifuged for 1 minute at 3900 rcf. The supernatant is then transferred to the pre-activated dishes and allowed to settle for 30 minutes. The dishes were washed twice with PBS and then once in Ringer's solution (section 2.4.1). Cells were seeded on the dishes and allowed to grow in media overnight before live imaging (section 2.4.1). Live-imaging for the experiments described in section 4.2.1 and section 4.2.2 was performed in Ringer's solution at 37°C without CO^2 added. For the section 4.2.4 experiments, cells were imaged on a Nikon TIe microscope with a 100x 1.49NA Apo TIRF objective and an Andor iXon897 camera. Except for where it is otherwise noted, all other imaging was performed on a Zeiss Elyra PS.1 microscope, with a 100x 1.47NA Apo TIRF objective and an Andor iXon897 camera.

For the experiment described in section 4.2.3, cells were synchronised prior to mitosis by incubating them with 9uM of a CDK1 inhibitor (Ro-3306; Enzo Life Sciences, ALX-270-463) for 15-20 hours. Cells were imaged with a 60x oil objective on a Nikon Ti-E with an Andor Zyla sCMOS camera and a CollLED pE-4000 LED illuminator. Once the cells were on the microscope, the media with inhibitor was replaced by drug-free media with the NanoJ-Optofluidics system and multi-location images were acquired every 1.5 minutes for 26 minutes prior to fixation.

4.5.3 Immuno-staining

Stainings were performed as in section 3.5.2, except where indicated below. In the figure 4.3 experiments, cells were seeded in coverslips (Carl Zeiss, 474030-9000-000) and fixed in ice-cold methanol (Sima, 322415). In the section 4.2.1 and section 4.2.2 experiments, immuno-stainings were performed *in-situ* using the NanoJ-Optofluidics system. Cells were fixed by adding $500\mu L$ of methanol-free 16% Paraformaldehyde from freshly opened ampules (Alfa Aesar, 43368) to $1.5mL$ of Ringer's solution and incubating for 10 minutes.

For DNA-PAINT labelling, secondary antibodies were pre-labelled according to Schnitzbauer et al. (2017). Target strand added to the anti-mouse antibody: TTATACATCTA. Complementary imaging strand was labelled with Cy3B on the 3' end. Target strand added to the anti-mouse antibody: TTTATTAAGCT. Complementary imaging strand was labelled with Atto655 on the 3' end.

In section 4.2.3 experiments, cells were fixed by adding $500\mu L$ of pre-warmed 16% Paraformaldehyde to $1.5mL$ of cell media and incubating for 20 minutes. They were then washed 3 times with PBS and 0.2% Triton-X was added for 5 min. 5% bovine serum albumin/PBS was used to block for 30mins at room temperature before the integrin B1 (Abcam ab30394) primary antibody was added Phalloidin-TRITC (Sigma, p1951) and DAPI (Thermo Fisher, D3571) were added with an Alexa Fluor 647 labelled secondary antibody (Thermo Fisher, A-21236). Cells were washed and imaged in PBS.

In section 4.2.4 experiments, cells were fixed by adding $500\mu L$ of pre-warmed 16% Paraformaldehyde to $1.5mL$ of cell media and incubating for 10 minutes. Cells were washed 3x2 minutes with PBS. Cell autofluorescence was quenched with a 10 minute 0.1% sodium borohydride incubation (Sigma, 213462), followed by 3x2 minutes PBS washes. These steps were performed with the incubation set at 37 degrees celsius, however, the incubation was turned off and the microscope and sample were allowed to equilibrate overnight. Cells were washed 3x2 minutes with PBS and incubated for 90 minutes with an Alexa Fluor 647 labelled antibody against LFA-1 (Abcam, ab186873). After washing 4x2 minutes with PBS, dSTORM buf-

fer was added and cells were imaged. After imaging, cells were washed 3x2 minutes with PBS, washed 3x2 minutes with madSTORM buffer (3.5M $MgCl_2$, 0.1% Tween-20, 20mM PIPES) to remove the prior staining. Simultaneous with the madSTORM incubations, the microscope revisited all acquired positions with the laser set at maximum power to assist with bleaching any remaining antibodies. Cells were then washed 3x2 minutes with PBS, incubated with 0.5% Triton-X for 10 minutes, washed 4x3 minutes with PBS and incubated for 90 minutes with an Alexa Fluor 647 labelled antibody against pFAK (Thermo Fisher, 700255). After washing 4x2 minutes with PBS, dSTORM buffer was added and cells were imaged. The same labelling removal, staining and imaging process was then repeated with an Alexa Fluor 647 labelled antibody targeting phosphorylated Src family kinases (Cell Signalling Technology, 82975), with the omission of the Triton-X step.

4.5.4 Sequential Labelling

The solutions used in the sequential labelling tests were as follows: 0.1 M glycine hydrochloride (Sigma, G2879) pH was adjusted to 2.2; 20mM DTT (Thermo Fisher, 20291); Tramu et al. (1978) solution - 0.15M $KMNO_4$ and 0.01N H_2SO_4; Hydrogen peroxide tests used a 30% H_2O_2 commercial solution (Sigma, 216763); 0.1% Sodium borohydride (Sigma, 213462). To perform DNA-PAINT imaging, imaging strands were diluted in PBS containg 500mM $MgCl_2$, pH 7.4, and all washes were performed with PBS, pH 7.4.

4.5.5 Data Processing and Analysis

For all of the above SMLM experiments, super-resolution imaging was performed as in section 2.4.3, except the exposure time was set at 18ms and EM-gain was set at 70. The resultimg images were analysed using the SRRF algorithm set to perform Temporal Radiality Maximum (Gustafsson et al., 2016). Settings were: Ring radius of 0.5; 6 axis per ring; magnification of 5; and intensity weighting was performed. All other image processing was performed as in section 2.4.4.

To measure the mean camera grey value in figure 4.1, FIJI was used. First, a Region of Interest (ROI) corresponding to the cell shape was determined by apply-

ing the Otsu threshold algorithm. Having established the ROI, the mean value was measured on the same ROI for both channels, before and after incubation with the buffer.

For the cluster analysis in section 4.2.4, 3 colour pointillist maps were analysed channel per channel with Bayesian cluster analysis software (Griffie et al., 2016), and colocalization was analysed using Rossey's method as described (Rossy et al., 2014). The correlation measurements and linear fits in table 4.1 were performed with Matlab.

4.6 Bibliography

Agasti, Sarit S. et al. 'DNA-barcoded labeling probes for highly multiplexed Exchange-PAINT imaging'. In: *Chem. Sci.* 8.4 (Mar. 2017), pp. 3080–3091. ISSN: 2041-6520. DOI: 10.1039/C6SC05420J.

Andronov, Leonid et al. 'ClusterViSu, a method for clustering of protein complexes by Voronoi tessellation in super-resolution microscopy'. In: *Scientific Reports* 6.1 (2016), p. 24084. ISSN: 2045-2322. DOI: 10.1038/srep24084.

Auer, Alexander et al. 'Fast, background-free DNA-PAINT imaging using FRET-based probes.' In: *Nano letters* (Sept. 2017), acs.nanolett.7b03425. ISSN: 1530-6992. DOI: 10.1021/acs.nanolett.7b03425.

Bearce, Beth. *Recovery after Cold Shock Depolymerization assays have taught me how to place/find/focus a sample at 63x in ~10seconds.* 2017. URL: https://twitter.com/Carcinoginger/status/906289173988085762.

Bedford, R. et al. 'Alternative reagents to antibodies in imaging applications'. In: *Biophysical Reviews* (2017), pp. 299–308. ISSN: 1867-2450. DOI: 10.1007/s12551-017-0278-2.

Berod, a, B K Hartman and J F Pujol. 'Importance of fixation in immunohistochemistry: use of formaldehyde solutions at variable pH for the localization of tyrosine hydroxylase.' In: *The journal of histochemistry and cytochemistry : official journal of the Histochemistry Society* 29.7 (1981), pp. 844–850. ISSN: 0022-1554. DOI: 10.1177/29.7.6167611.

Bershadsky, Alexander D., Nathalie Q. Balaban and Benjamin Geiger. 'Adhesion-Dependent Cell Mechanosensitivity'. In: *Annual Review of Cell and Developmental Biology* 19.1 (2003), pp. 677–695. ISSN: 1081-0706. DOI: 10.1146/annurev.cellbio.19.111301.153011.

Bolognesi, Maddalena Maria et al. 'Multiplex Staining by Sequential Immunostaining and Antibody Removal on Routine Tissue Sections'. In: *Journal of Histochemistry & Cytochemistry* 65.8 (2017), pp. 431–444. ISSN: 0022-1554. DOI: 10.1369/0022155417719419.

Brown, Jeremy K. et al. 'Primary Antibody–Fab Fragment Complexes: A Flexible Alternative to Traditional Direct and Indirect Immunolabeling Techniques'. In: *Journal of Histochemistry & Cytochemistry* 52.9 (Sept. 2004), pp. 1219–1230. ISSN: 0022-1554. DOI: 10.1369/jhc.3A6200.2004.

Brown, M. C. 'Paxillin: Adapting to Change'. In: *Physiological Reviews* 84.4 (2004), pp. 1315–1339. ISSN: 0031-9333. DOI: 10.1152/physrev.00002.2004.

Burridge, Keith and Magdalena Chrzanowska-Wodnicka. 'Focal Adhesions, Contractility, and Signaling'. In: *Annu. Rev. Cell Dev. Biol* 12 (1996), pp. 463–519. ISSN: 1081-0706. DOI: 10.1146/annurev.cellbio.12.1.463.

Chen, Lingfeng et al. 'The integrin-ligand interaction regulates adhesion and migration through a molecular clutch'. In: *PLoS ONE* 7.7 (2012). ISSN: 19326203. DOI: 10.1371/journal.pone.0040202.

Cramer, L. and T. J. Mitchison. 'Moving and stationary actin filaments are involved in spreading of postmitotic PtK2 cells'. In: *Journal of Cell Biology* 122.4 (1993), pp. 833–843. ISSN: 00219525. DOI: 10.1083/jcb.122.4.833.

Dempsey, Graham T et al. 'Evaluation of fluorophores for optimal performance in localization-based super-resolution imaging.' In: *Nature methods* 8.12 (Dec. 2011), pp. 1027–36. ISSN: 1548-7105. DOI: 10.1038/nmeth.1768.

Dustin, Michael L. 'Stop and go traffic to tune T cell responses'. In: *Immunity* 21.3 (2004), pp. 305–314. ISSN: 10747613. DOI: 10.1016/j.immuni.2004.08.016.

Eisen, H. N. 'Affinity Enhancement of Antibodies: How Low-Affinity Antibodies Produced Early in Immune Responses Are Followed by High-Affinity Antibodies Later and in Memory B-Cell Responses'. In: *Cancer Immunology Research* 2.5 (2014), pp. 381–392. ISSN: 2326-6066. DOI: 10.1158/2326-6066.CIR-14-0029.

Eldred, W D et al. 'Comparison of fixation and penetration enhancement techniques for use in ultrastructural immunocytochemistry.' In: *J Histochem Cytochem.* 31 (1983), pp. 285–292. ISSN: 0022-1554. DOI: 10.1177/31.2.6339606.

Fink, Jenny et al. 'External forces control mitotic spindle positioning'. In: *Nature Cell Biology* 13.7 (2011), pp. 771–778. ISSN: 1465-7392. DOI: 10.1038/ncb2269.

Friedl, Peter and Bettina Weigelin. 'Interstitial leukocyte migration and immune function'. In: *Nature Immunology* 9.9 (2008), pp. 960–969. ISSN: 1529-2908. DOI: 10.1038/ni.f.212.

Geiger, B et al. 'Transmembrane crosstalk between the extracellular matrix–cytoskeleton crosstalk.' In: *Nature reviews. Molecular cell biology* 2.11 (2001), pp. 793–805. ISSN: 1471-0072. DOI: 10.1038/35099066.

Gendusa, Rossella et al. 'Elution of High-affinity (>10-9 KD) Antibodies from Tissue Sections: Clues to the Molecular Mechanism and Use in Sequential Immunostaining.' In: *The journal of histochemistry and cytochemistry : official journal of the Histochemistry Society* 62.7 (May 2014), pp. 519–531. ISSN: 1551-5044. DOI: 10.1369/0022155414536732.

Gerdes, Michael J. et al. 'Highly multiplexed single-cell analysis of formalin-fixed, paraffin-embedded cancer tissue.' In: *Proceedings of the National Academy of Sciences of the United States of America* 110.29 (July 2013), pp. 11982–7. ISSN: 1091-6490. DOI: 10.1073/pnas.1300136110.

Giannone, Gregory et al. 'Dynamic superresolution imaging of endogenous proteins on living cells at ultra-high density.' In: *Biophysical journal* 99.4 (Aug. 2010), pp. 1303–10. ISSN: 1542-0086. DOI: 10.1016/j.bpj.2010.06.005.

Gierke, Sarah, Praveen Kumar and Torsten Wittmann. 'Analysis of microtubule polymerization dynamics in live cells.' In: *Methods in cell biology* 97 (Jan. 2010), pp. 15–33. ISSN: 0091-679X. DOI: 10.1016/S0091-679X(10)97002-7.

Griffie, Juliette et al. 'A Bayesian cluster analysis method for single-molecule localization microscopy data'. In: *Nat. Protocols* 11.12 (2016), pp. 2499–2514. ISSN: 1754-2189. DOI: 10.1038/nprot.2016.149.

Gustafsson, Nils et al. 'Fast live-cell conventional fluorophore nanoscopy with ImageJ through super-resolution radial fluctuations'. In: *Nature Communications* 7 (Aug. 2016), p. 12471. ISSN: 2041-1723. DOI: 10.1038/ncomms12471.

Holliger, Philipp and Peter J Hudson. 'Engineered antibody fragments and the rise of single domains'. In: *Nature Biotechnology* 23.9 (2005), pp. 1126–1136. ISSN: 1087-0156. DOI: 10.1038/nbt1142. arXiv: arXiv:1011.1669v3.

Hong, Jangmi et al. 'Structural characterization of immunoglobulin G using time-dependent disulfide bond reduction'. In: *Analytical Biochemistry* 384.2 (2009), pp. 368–370. ISSN: 00032697. DOI: 10.1016/j.ab.2008.10.012.

Iliuk, Anton B., Lianghai Hu and W. Andy Tao. 'Aptamer in bioanalytical applications'. In: *Analytical Chemistry* 83.12 (2011), pp. 4440–4452. ISSN: 00032700. DOI: 10.1021/ac201057w. arXiv: NIHMS150003.

Janeway, Charles. *Immunobiology 5 : the immune system in health and disease*. Garland Pub, 2001, p. 732. ISBN: 081533642X.

Johnstone, Ricky W. et al. 'The effect of temperature on the binding kinetics and equilibrium constants of monoclonal antibodies to cell surface antigens'. In: *Molecular Immunology* 27.4 (1990), pp. 327–333. ISSN: 01615890. DOI: 10.1016/0161-5890(90)90045-2.

Jungmann, Ralf, Maier S Avendaño et al. 'Multiplexed 3D cellular super-resolution imaging with DNA-PAINT and Exchange-PAINT.' In: *Nature methods* 11.3 (Mar. 2014), pp. 313–8. DOI: 10.1038/nmeth.2835.

Jungmann, Ralf, Christian Steinhauer et al. 'Single-Molecule Kinetics and Super-Resolution Microscopy by Fluorescence Imaging of Transient Binding on DNA Origami'. In: *Nano Letters* 10.11 (Nov. 2010), pp. 4756–4761. ISSN: 1530-6984. DOI: 10.1021/nl103427w.

Kanchanawong, Pakorn et al. 'Nanoscale architecture of integrin-based cell adhesions.' In: *Nature* 468.7323 (2010), pp. 580–584. ISSN: 1476-4687. DOI: 10.1038/nature09621.

Katakai, Tomoya, Katsuyoshi Habiro and Tatsuo Kinashi. 'Dendritic cells regulate high-speed interstitial T cell migration in the lymph node via LFA-1/ICAM-1.' In: *Journal of immunology (Baltimore, Md. : 1950)* 191.3 (2013), pp. 1188–99. ISSN: 1550-6606. DOI: 10.4049/jimmunol.1300739.

Kiuchi, Tai et al. 'Multitarget super-resolution microscopy with high-density labeling by exchangeable probes'. In: *Nature Methods* 12.July (2015). ISSN: 1548-7091. DOI: 10.1038/nmeth.3466.

Kolodziejczyk, E. and a. J. Baertschi. 'Multiple immunolabeling in histology: a new method using thermo-inactivation of immunoglobulins.' In: *The journal of histochemistry and cytochemistry : official journal of the Histochemistry Society* 34.12 (Dec. 1986), pp. 1725–9. ISSN: 0022-1554. DOI: 10.1177/34.12.3023476.

Komarova, Yulia A. et al. 'Cytoplasmic linker proteins promote microtubule rescue in vivo'. In: *Journal of Cell Biology* 159.4 (2002), pp. 589–599. ISSN: 15408140. DOI: 10.1083/jcb.200208058.

Legant, Wesley R et al. 'High-density three-dimensional localization microscopy across large volumes'. In: *Nature Methods* 13.4 (2016), pp. 359–365. ISSN: 1548-7091. DOI: 10.1038/nmeth.3797. arXiv: 1602.03837.

Levet, Florian et al. 'SR-Tesseler: a method to segment and quantify localization-based super-resolution microscopy data'. In: *Nature Methods* 12.11 (2015), pp. 1065–1071. ISSN: 1548-7091. DOI: 10.1038/nmeth.3579.

Lin, Jia Ren, Mohammad Fallahi Sichani, Jia-yun Chen et al. 'Cyclic Immunofluorescence (CycIF), A Highly Multiplexed Method for Single-cell Imaging'. In: *Current Protocols in Chemical Biology*. Vol. 8. Hoboken, NJ, USA: John Wiley & Sons, Inc., Dec. 2016, pp. 251–264. DOI: 10.1002/cpch.14.

Lin, Jia Ren, Mohammad Fallahi Sichani and Peter K Sorger. 'Highly multiplexed imaging of single cells using a high-throughput cyclic immunofluorescence method.' In: *Nature communications* 6 (Sept. 2015), p. 8390. ISSN: 2041-1723. DOI: 10.1038/ncomms9390.

Mali, Prashant, Denis Wirtz and Peter C. Searson. 'Interplay of RhoA and motility in the programmed spreading of daughter cells postmitosis'. In: *Biophysical Journal* 99.11 (2010), pp. 3526–3534. ISSN: 00063495. DOI: 10.1016/j.bpj.2010.10.006.

Malkusch, Sebastian and Mike Heilemann. 'Extracting quantitative information from single-molecule super-resolution imaging data with LAMA – LocAlization Microscopy Analyzer'. In: *Scientific Reports* 6.1 (2016), p. 34486. ISSN: 2045-2322. DOI: 10.1038/srep34486.

Marchesi, Stefano et al. 'DEPDC1B coordinates de-adhesion events and cell-cycle progression at mitosis'. In: *Developmental Cell* 31.4 (2014), pp. 420–433. ISSN: 18781551. DOI: 10.1016/j.devcel.2014.09.009.

Mazouchi, A. and J. N. Milstein. 'Fast Optimized Cluster Algorithm for Localizations (FOCAL): a spatial cluster analysis for super-resolved microscopy'. In: *Bioinformatics* 32.5 (Mar. 2016), pp. 747–754. ISSN: 1367-4803. DOI: 10.1093/bioinformatics/btv630.

Micheva, Kristina D and Stephen J Smith. 'Array tomography: a new tool for imaging the molecular architecture and ultrastructure of neural circuits.' In: *Neuron* 55.1 (July 2007), pp. 25–36. ISSN: 0896-6273. DOI: 10.1016/j.neuron.2007.06.014.

Miller, M. J. 'Two-Photon Imaging of Lymphocyte Motility and Antigen Response in Intact Lymph Node'. In: *Science* 296.5574 (2002), pp. 1869–1873. ISSN: 00368075. DOI: 10.1126/science.1070051.

Mitchison, T. J. 'Actin based motility on retraction fibers in mitotic PtK2 cells'. In: *Cell Motility and the Cytoskeleton* 22.2 (1992), pp. 135–151. ISSN: 10970169. DOI: 10.1002/cm.970220207.

Moser, Annette C and David S Hage. 'Immunoaffinity chromatography: an introduction to applications and recent developments'. In: *Bioanalysis* 2.4 (2010), pp. 769–790. ISSN: 1757-6180. DOI: 10.4155/bio.10.31.

Murray, Evan et al. 'Simple, Scalable Proteomic Imaging for High-Dimensional Profiling of Intact Systems'. In: *Cell* 163.6 (2015), pp. 1500–1514. ISSN: 10974172. DOI: 10.1016/j.cell.2015.11.025.

Nakane, P K. 'Simultaneous localization of multiple tissue antigens using the peroxidase-labeled antibody method: a study on pituitary glands of the rat.' In: *The journal of histochemistry and cytochemistry : official journal of the Histochemistry Society* 16.9 (1968), pp. 557–560. ISSN: 0022-1554. DOI: 10.1177/16.9.557.

Nanguneri, Siddharth et al. 'Three-dimensional, tomographic super-resolution fluorescence imaging of serially sectioned thick samples.' In: *PloS one* 7.5 (May 2012). Ed. by Markus Sauer, e38098. DOI: 10.1371/journal.pone.0038098.

Narhi, L O et al. 'Effect of three elution buffers on the recovery and structure of monoclonal antibodies.' In: *Analytical biochemistry* 253.2 (1997), pp. 236–245. ISSN: 0003-2697. DOI: 10.1006/abio.1997.2375.

Parsons, J. Thomas, Alan Rick Horwitz and Martin A. Schwartz. 'Cell adhesion: integrating cytoskeletal dynamics and cellular tension'. In: *Nature Reviews Molecular Cell Biology* 11.9 (2010), pp. 633–643. ISSN: 1471-0072. DOI: 10.1038/nrm2957. arXiv: NIHMS150003.

Pierobon, Mariaelena et al. *Reverse phase protein microarrays for clinical applications*. Vol. 785. 2011, pp. 3–12. ISBN: 978-1-61779-285-4. DOI: 10.1007/978-1-61779-286-1_1.

Pirici, Daniel et al. 'Antibody elution method for multiple immunohistochemistry on primary antibodies raised in the same species and of the same subtype.' In: *The journal of histochemistry and cytochemistry : official journal of the Histochemistry Society* 57.6 (2009), pp. 567–575. ISSN: 0022-1554. DOI: 10.1369/jhc.2009.953240.

Ramkumar, Nitya and Buzz Baum. 'Coupling changes in cell shape to chromosome segregation'. In: *Nature Reviews Molecular Cell Biology* 17.8 (2016), pp. 511–521. ISSN: 1471-0072. DOI: 10.1038/nrm.2016.75.

Reverberi, Roberto and Lorenzo Reverberi. 'Factors affecting the antigen-antibody reaction'. In: *Blood Transfusion* 5.4 (2007), pp. 227–240. ISSN: 17232007. DOI: 10.2450/2007.0047-07.

Riedl, Julia et al. 'Lifeact: a versatile marker to visualize F-actin.' In: *Nature methods* 5.7 (July 2008), pp. 605–7. ISSN: 1548-7105. DOI: 10.1038/nmeth.1220.

Rossy, Jérémie et al. 'Method for co-cluster analysis in multichannel single-molecule localisation data'. In: *Histochemistry and Cell Biology* 141.6 (2014), pp. 605–612. ISSN: 1432119X. DOI: 10.1007/s00418-014-1208-z.

Saerens, Dirk, Gholamreza Hassanzadeh Ghassabeh and Serge Muyldermans. 'Antibody technology in proteomics'. In: *Briefings in Functional Genomics and Proteomics* 7.4 (2008), pp. 275–282. ISSN: 14739550. DOI: 10.1093/bfgp/eln028.

Schlaepfer, David D., Christof R. Hauck and David J. Sieg. 'Signaling through focal adhesion kinase'. In: *Progress in Biophysics and Molecular Biology* 71.3-4 (1999), pp. 435–478. ISSN: 00796107. DOI: 10.1016/S0079-6107(98)00052-2.

Schnitzbauer, Joerg et al. 'Super-resolution microscopy with DNA-PAINT'. In: *Nature Protocols* 12.6 (2017), pp. 1198–1228. ISSN: 1754-2189. DOI: 10.1038/nprot.2017.024.

Schoen, Ingmar et al. 'Binding-activated localization microscopy of DNA structures.' In: *Nano letters* 11.9 (Sept. 2011), pp. 4008–11. ISSN: 1530-6992. DOI: 10.1021/nl2025954.

Schubert, Walter et al. 'Analyzing proteome topology and function by automated multidimensional fluorescence microscopy.' In: *Nature biotechnology* 24.10 (Oct. 2006), pp. 1270–8. ISSN: 1087-0156. DOI: 10.1038/nbt1250.

Schweller, Ryan M. et al. 'Multiplexed In-Situ Immunofluorescence Using Dynamic DNA Complexes'. In: *Angewandte Chemie International Edition* 51.37 (Sept. 2012), pp. 9292–9296. ISSN: 14337851. DOI: 10.1002/anie.201204304.

Shannon, Michael J. et al. 'Protein clustering and spatial organization in T-cells'. In: *Biochemical Society Transactions* 43.3 (June 2015), pp. 315–321. ISSN: 0300-5127. DOI: 10.1042/BST20140316.

Sharonov, Alexey and Robin M Hochstrasser. 'Wide-field subdiffraction imaging by accumulated binding of diffusing probes.' In: *Proceedings of the National Academy of Sciences of the United States of America* 103.50 (2006), pp. 18911–18916. ISSN: 0027-8424. DOI: 10.1073/pnas.0609643104.

Smith, Andrew et al. 'A talin-dependent LFA-1 focal zone is formed by rapidly migrating T lymphocytes'. In: *Journal of Cell Biology* 170.1 (2005), pp. 141–151. ISSN: 00219525. DOI: 10.1083/jcb.200412032.

Smith, M. A., L. M. Hoffman and M. C. Beckerle. 'LIM proteins in actin cytoskeleton mechanoresponse'. In: *Trends in Cell Biology* 24.10 (2014), pp. 575–583. ISSN: 18793088. DOI: 10.1016/j.tcb.2014.04.009. arXiv: NIHMS150003.

Smolinski, Dorthe von et al. 'Validation of a novel ultra-short immunolabeling method for high-quality mRNA preservation in laser microdissection and real-time reverse transcriptase-polymerase chain reaction.' In: *The Journal of molecular diagnostics : JMD* 8.2 (Mar. 2006), pp. 246–53. ISSN: 1525-1578. DOI: 10.2353/jmoldx.2006.050096.

Swaminathan, V., R. S. Fischer and C. M. Waterman. 'The FAK-Arp2/3 interaction promotes leading edge advance and haptosensing by coupling nascent adhesions to lamellipodia actin'. In: *Molecular Biology of the Cell* 27.7 (2016), pp. 1085–1100. ISSN: 1059-1524. DOI: 10.1091/mbc.E15-08-0590.

Tam, Johnny et al. 'Cross-Talk-Free Multi-Color STORM Imaging Using a Single Fluorophore.' In: *PloS one* 9.7 (Jan. 2014), e101772. ISSN: 1932-6203. DOI: 10.1371/journal.pone.0101772.

Teijeira, Alvaro et al. 'T Cell Migration from Inflamed Skin to Draining Lymph Nodes Requires Intralymphatic Crawling Supported by ICAM-1/LFA-1 Interactions'. In: *Cell Reports* 18.4 (2017), pp. 857–865. ISSN: 22111247. DOI: 10.1016/j.celrep.2016.12.078.

Théry, Manuel et al. 'The extracellular matrix guides the orientation of the cell division axis'. In: *Nature Cell Biology* 7.10 (2005), pp. 947–953. ISSN: 1465-7392. DOI: 10.1038/ncb1307.

Tiede, Christian et al. 'Adhiron: A stable and versatile peptide display scaffold for molecular recognition applications'. In: *Protein Engineering, Design and Selection* 27.5 (2014), pp. 145–155. ISSN: 17410134. DOI: 10.1093/protein/gzu007.

Toyoshima, Fumiko and Eisuke Nishida. 'Integrin-mediated adhesion orients the spindle parallel to the substratum in an EB1- and myosin X-dependent manner'. In: *The EMBO Journal* 26.6 (2007), pp. 1487–1498. ISSN: 0261-4189. DOI: 10.1038/sj.emboj.7601599.

Tramu, G., a. Pillez and J. Leonardelli. 'An efficient method of antibody elution for the successive or simultaneous localization of two antigens by immunocytochemistry.' In: *Journal of Histochemistry & Cytochemistry* 26.4 (Apr. 1978), pp. 322–324. ISSN: 0022-1554. DOI: 10.1177/26.4.207771.

Valley, Christopher C. et al. 'Sequential superresolution imaging of multiple targets using a single fluorophore.' In: *PloS one* 10.4 (2015), e0123941. ISSN: 1932-6203. DOI: 10.1371/journal.pone.0123941.

Vandesande, F and K Dierickx. 'Identification of the vasopressin producing and of the oxytocin producing neurons in the hypothalamic magnocellular neurosecretroy system of the rat.' In: *Cell and tissue research* 164.2 (1975), pp. 153–162. ISSN: 0302-766X. DOI: 10.1007/BF00218970.

— 'Immunocytochemical demonstration of separate vasotocinergic and mesotocinergic neurons in the amphibian hypothalamic magnocellular neurosecretory system.' In: *Cell and tissue research* 175.3 (1976), pp. 289–296. ISSN: 0302-766X. DOI: 10.1007/BF00218707.

Vorob'ev, I A and I S Grigor'ev. '[Dynamics and the life cycle of cell microtubules].' In: *TSitologiia i genetika* 37.2 (2003), pp. 22–38. ISSN: 0564-3783.

Wählby, Carolina et al. 'Sequential immunofluorescence staining and image analysis for detection of large numbers of antigens in individual cell nuclei.' In:

Cytometry 47.1 (Jan. 2002), pp. 32–41. ISSN: 0196-4763. DOI: 10.1002/cyto.10026.

Welman, Arkadiusz et al. 'Two-color photoactivatable probe for selective tracking of proteins and cells.' In: *The Journal of biological chemistry* 285.15 (Apr. 2010), pp. 11607–16. ISSN: 1083-351X. DOI: 10.1074/jbc.M110.102392.

Woolf, Eilon et al. 'Lymph node chemokines promote sustained T lymphocyte motility without triggering stable integrin adhesiveness in the absence of shear forces.' In: *Nature immunology* 8.10 (2007), pp. 1076–1085. ISSN: 1529-2908. DOI: 10.1038/ni1499.

Yi, Jason et al. 'madSTORM: a Super-Resolution Technique for Large-Scale Multiplexing at Single Molecule Accuracy.' In: *Molecular biology of the cell* 27 (2016). ISSN: 1939-4586. DOI: 10.1091/mbc.E16-05-0330.

Zhang, Xian et al. 'Talin depletion reveals independence of initial cell spreading from integrin activation and traction.' In: *Nature cell biology* 10.9 (2008), pp. 1062–1068. ISSN: 1465-7392. DOI: 10.1038/ncb1765.

Chapter 5

Concluding remarks

The Alpha and the NanoJ-Optofluidics platforms are fully functioning systems. The Alpha has demonstrated large FOV SMLM imaging at high frame-rates by optimising illumination to harness the new sCMOS camera technologies. NanoJ-Optofluidics platforms have been demonstrated to achieve online fixation, immunostaining and buffer exchange for SMLM imaging and sequential labelling. By performing online fixation and immuno-labelling, the platform was able to demonstrate how retraction fibres attach to the cell's substrate by integrins from previously disassembled focal adhesion. A similar approach has also demonstrated that the number of LFA-1 (T-cell specific integrin) clusters in T-cells are correlated with cell speed. Finally, the system allowed both sequential labelling by bleaching and DNA-PAINT to be combined in one experiment. These experiments could be achieved in a reliable manner and by a system which is orders of magnitude less expensive than commercial fluidics systems. All of the components of the NanoJ-Optofluidics platform are easily available, easy to repair and require no special expertise to assemble and operate, making a true universally accessible fluidic system.

Integrating automated microscope acquisition with automated microfluidics should also enable new applications. For example, computer vision algorithms can be used to identify specific events that occur during live imaging and the microfluidic system can add drugs or fixatives at that particular time point. This should further help to fix cells during rare transitions, like mitosis, for example.

However, the Alpha and NanoJ-Optofluidics yet to be integrated into a single,

unified system. To enable high-throughput multiplexed SMLM, this integration should happen in a fully automated manner. There is currently a functioning method to perform an integrated acquisition, but it depends on Micro-Manager scripts. section 3.3.3 details a future plugin for Micro-Manager with a user interface coordinate between starting fluidic protocols and Micro-Manager acquisitions. This would be a user-friendly approach, which would make the system more widely applicable. However, as mentioned in section 2.3.4, the true bottleneck for a completely automated acquisition is the current drift correction scheme, as the current system only corrects for one stage position reference. section 2.3.4 outlines an approach to address this, where the software would automatically obtain a new reference image for each new stage position. Should drift correction be successfully extended to a multi-position acquisition, it should also immediately be useful for sequential labelling experiments. Throughout the experiments shown in chapter 4, images acquired before fixation, after fixation and after different rounds of labelling all needed to be registered to each other *a posteriori*. The drift correction by cross-correlation method should be able to maintain samples stable in both the lateral and axial directions. This means images do not need to be registered to each other after acquisition.

With SMLM in particular, there are further bottlenecks generated by the need to reconstruct the localisations. First, the acquired images need to be be analysed, as to generate a super-resolution image. There are a large number of software packages that achieve this (Sage et al., 2015), and yet more are being developed. For HT SMLM, the focus should be on speed of analysis and there are packages which can analyse data in real-time (Smith et al., 2010; Kechkar et al., 2013; Li et al., 2017), largely by harnessing the graphical processing unit (GPU) of a computer. For all of these methods, however, a table of localisations is still generated. These tables contain millions of localisations, each with several parameters associated with it such as XY location, localisation precision, pixel intensity, etc. If a SMLM image stack can reach tens of gigabytes, so do these localisation tables. This creates a data storage burden on HT SMLM systems. For example, acquiring 100 different

positions with the full field of view of an sCMOS, at 40.000 frames per acquisition and with 4 colours, yields that 128 terabytes are necessary just for the raw data of one experiment. The localisation data can vary anywhere between a quarter to the same size as the raw acquisition data. With these two facts in mind, the limitations become obvious. The Henriques lab has recently developed a new method for super-resolution analysis, super-resolution radial fluctuation (SRRF) method, which is based on analysing image transforms and does not generate a localisation table (Gustafsson et al., 2016). It can also analyse images in real-time, and this has been implemented with scientific camera systems as the SRRF-STREAM system (Andor Technology Ltd, 2017). Because there are very few parameters to adjust, if at all, the raw data need not be retained and the SRRF-STREAM gives the output of the algorithm as the final output of an imaging system instead of the unprocessed camera data (Andor Technology Ltd, 2017). If the LMCB-Alpha microscope and the NanoJ-Optofluidics platform are integrated with SRRF-STREAM, such a system would generate SMLM images immediately after imaging, without requiring any SMLM processing, channel registration, or separate large storage management facilities. For the same example given above of 100 full sCMOS fields of view and 4 colours, that corresponds to a total of 84 gigabytes, or almost 4 orders of magnitude less storage space required.

Combining high-throughput SMLM imaging, microfluidics and SRRF-STREAM imaging is a straightforward proposition. Such an integrated system would be able to image whole signalling complexes like the T-cell receptor, or complex multi-molecular structures like focal adhesions, and the dynamic context for each individual cell would be known. The fast nature of a such a system would enable these experiments to be carried out in the course of a few days, if not a day. A single researcher manually staining, acquiring, analysing and correlating different populations of cells to try and determine these complexes and structures would take months to achieve similar results, and with many more potential sources of bias. Overall, further exploiting the systems demonstrated in this work has the potential to be an enabling technology to many research scientists studying cell

biology.

5.1 Bibliography

Andor Technology Ltd. *SRRF-Stream Real Time Super-Resolution | Andor*. 2017. URL: http://www.andor.com/srrf-stream (visited on 17/09/2017).

Gustafsson, Nils et al. 'Fast live-cell conventional fluorophore nanoscopy with ImageJ through super-resolution radial fluctuations'. In: *Nature Communications* 7 (Aug. 2016), p. 12471. ISSN: 2041-1723. DOI: 10.1038/ncomms12471.

Kechkar, Adel et al. 'Real-time analysis and visualization for single-molecule based super-resolution microscopy.' In: *PloS one* 8.4 (Jan. 2013), e62918. ISSN: 1932-6203. DOI: 10.1371/journal.pone.0062918.

Li, Yiming et al. 'Fast, robust and precise 3D localization for arbitrary point spread functions'. In: *bioRxiv* (2017), pp. 1–16. DOI: 10.1101/172643.

Sage, Daniel et al. 'Quantitative evaluation of software packages for single-molecule localization microscopy'. In: *Nature Methods* August 2014 (2015), pp. 1–12. ISSN: 1548-7091. DOI: 10.1038/nmeth.3442.

Smith, Carlas S et al. 'Fast, single-molecule localization that achieves theoretically minimum uncertainty.' In: *Nature methods* 7.5 (May 2010), pp. 373–5. ISSN: 1548-7105. DOI: 10.1038/nmeth.1449.

Appendix A

Acronyms

3D three dimensions.

ASI Applied Scientific Instrumentation.

BFP Back Focal Plane.

CAD Computer Aided Design.

CCM Cross Correlation Map.

CCSR Cross Correlation by Static Reference.

CRISP Continuous Reflective Interface Sample Placement.

CSV Comma Separated Values.

DC Direct Current.

dSTORM direct Stochastic Optical Reconstruction Microscopy.

EM Electron Microscopy.

EM-CCD Electron-Multiplying Charge-Coupled Device.

FFT Fast Fourier Transform.

FOV Field-Of-View.

FPS Frames Per Second.

FRC Fourier Ring Correlation.

FRET Förster Resonance Energy Transfer.

GUI Graphical User Interface.

HPLC High-Performance Liquid Chromatography.

IR Infra-Red.

LED Light Emitting Diode.

MIM Modular Infinity Microscope.

NA Numerical Aperture.

PALM Photoactivated Localization Microscopy.

PDMS Polydimethylsiloxane.

PSF Point Spread Function.

PWM Pulse Width Modulation.

QE Quantum Efficiency.

RAMM Rapid Automated Modular Microscope.

RI Refractive Index.

sCMOS scientific Complementary Metal Oxide Semiconductor.

SIM Structured Illumination Microscopy.

SMLM Single Molecule Localization Microscopy.

SNR Signal-to-Noise Ratio.

SR Super-Resolution.

STED Stimulated Emission Depletion.

TIRF Total Internal Reflection Fluorescence.

UV Ultra-Violet.